ENGINEERING CHARACTERIZATION OF WASTE DERIVED GEOPOLYMER CEMENT CONCRETE FOR STRUCTURAL APPLICATIONS

by

Brett Tempest

A dissertation submitted to the faculty of
The University of North Carolina at Charlotte
in partial fulfillment of the requirements
for the degree of Doctor of Philosophy in
Infrastructure and Environmental Systems

Charlotte

2010

Approved by:

_____
Dr. Janos Gergely

_____
Dr. Rajaram Janardhanam

_____
Dr. Helene Hilger

_____
Dr. Vincent Ogunro

_____
Dr. Jeff Ramsdell

_____
Dr. David Weggel

ABSTRACT

BRETT TEMPEST. Engineering characterization of waste derived geopolymer cement concrete for structural applications. (Under direction of DR. JANOS GERGELY)

Geopolymer cements provide an alternative to the Portland cement used to manufacture structural concrete. The material commonly used to produce geopolymers is fly ash, which is found in the waste stream of power generation facilities. Therefore, replacing Portland cement with geopolymer cement improves the sustainability of concrete by reducing emissions and diverting waste from landfils. In this study, geopolymer cements were used to create concrete having compressive strength in the range of 5,000 to 12,000 psi (34-83 MPa). The mechanical properties of these concretes were evaluated to determine the compressive, tensile and elastic behaviors. Durability tests were also performed to assess creep and shrinkage characteristics. Prestressed and mild steel reinforced beams were made with the geopolymer cement concrete (GCC) and were tested to failure. The results of these flexural tests were used to confirm the applicability of traditional concrete design criteria and techniques. The GCC was found to perform in a similar manner to Portland cement concrete and the efficacy of existing design formulations was verified with small changes to some design values. Finally, the processes and materials used to prepare the concretes were used to make a preliminary lifecycle assessment to verify the sustainability gains of GCC. Reduced energy use and emissions generation were confirmed.

AKNOWLEDGMENTS

I have been fortunate throughout my graduate studies for having strong support from my advisor, my classmates, my committee and my family. Thank you to Dr. Janos Gergely for your guidance, encouragement and mentorship over the many years I have been your student. Thank you to Tina, Ailee, Mom and Dad for tolerating the mania that these studies sometimes brought. Thank you to Jeff Berryman, Alex Gotta, Cassanni Laville, Olanrewaju Sanusi, Angela Sims and Mitch Taylor for your dedication to the project and the long hours you contributed. Special thanks to Mike Moss for all the times you've rolled your sleeves up and gotten the work done in spite of the budget, the hours or the challenges of the task. Finally, thank you to the members of my dissertation committee, Drs. Helene Hilger, Rajaram Janardhanam Vincent Ogunro, Jeff Ramsdell and David Weggel, for your generous contributions of time, advice and direction.

TABLE OF CONTENTS

LIST OF FIGURES

LIST OF TABLES

CHAPTER 1: INTRODUCTION

1.1 Background

Concrete is one of the most ubiquitous construction materials in the world due to its durability, flexibility and economy. The latter two of these features arise from the ability of concrete producers to incorporate a variety of source materials, while still guaranteeing suitable structural performance. For instance, the aggregates used in concrete vary widely from granitic to calciferous materials depending on the geology local to the production site. The cementitious constituents also tend to be locally produced from materials that are available in proximity to the cement mill. Because of this tradition of local production and flexibility in the nature of source materials, concrete could become one of the most sustainable construction materials available. However, even with modern production techniques it is extremely energy and emissions intensive to manufacture.

The production of Portland cement for concrete is becoming an unattractive industrial process as concern mounts over energy use and greenhouse gas production. In order to manufacture Portland cement, limestone is heated in a kiln until $CaCO_3$ is reduced to CaO. This results in the release of one molecule of CO_2 for every molecule of CaO produced as well as an assortment of greenhouse gasses originating from the combustion of fuels used to heat the kiln. In total, 0.8 tons of CO_2 are released for every ton of cement produced (Gartner, 2004). The manufacture of cement accounts for at least

7% of worldwide greenhouse gas generation on an annual basis (Chindaprasirt et al., 2007).

Two existing strategies to reduce the energy and greenhouse gas intensiveness of concrete use are to seek alternate energy sources for heat generation during cement manufacture and to reduce the quantity of Portland cement required to mix concrete of various strengths. For instance, waste solvents and tires have been used in place of oil and natural gas in the kilns as energy sources. Research and practice have also shown that up to 35% of the cement can be replaced by the pozzolan, fly ash (ACI, 2003).

While the inclusion of fly ash represents some progress towards "green" concrete, the energy intensiveness of Portland cement remains a major impediment to true sustainability. However, despite the problems with Portland cement, concrete has an institutionalized role in economical construction and does provide many positive environmental features such as durability, recycleability and thermal mass. A new material, geopolymer cement, appears to be an alternative to Portland cement that can continue to provide concrete, but with a reduction in carbon dioxide.

As acceptance of global climate change grows, the motives for reducing greenhouse gas emissions are becoming imperatives for businesses. Limits to greenhouse gas production in the form of economic penalties are already appearing on the regulatory horizons for industrial emitters. Geopolymers could provide a solution to the challenges of manufacturing Portland cement (Duxson et al., 2007b).

1.2 Geopolymers

The term "geopolymer" was instituted by Davidovits (1991)following research into inorganic-polymer technologies for industrial applications. Geopolymers are formed

when alumino-silicates dissolve in a strong base, reorganize and precipitate in a hardened state (Davidovits, 1991; Duxson et al., 2007a). They can have properties very similar to Portland cement when formed under suitable conditions (Sofi et al., 2007b). Geopolymers have been manufactured from industrial wastes, such as blast furnace slag, for more than 60 years and are also often referred to as alkali-activated cements or inorganic polymer cements (Duxson et al., 2007a). Many researchers have produced geopolymer paste with kaolinite and metakaolinite as a source material of aluminates and silicates (Alonso and Palomo, 2001; Xu and Van Deventer, 2002). Construction silt and industrial waste products have also been successfully used (Lampris et al., 2009). Slavik et al. (2008) produced geopolymer material that attained structural strength with coal bottom ash and demonstrated its durability with freeze-thaw tests as well as wet-dry tests. However, the bulk of research into the use of industrial waste in geopolymer cements has centered on pulverized fuel ash or fly ash due to its wide and plentiful availability (Andini et al., 2008; Buchwald and Schulz, 2005; Duxson et al., 2007a; Duxson et al., 2007b; Jo et al., 2007; Palomo et al., 1999; Roy, 1999; Sun, 2005; van Deventer et al., 2007).

Of the more than 70 million tons of fly ash produced in the United States in 2006, much less than half was used; the remainder entered the waste stream. The southeast alone produced more than 30 million tons (American Coal Ash Association, 2007). Landfilling fly ash has been shown to have negative environmental consequences, including leaching toxic compounds and heavy metals into groundwater. The use of fly ash as an alumino-silicate source material for geopolymer gives rise to many environmental benefits. Not only does it eliminate the pollution problems associated

with Portland cement production, it relieves the burden of safely disposing of fly ash (Roy, 1999).

1.3 A civil engineering perspective on geopolymer research

As the material science research community has continued to study geopolymers, it has established that these materials can match or surpass Portland cement concrete in areas of strength and durability (van Deventer et al., 2007). Much of the research described in the literature is related to understanding the chemistry of inorganic polymer formation, reaction mechanisms and the relationship between base material composition, activating solution, curing conditions and characteristics of the hardened product (Fernandez-Jimenez and Palomo, 2003; van Jaarsveld et al., 2002). More recently, study of the engineering properties of geopolymer in terms of modulus of elasticity, Poisson's ratio and flexural strength has begun (Sofi et al., 2007b). Research has also been conducted on reinforced concrete columns created from geopolymer concrete that verified the relevance of existing design protocols to geopolymer structural elements (Sumajouw et al., 2007). Although there is a small body of research on the engineering properties of geopolymer cement, the quantity of data in this area is not sufficient to encourage its use in heavy construction. It is this area that must be researched from a civil engineering perspective.

1.4 Background on geopolymers

1.4.1 Geopolymerization process

Most of the research into the reaction mechanisms present during the formation of geopolymers has been based on metakaolin as the alumino-silicate source material. This is due to the greater homogeneity of metakaolin over fly ash. However, it is expected that the general geopolymerization mechanism is similar for the two materials, with the addition of subprocesses related to contaminants in the case of fly ash. The reaction of alumino-silicate materials in alkaline environments gives rise to the geopolymeric cements under consideration in this dissertation. The basic conceptual model of the geopolymerization process is a series of three phases, which are (Glukhovsky, 1959):

1) Dissolution- the aluminosilicate material is dissolved in an alkaline solution
2) Reorientation- the liberated silicate and aluminate monomers form short aluminosilicate oligomers
3) Solidification- the three dimensional geopolymer matrix becomes rigid

1.4.1.1 Dissolution

Aluminate and silicate ions are provided in solution via the dissolution process. Various source materials have characteristically different levels of reactivity in alkaline solutions. Panagiotopoulou (2007) dissolved pozzolana, fly ash, slag, kaolinite, metakaolinite and zeolite in solutions of varying alkalinity for varying amounts of time. It was found that the reactivity of the materials in decreasing order was, metakaolin>zeolite>slag>fly ash>pozzolana>kaolin. The degree of reactivity is likely related to multiple source material characteristics, including fineness, capability of cation

exchange and Al coordination (Panagiotopoulou et al., 2007). Panagiotopoulou et al. also found significant increases in the dissolution rates of Si by increasing the molarity of the alkaline solution from 2 to 5M. Using NaOH as the alkalinity source was found to be more effective at dissolving greater amounts of Si and Al than KOH (Panagiotopoulou et al., 2007).

The dissolution of fly ash in alkaline solutions has also been investigated by Mikuni et al. (2007). By dissolving fly ashes from pulverized coal combustion plants as well as pressurized fluidized bed combustion plants, high dissolution rates were found for aluminates at alkalinities between 5 and 10N at 25° C. Silicates were found to dissolve at increasing rates with increasing alkalinity.

The dissolution of aluminate and silicate into solution is described by the following three reactions:

$$Al_2O_3 + 3H_2O + 2OH^- \rightarrow 2[Al(OH)_4]^- \quad (1\text{-}1)$$
$$SiO_2 + H_2O + OH^- \rightarrow [SiO(OH)_3]^- \quad (1\text{-}2)$$
$$SiO_2 + 2OH^- \rightarrow [SiO_2(OH)_2]^{2-} \quad (1\text{-}3)$$

1.4.1.2 Reorientation

During the reorientation phase, the free aluminate and silicate monomers begin to form oligomers. First, the $[Al(OH)_4]^-$ and $[SiO(OH)_3]^-$ groups form an attraction between the Al and OH. As the two OH groups condense, an H_2O molecule is released. A similar reaction can occur between $[Al(OH)_4]^-$ and $[SiO_2(OH)_2]^{2-}$. This arrangement results in smaller oligomers than the condensation of $[Al(OH)_4]^-$ and $[SiO(OH)_3]^-$ (Weng and Sagoe-Crentsil, 2007). Because the proportion of $[SiO(OH)_3]^-$/ $[SiO_2(OH)_2]^{2-}$ is

dependent on the alkalinity of the activating solution, the formation of the whole geopolymer network is affected by the initial dissolution conditions.

1.4.1.3 Hardening

During the reorientation phase, a continuous gel network of three dimensional alumino-silicate structures is formed. As polymerization and hardening begin to occur, the possibility for transport of monomer species is precluded. Depending on the nature of the precursor groups, these structures may form the polysialate type (Si-O-Al-O-), polysialate-siloxo type (Si-O-Al-O-Si-O), or the polysialatedisiloxo type (Si-O-Al-O-Si-O-Si-O), as termed by Davidovits (1991).

Geopolymers have been cured at a variety of temperatures ranging from room-temperature to nearly 212 °F (100°C) depending on the source materials and strength development requirements. Alonso and Palomo studied the effect of heat addition to the geopolymer gel. Increased temperatures were found to accelerate the reaction and promote hardening (Alonso and Palomo, 2001). Swanepoel and Strydom (2002) found that an unsuitably slow reaction rate occurred under 140°F (60°C) in fly ashes sourced from the SASOL steam station. Others have developed geopolymers with compressive strengths suitable for structural application through room temperature curing (Sun, 2005).

1.5 Source materials

The precursors to geopolymer formation are sources of silicate and aluminate that form the backbone of the inorganic polymer. During the history of geopolymer development, most research has revolved around a two-part mixture system in which an alumino-silicate powder is combined with an alkaline liquid activator in order to initiate

the dissolution reaction. In this case, the alumino-silicate powder may consist of coal fly ashes or metakaolin. Some research has investigated biomass ashes from rice husk combustion as a partial replacement for the fly ash (Songpiriyakij et al., 2009). A second branch of geopolymer research is centered on the development of "one-part" systems or "just add water" mixes, in which the powder contains sufficient soluable alkaline components to initiate dissolution of silica with the addition of water (Duxson and Provis, 2008). Research presented in this document utilized a two-part system.

Although geopolymer materials can be reliably produced in the laboratory from pure reagents, the challenge comes in producing a consistent material from fly ash and other industrial byproducts that have variable compositions. The fly-ash can be characterized in terms of its physical features and chemical composition. Each of these features has an impact on the material properties of the hardened polymer.

1.5.1 Fly ash

Geopolymer made during the course of this research utilized fly ash as the source of aluminosilicates. Difficulty arises in manufacturing geopolymer from fly ash because it is a waste product from a highly variable stream. Even different samples from the same source have been known to produce final geopolymer concrete products with dissimilar rheology and strength development. Due to the magnitude of its production, fly ash is widely regarded as the most viable source material for bulk production of geopolymer cement concrete, much work presented in the literature has focused on empirically determining the characteristics of the material that produce acceptable results.

Ash characteristics that impact their usability in geopolymer applications are physical qualities, oxide composition and crystallography. Each of these characteristics

impacts either the rheology and reaction rate of the fresh material or the mechanical and microstructural characteristics of the hardened material (Diaz et al., 2009). Van Jaarsveld et al. found the particle size, calcium content, alkali metal content, amorphous content and origin of the fly ash to be important properties that contribute to the quality of the final geopolymer product (van Jaarsveld et al., 2003). Fernández-Jiménez (2003) described an activatable fly ash as having LOI less than 5%, Fe_2O_3 less than 10%, low CaO, reactive silica between 40 and 50% and 80 to 90% of particles smaller than $1.80X10^{-3}$" (45μm). The following is a summary of fly ash characteristics that determine its suitability as a source material for geopolymer.

1) Typical diameters for fly ash range between $3.9X10^{-5}$ and $7.9X10^{-3}$ in (1 μm - 1 mm (Mehta, 1989). However, the average size is highly dependent on the combustion process in the furnace where it is produced. The gradation of the fly ash is also important. Work done by Fernández-Jiménez and Palomo determined that removal of particle fractions larger than $1.80X10^{-3}$ in (45 μm) is related to substantial improvements in the 1-day compressive strength of samples and was able to develop 1-day strengths of over 10,000 psi (69 MPa) by removing these larger particles (Fernandez-Jimenez and Palomo, 2003). Because the fly ash is formed as molten coal ash molecules condense in the exhaust flue of the furnace where they are produced, the shape tends to be spherical.
2) The specific surface is often determined via the Blaine method or the BET method (named for its developers, Stephan Brunauer, Paul Emmett and Edward Teller). During the polymerization reactions, the gel matrix may begin to harden before the dissolution of the fly ash is complete. Therefore, surface reactions

most likely play a significant role in the set-up of the geopolymer matrix (van Jaarsveld et al., 2003). Since small particle size corresponds to greater surface area in aggregate, this might explain the increase in specimen strength related to eliminating larger size fractions. Using the BET method of nitrogen absorption, the specific surface areas of fly ashes are typically found in the range of 1,464 ft^2/lb to 2,440 ft^2/lb (300 to 500 m^2/kg) (Malhotra et al., 1989).

3) Although most geopolymers are typically based on low calcium fly ashes, the reactivity of high calcium material has also been investigated. The most immediately apparent effect of the addition of calcium is to increase the rate of set for the geopolymer. It is known that as the solution pH begins to decrease from 14 to lower values, the polycondensation reactions begin to occur (Lee and van Deventer, 2002). Calcium in the fly ash tends to precipitate as $Ca(OH)_2$ upon addition of the alkaline activation solution. As OH^- ions are removed from the activating solution, the pH falls and the solidification begins. van Deventer found that the Ca precipitates provide nucleation sites but also generate competition for crystal growth nutrients (van Deventer et al., 2007). Fe present in the source materials has a similar effect, precipitating as a hydroxide or oxy-hydroxide.
4) The bituminous coal that is most often burned in US steam plants typically produces an ash with SiO_2 in the range of 45-60% and Al_2O_3 in the range of 4-20% (Mehta, 1989). While this chemical composition besides the loss on ignition and the calcium content is not a determinant of pozzolanic activity, it is important in the development of geopolymers. The most effective ratio of silica to aluminum has been determined by Davidovits to be between 3.3 and 6.5 (1991).

This was confirmed by Sun in experiments that tested the strength of geopolymer specimens made with mortars that varied the ratio of silica to aluminum (Sun, 2005).

5) Although the x-ray fluorescence (XRF) method of chemical composition used in this research to determine the quantities of SiO_2 and Al_2O_3 are accurate and accepted, the portion of these oxides that participate in the geopolymer reaction is referred to as the "reactive" component. The proportion of reactive silica is reported as a ratio with total silica. The amorphous fraction of fly ash has been estimated between 60 and 80% of the total quantity. Of this amorphous fraction, 60-80% of the material is silicates and 10-20% is aluminates (Henry et al., 2004).

1.6 Activating solutions

The initiation of the geopolymerization phases described in the previous sections is caused by the addition of an activating solution to the source material. The solution contains the alkalinity that causes the dissolution of the source material solids and sometimes also contains a supplementary source of soluble silicates. Activating solutions must be carefully designed because their composition has several impacts on the development of the mechanical properties in the hardened geopolymer.

1.6.1 Alkali species

The two predominant alkaline salts used in geopolymer formation are NaOH and KOH. Each of these results in slightly different dissolution rates and hardened geopolymer characteristics. Greater dissolution rates for both Si and Al have been found

in solutions of NaOH. The impact of the more effective dissolution ability of NaOH solutions is that equilibrium of dissolved species and undissolved species is reached at lower levels of alkalinity (Panagiotopoulou et al., 2007). Comparison of the hardened properties of geopolymers formed with activating solutions containing either potassium or sodium have shown impacts to compressive strength and durability. Van Jaarsveld and van Deventer (1999) demonstrated that potassium activating solutions produced slightly higher compressive strength geopolymers. However, the potassium based activators also produced materials with higher specific surface area and lower resistance to acid attack.

1.6.2 Alkalinity level

The dissolution rates of aluminate and silicate species in the activating solution are affected by a combination of thermal conditions and the molarity of the alkaline solution. With both sodium and potassium based activating solutions, dissolution rates are known to increase with increasing alkalinity (Mikuni et al., 2007) (Sagoe-Crentsil and Weng, 2007). However, despite the dissolution capacity of higher alkalinity solutions, excessive presence of concentrations of sodium hydroxide have been found to reduce the compressive strength of hardened geopolymer. This is due to the reduced degree of polymerization that is caused by excessive NaOH concentrations. The balance of silicate species at high alkalinity levels tends to favor smaller monomers over the larger oligomers and therefore, less polycondensation (Panias et al., 2007).

1.6.3 Supplementary silica

The initial assembly of the alumino-silicate matrix is heavily controlled by the availability of aluminum. The supply of aluminum in the solution is known to dictate the setting time, durability and strength development (Duxson and Provis, 2008). However, the dissolution of the aluminum is dictated largely by the specific phases that exist in the source material. Because its bonds with oxygen in the source material are weaker, it tends to be provided more readily during dissolution. The activating solution can be a source of soluble silica for the reaction in order to either supplement the amorphous silica in the source material or to provide sufficient silica to the gel formation prior to it being made available through dissolution. Addition of soluble silica has been shown to increase the degree of polymerization in the hardened geopolymer and therefore improve the compressive strength (Criado et al., 2007).

1.7 Performance in structural elements

As the bulk of geopolymer research has been conducted on small specimens by material scientists and chemists, there are fewer reported studies on structural applications. Most data has been published on either neat geopolymer pastes or on geopolymer mortar. However, a small number of studies have been published on geopolymer concrete and geopolymer concrete in structural applications. The extension of geopolymer formation research to structural applications research involves investigating the binder as it is mixed with aggregates to form concretes. Once these materials are developed, the dimensions of research into structural uses include strength, durability, and performance in reinforced structural elements.

1.7.1 Interaction with other materials

In order to be used as structural concrete, geopolymer paste must interact with aggregates and reinforcing steel. The mechanical aspects of the cement-aggregate composite are of critical importance. Equally important is the bond with reinforcing steel.

1.7.1.1 Bond with aggregate

The interfacial transition zone (IZT) is the boundary between binder gel and aggregate in PCC as well as in GCC. A complex set of hydration processes affect the morphology of the IZT in PCC such that there is less gel present and the zone has greater porosity than gel at points away from the aggregate. In geopolymeric systems, the absence of hydration reactions and the much different hardening and curing process result in an IZT that is not as strongly affected. Lee et al. (2004) used a series of specimens with geopolymer paste bonded to polished slices of stone to measure the strength of the bond between the cement and aggregate. Samples were also examined under an electron microscope to determine the effect of the geopolymer materials on the mineralogy of the aggregate. It was found that systems activated with low soluble silicate activators formed low compressive strength bulk material and poor bonds with the stone (Lee and van Deventer, 2004). Materials with higher soluble silicate had denser binder phases and better bonds with the aggregates. The area near the aggregate surface had the same morphology as the bulk binder, indicating that there is not a heavily impacted ITZ as with PCC (Lee and van Deventer, 2004).

1.7.1.2 Bond with steel

The primary tensile reinforcement in concrete is present in the form of longitudinal bars or tendons. Stresses are transferred from the concrete to the tensile material through a bond at the surface. Prior to substantial loading, the bond consists of adhesion, friction and bearing. However, the first two of these mechanisms are typically broken after relatively low load application rates. Therefore, bearing is the only mechanism considered in the design process and reinforcing bars are deformed in order to improve the surface for stress transfer (MacGregor and Wight, 2005). ACI has given an equation to determine the development length for various sized bars in various strength concrete (ACI Committee 318. and American Concrete Institute., 2008).

$$l_d = \left(\frac{3}{40} \frac{f_y}{\lambda \sqrt{f_c'}} \frac{\psi_t \psi_e \psi_s}{\left(\frac{c_b + K_{tr}}{d_b} \right)} \right) d_b \qquad (1\text{-}4)$$

where:
l_d: development length
f_y: yield stress of bar
λ: lightweight concrete reduction factor
ψ_t: bar location factor
ψ_e: coating factor
ψ_s: bar diameter factor to favor smaller bars
c_b: factor representing concrete cover around bar
K_{tr}: concrete confinement across splitting planes
d_b: diameter of the reinforcing bar
f_c': concrete compressive strength

It can be seen from the terms in the equation that many of the factors affecting the development length of the reinforcing material are related to concrete properties that are similar for GCC and PCC. For instance, the term, $\left(\frac{c_b + K_{tr}}{d_b} \right)$, describes the propensity of beams to generate longitudinal cracks due to radial tensile forces transferred from the

steel to the concrete. Since the relationship between tensile and compressive strength for GCC and PCC are relatively similar, it is expected that they will have similar responses to these radial forces. The remaining geometric and tensile material surface and strength properties are also similar for GCC and PCC.

Sofi et al. (2007a) conducted tests to verify the bond performance of steel reinforcing materials with geopolymer concrete. The research group created geopolymer concretes from fly ashes from three steam generation units. The concretes were tested with the direct pull-out method given in American Society for Testing and Materials (ASTM) C 234-91 as well as the beam-end specimen method given in ASTM A 944-99 (ASTM, 1991; ASTM, 1999). It was found that the provisions given in ACI 318-02 and AS3600 for predicting development length are applicable to GCC.

1.7.2 Durability

1.7.2.1 Asr

In PCC, alkali-silica reaction is a threat to the durability of concretes containing expansive aggregates. Reactive aggregates are ones in which certain forms of silica engage in forming a swelling alkali-silicate-hydrate. This resulting gel attracts water and increases in size to cause cracks in the concrete (Mindess et al., 2003). Because of the high pH found in geopolymer pore solution, alkali-silica reaction ASR has been a concern for aggregates used in GCC. The performance of aggregates in GCC was investigated by Garcìa-Lodeiro, et al. (2007). ASR in several aggregates was measured by means of ASTM C1260-94 (ASTM, 1994). Concretes were produced with geopolymer cement as well as Portland cement and a range of reactive and sTABLE

aggregates. While all concretes exhibited some degree of expansion due to alkali-aggregate reactions, the alkali-activated fly ash systems exhibited less expansion than OPC systems with similar aggregates. The cause of the lesser expansion is speculated to be the low availability of calcium in class F fly ashes (Garcia-Lodeiro et al., 2007).

1.7.2.2 Creep

Creep behavior of GCC has been investigated by Wallah (2004). Concretes with compressive strength in the range of 5,800-10,000 psi (40 to 70 MPa) were prepared using two levels of alkalinity in the activating solution and two curing procedures. Half of the specimens were subjected to steam curing at 140°F (60°C) for 24 hours and the remaining specimens were cured at the same temperature, but under dry conditions. All specimens were loaded at a load intensity of 40% of the cylinder compressive strength. Specific creep levels ranged from 15 to 29 microstrain. Lower specific creep was found for concrete having higher compressive strength. Wallah (2004) determined that the measured creep in geopolymer specimens was uniformly less than creep strains predicted using the Gillbert model specified in the Austrailian code AS3600 (Standards Association of Australia., 2001).

1.7.2.3 Chemical resistance

Portland cement concretes are frequently degraded when exposed to aggressive chemical environments. This exposure may occur because they are intentionally exposed to elevated concentrations of chemicals due to the specifics of their intended service or unintentionally due to deleterious chemicals present in the environment. Sulfates and acids are two substances that can cause significant durability issues for concrete. When

exposed to sulfates, tri-calcium aluminate can form monosulfoaluminate. The reaction products occupy 55% more volume than the precursors, which causes stresses in the concrete. Further expansion can be caused by the reaction products absorbing water. Bakharev (2005) studied the sulfate resistance of geopolymer concrete by immersing specimens in solutions of sodium sulfate and magnesium sulfate. The changes caused by exposure to these sulfate solutions were of a different type than would be expected of Portland cement specimens. In the sodium sulfate solution, the alkali cations from the geopolymer matrix diffused out into the solution and caused significant microcracking. The magnesium sulfate solution caused magnesium and calcium to migrate into the matrix and improve the compressive strength (Bakharev, 2005a). As has been shown by other authors, the finer pore structure of geopolymers activated by sodium hydroxide results in materials that have lower susceptibility to attack in aggressive environments.

Acids can also cause problems in Portland cement mortars and concretes. As the calcium phases of the Portland cement hydration products are exposed to acid, calcium salts are formed which immediately weaken the material. Bakharev (2005) exposed geopolymer materials to acetic and sulfuric acid solutions to study their durability. The degree of degradation was linked to several factors of the geopolymer microstructure and chemistry. Polymer structures having lower Si/Al ratios were more heavily affected. Microstructural characteristics such as pore size and degree of polymerization were also correlated with greater resistance. Thus, geopolymers activated with potassium solutions had coarser pore structures and were more subject to degradation in the sulfuric acid. The most stable materials were geopolymers activated by sodium hydroxide and heat cured (Bakharev, 2005b).

1.7.3 Use in structural elements

Geopolymer cements have been used to create structural concretes by Hardjito and Rangan. In the course of their preliminary research, mixing procedures similar to those developed for Portland cement concrete (PCC) were used. The researchers found that PCC superplasticizers could be used effectively to manipulate the workability of the GCC. Concretes were produced with compressive strength in the range of 6,400-13,000 psi (44-90 MPa). The authors also measured Poisson's ratio and Young's modulus and found them to be similar to expected values for OPC concretes with comparable compressive strength (Hardjito and Rangan, 2005).

Sumanjouw et al. used fly ash geopolymer to build slender reinforced columns (Sumajouw et al., 2007; Sumajouw and Rangan, 2006). The concrete was cured at elevated temperatures and achieved compressive strengths of 5,800 and 8,700 psi (40 - 60 MPa). The columns were tested by loading to failure with eccentricities of 0.6", 1.4" and 2" (15, 35 and 50 mm). The failure modes were as expected, and the failure loads were predictable using formulas available in ACI 318-02 and AS3600 (ACI Committee 318. and American Concrete Institute., 2002; Standards Association of Australia., 2001).

Prestressed railway sleepers have been manufactured from geopolymer cement concrete. The geopolymer provides advantages in terms of fast strength development, allowing rapid turn-around and the ability to transfer prestress at an early concrete age. Palomo et al. (2007) has reported that the further benefits of geopolymer in this application include better durability under the harsh chemical and physical service environment of railway sleepers. The concrete also exhibits less drying shrinkage, and therefore lower prestress losses (Palomo et al., 2007).

Reinforced GCC columns have also been evaluated by Sarker (2009). The experimental results of testing GCC columns to failure were compared with analytical results. The columns were modeled with a moment-curvature relationship which relied on material properties determined by standard tests. A modified version of the Popovics stress-strain relationship was used to estimate the concrete compressive behavior (Popovics, 1973). The authors were able to predict the failure loads for the columns with a test/prediction ratio of 1.03, and the midspan deflections with test/prediction ratio of 1.14. This was seen as confirmation that conventional PCC design methodology may be applied to GCC applications (Sarker, 2009).

The engineering properties of GCC have been investigated by a limited number of research teams. In addition to the short supply of data regarding these characteristics, the composition of GCC materials is not consistent between the research groups. Therefore, the available data has a considerable spread, which is a result of the mortar fraction, aggregate type, activator composition and curing schedule that each author used.

1.8 Scope of research

The research presented in this dissertation is oriented towards developing a structural-grade concrete that is as energy and emissions efficient as possible. Further, the suitability of the concrete is demonstrated to the material producing community by the creation of typical and familiar structural elements. In order to develop an energy efficient concrete, mix designs were studied that incorporate varying quantities of virgin and recycled materials. After a structural strength (6,000-8,000 psi (41.4-55.1 MPa)) mix design was developed, its performance was tested through a variety of established material tests and structural component tests.

Fly ashes from multiple sources, collected at different times, were examined to determine the optimum mixing methods to account for their chemical and physical differences. Since a rigorous physical and chemical analysis of fly ash characteristics is beyond the scope of this research, a single source of fly ash was selected for use throughout the remainder of the project. The single source of fly ash was used to prepare concrete specimens and components. Small specimens were used to establish the material characteristics f'_c, E_c and f_{ct} via customary ASTM methods. Specimens were also created to test the durability characteristics, creep and shrinkage, which are critical in prestressed applications. Larger beam-column specimens were prepared in order to evaluate compressive stress response of the GCC. Finally, four mid-sized beams (10 ft (3m) in length) were created to verify geopolymer performance in reinforced concrete applications. Finally, three larger scale girders (18 ft (5.5m) in length) were produced from geopolymer to demonstrate geopolymer performance in prestressed concrete.

Following this work, the results provide an initial engineering characterization of geopolymer concrete structural components. The final analysis includes comparisons between the energy and material requirements to produce Portland cement concrete and those for producing geopolymer concrete.

CHAPTER 2: DEVELOPMENT AND OPTIMIZATION OF GEOPOLYMER CEMENT CONCRETE MIX DESIGNS

The source materials for geopolymer cement concrete (GCC), as with Portland cement concrete (PCC) are local in their origin. The primary cementitious component, fly ash, is a byproduct of coal combustion which is captured by emissions control devices at power generation stations. As such, its composition is highly dependent on a range of variables including the mine where the coal was collected and the operational particulars of the furnace that burned it. In order to begin GCC research at UNC Charlotte, an initial exercise in collecting and characterizing the source materials was undertaken. This chapter describes the following research activities:

1) Developing activating solution and aggregate proportions for GCC
2) Optimizing the aging and curing routine
3) Scaling up to larger batches
4) Determining the modulus of elasticity of the concrete
5) Determining the splitting tensile strength of the concrete

The research presented in this dissertation required the development and implementation of several types of material preparation and experimental techniques. Some of the techniques are based on existing and accepted material testing methods put forth by the American Society for Testing and Materials (ASTM). Whenever possible, existing test methods were used so that the geopolymer concrete may be more readily accepted by the materials production and construction communities. In other cases, no

suitable existing method was available and attempts were made to develop appropriate and reliable procedures for the purposes of this project.

2.1 Development of activating solution and aggregate proportions

2.1.1 Determining requisite ash quality

In the summer of 2008, a series of experiments was conducted on a range of fly ashes available in proximity to Charlotte, North Carolina. The goal in completing these tests was to arrive at a baseline set of mix designs and to determine the qualities of local ashes that indicated their acceptability for geopolymer manufacture. In the first phase, ashes came from two primary local sources, designated MA and BL.

Oxide analysis via XRD was carried out by an external lab and yielded the compositional data in TABLE 2-1. As can be seen from the results, the ashes contained Si/Al ratios of roughly 2:1. The MA ashes had very high carbon content as evidenced by a measured loss on ignition (LOI) of 10%. The BL ashes had much lower LOI, with only 3.3% carbon.

A mix proportioning methodology was designed, which is organized in a similar manner to that developed by Sun (2005). Various combinations of NaOH and Silica Fume were used to create the activating solution. The specific proportions for the activating solution used in this study are presented in TABLE 2-2. The quantities of NaOH and silica fume are presented as ratios to the weight quantity of fly ash used, which was 8.50 lb (3.90 kg) in all cases. The water content was adjusted so that despite the increasing quantity of activating solids (NaOH and silica fume) the ratio between cementitous materials (activating solids and fly ash) and water was always 0.40.

TABLE 2-1: Fly ash composition.

% By Mass	MA	BL
SiO_2	51.51	54.92
TiO_2	1.34	1.44
Al_2O_3	26.11	31.28
Fe_2O_3	6.05	4.8
MnO	0.02	0.01
MgO	0.85	0.77
CaO	1.22	0.83
Na_2O	0.27	0.31
K_2O	2.38	2.25
P_2O_5	0.2	0.1
LOI	10.05	3.29

TABLE 2-2: Activator design for preliminary batches.

Mix ID	NaOH/Fly Ash	Silica Fume/Fly Ash	Water, lb (kg)
MA1	0.1	0.075	3.98 (1.81)
MA2	0.16	0.075	4.19 (1.90)
MA3	0.19	0.075	4.31 (1.95)
MA4	0.1	0.1	4.07 (1.84)
MA5	0.16	0.1	4.28 (1.94)
MA6	0.19	0.1	4.39 (1.99)
BC1	0.19	0.05	4.22 (1.92)
BC2	0.16	0.05	4.11 (1.87)
BC3	0.13	0.075	4.09 (1.86)
BC4	0.16	0.075	4.19 (1.90)
BC5	0.13	0.1	4.18 (1.89)
BC6	0.16	0.05	4.11 (1.87)

The aggregates used in this phase of the work were sourced from local quarries. The coarse aggregate was a 3/8", granite stone and the fine aggregate was silica concrete sand. The gradation for these aggregates is given in TABLE 2-3. The quantity of aggregate used was proportioned so that it accounted for roughly 80% of the total mass of the concrete. This ratio is typical of OPC concretes.

TABLE 2-3: Gradation of fine and coarse aggregates.

Sieve Opening	% finer	
	Coarse	Fine
5/8	100.0	100
1/2	99.5	100
3/8	85.3	99.77
no. 4	28.8	99.54
no. 8	5.5	97.94
no. 16	1.3	90.37
no. 40	0.7	37.16
no. 50	0.7	19.95
no. 100	0.5	1.61
Pan	0.0	0.00

2.1.2 Results of preliminary tests

The results of the preliminary tests are partly anecdotal and partly quantitative. Although none of the mixes developed strength in the desired range of 4,500-6,000 psi (27.5-41.3 MPa) for structural use, there were clear trends in the relationship between the

activator solution make-up and strength development. This information was useful in the development of subsequent procedures.

2.1.2.1 Activating solution proportions

The two ashes used in the preliminary tests had very different physical and chemical characteristics and produced concretes with various compressive strengths. In general, the MA ashes produced lower strength concrete than the BL ashes. This might be attributable to the very high LOI of the MA ashes. Despite the difference in strength produced, both ashes showed improved strength development associated with similar activating solution compositions. In this series of experiments, two variables were systematically manipulated- the ratio of NaOH to fly ash and the ratio of Silica Fume to fly ash. The mix proportions shown in TABLE 2-2 were used. 11.2 lb (5.1 kg) of coarse aggregate and 11.2 lb (5.1 kg) of fine aggregate were used in each batch.

Generally, nine 3”x6” (76mmx152mm) cylindrical specimens were made from each batch. These were tested in compression after seven and twenty-eight days. The results of the compression tests are shown in TABLE 2-4. The experiments revealed some important trends in the activator design and the development of compressive strength. As is shown in FIGURE 2-1 and FIGURE 2-2, compressive strength increased up to the NaOH/Fly Ash ratio of 0.15 and then decreased for higher alkalinity solutions. Strength also increased with the addition of silica fume to the activating solution. However, the limited number of data points does not indicate an optimal amount of silica fume for strength development. As is shown in FIGURE 2-3, there is no peak in the strength vs. silica fume addition for the ratios tested.

The compressive strength results given in TABLE 2-4 show uniformly higher values for the BL ashes over the MA ashes. Since the oxide composition of the two ashes was very similar and the preparation and proportioning of the concrete was also alike, the main difference seems to be the LOI. In the case of the MA ashes, the high LOI seemed to inhibit the development of compressive strength in the cylinders. The appearance of the cylinders also seemed to be affected by the high carbon content. Whereas the cylinders prepared with BL ashes had a grayish color very similar to PCC, the MA cylinders were very dark.

TABLE 2-4: Compressive strength of concretes made with BC and MA ashes.

Mix ID	f_c' , psi (MPa)
MA1	476 (3.3)
MA2	2,031 (14.03)
MA3	1,854 (12.8)
MA4	986 (6.8)
MA5	2,680 (18.5)
MA6	2,158 (14.9)
BC1	1,265 (8.7)
BC2	2,883 (19.9)
BC3	1,285 (8.9)
BC4	2,006 (13.8)
BC5	2,521 (17.4)
BC6	3,207 (22.1)

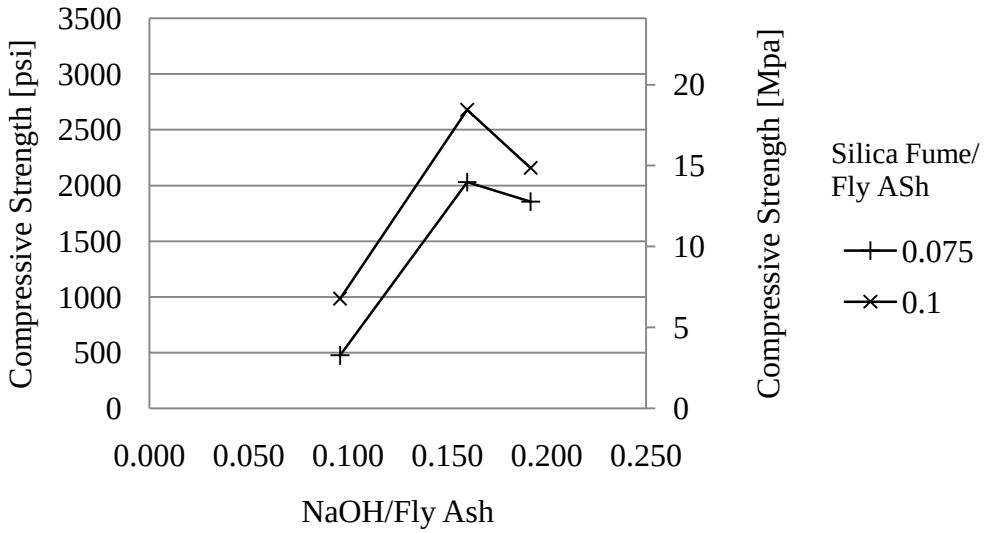

FIGURE 2-1: Optimum NaOH Addition For MA Ashes.

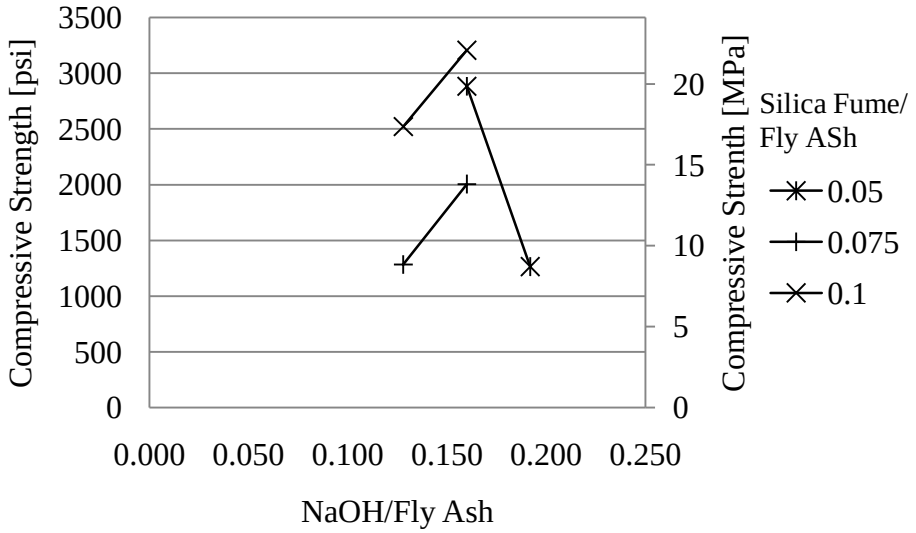

FIGURE 2-2: Optimum NaOH Addition For BL Ashes.

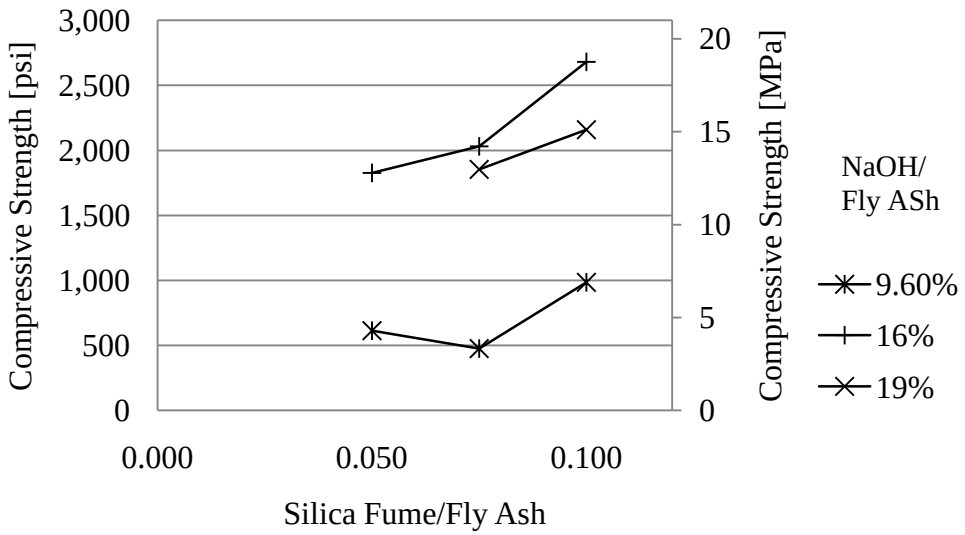

FIGURE 2-3: Activator Design and 7-Day Strength for MA Ashes.

Although the results did not provide sufficient data for strong conclusions about geopolymer mix design, they did set the stage for further testing. The following guidelines were established from the first tests:

1) Future activator designs should incorporate more silica fume
2) Only class F fly ashes should be used
3) The total quantity of cementitious solids (NaOH, silica fume, fly ash) should be held constant rather than simply the fly ash quantity. This will result in constant batch masses and fewer variables between batches.
4) The w/c ratio has a significant role in strength determination and should be held as low as possible. Experiments should be performed to determine a target w/c ratio for workability and strength development.

2.2 Further mix development

In the second round of tests, the lessons learned from round one were applied. Here, the w/c ratio was to be studied and controlled more closely and the mix designs used in the experiments were adjusted to include more silica fume. Higher grade fly ash was also used in these experiments.

2.2.1 New fly ash

For the second round of tests, fly ashes of more verifiable quality were collected. These were from sources specifically designated for concrete use and were marketed by the supplier as Class F. Once these ashes were collected, they were designated BC and CL. An XRF analysis was completed and provided the results shown in TABLE 2-5. The ash was collected and stored in sealed 55 gallon steel drums.

TABLE 2-5: XRF analysis of BC and CL ashes.

% by Mass	BC	CL
SiO_2	58.08	56.20
TiO_2	1.56	1.46
Al_2O_3	28.63	28.00
Fe_2O_3	4.12	5.22
MnO	0.02	0.02
MgO	0.94	1.00
CaO	0.74	1.52
Na_2O	0.22	0.21
K_2O	2.44	2.74
P_2O_5	0.10	0.18
Totals	96.85	96.55
LOI	3.03	3.32

2.2.2 W/c ratio

The importance of the water/cement ratio was not fully appreciated until late in the experimental process. In the first round of tests, water was often added in a measured, however, liberal manner. The relationship between strength gain and w/c ratio from the first batch of tests is shown in FIGURE 2-4. The data points plotted in this chart include many activator compositions. However, despite the concurrent representation of a wide range of factors, a clear trend toward higher strength at lower w/c ratios is apparent.

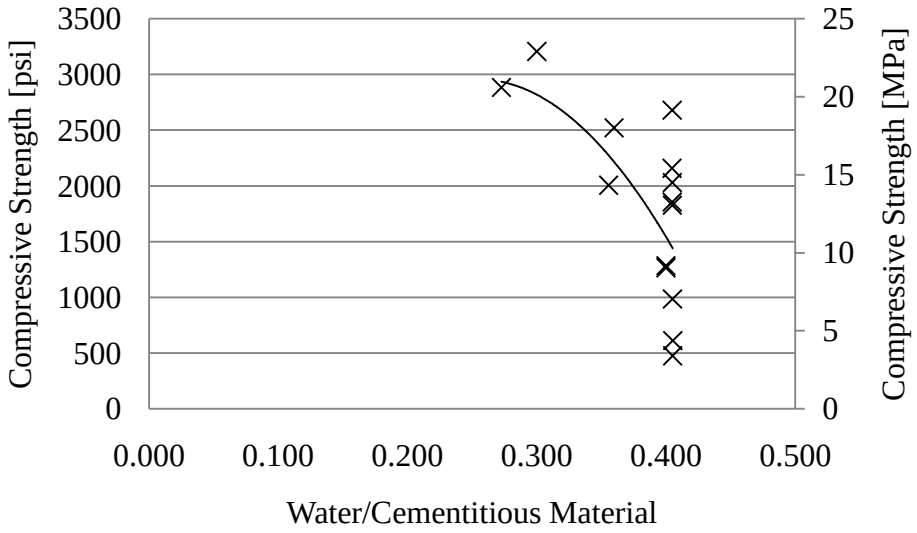

FIGURE 2-4: w/c ratio and 28-day compressive strength.

Following the discovery of the importance of water content, several more small batches of concrete were produced with known w/c ratios. In this experiment, concretes with the proportions shown in TABLE 2-6 were prepared by mixing by hand. In these specimens the variables were water content and the ratio of NaOH to fly ash. The

strength development results can be seen in FIGURE 2-5. For both activating solution concentrations, there was an improvement in strength achieved by reducing the w/c ratio. For the 0.13 NaOH/Fly ash activating solutions, the strength development with reduced water content was more pronounced.

TABLE 2-6: Mixing proportions for w/c ratio specimens, lb (kg).

NaOH/Fly Ash	Silica Fume	NaOH	Fly Ash	Fine Aggregate	Coarse Aggregate
0.10	0.2 (0.091)	0.3 (0.1361)	3.1 (1.41)	3.7 (1.68)	3.7 (1.68)
0.13	0.2 (0.091)	0.4 (0.181)	3.1 (1.41)	3.7 (1.68)	3.7 (1.68)

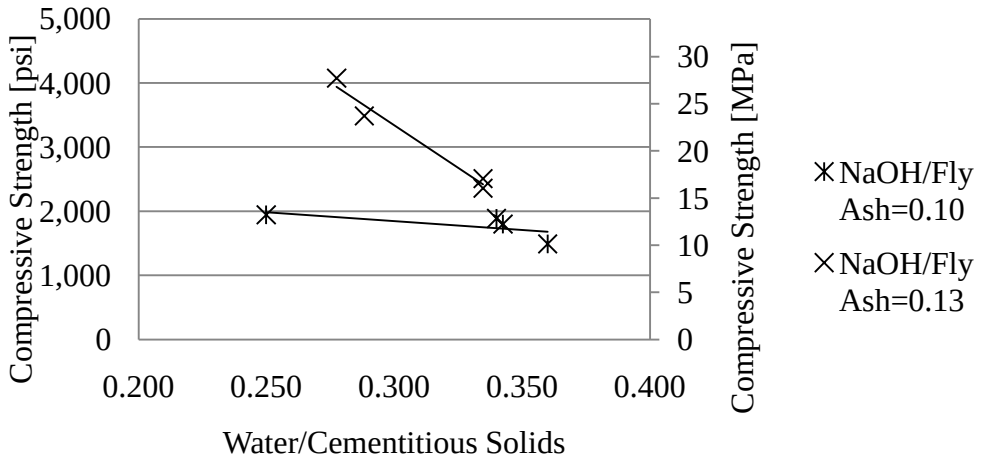

FIGURE 2-5: w/c ratio and strength development for two activator concentrations.

Although quantitative tests for workability were not used during the water content experiments (due to the reactivity of the aluminum test equipment), qualitative

assessments were made. The workability of mixes with w/c ratios below ~0.27 was very poor. These concretes were difficult to mix and to mold into suitable specimens. Therefore, the w/c ratio selected for subsequent tests was 0.28. This low w/c ratio required the use of high range water reducer.

Based on lessons learned in the previous series of tests, the experiment parameters for the activator mix design were set as is shown in TABLE 2-7. Each batch included 11.2 (5.1 kg) and 11.5 lb (5.2 kg) of fine and coarse aggregate, respectively. Following the conclusions from the water content tests described above, the w/c ratio was fixed at 0.28, where weight of cementitous solids includes the sum of the fly ash, silica fume and sodium hydroxide. In each batch, the total weight of cementitious solids is constant, although the relative proportions of fly ash, silica fume and sodium hydroxide change in each activator design. 10 ml of ADVA 190 superplasticizer was used in each batch.

Nine cylinders were made from each batch. Three were tested at seven days and three were tested at 28 days using the procedures for compression tests given in ASTM C39 (ASTM, 2005). The remaining three were retained as alternates in case there were problems with any of the tests. The results of the compression tests are given in TABLE 2-9. In the TABLE, “No Data” implies that there was a problem mixing the batch and no cylinders were created. This typically occurred with the higher alkalinity mixes that were either not workable enough to create cylinders, or set-up in the mixer.

There are general similar trends for concretes made from the two types of fly ash. As shown in TABLE 2-5, the chemical composition of BC and CL ashes is very similar, although they were produced at different steam stations. The results were analyzed to

determine trends in strength development and to select the best activator design for future work.

TABLE 2-7: Mix Designs, lb (kg).

Activator #	NaOH/ Fly Ash	Silica Fume/ Fly Ash	Fly Ash	Water	Silica Fume	NaOH
10	0.1	0.08	11.1 (5.05)	3.7 (1.68)	0.89 (0.4)	1.11 (0.5)
11	0.1	0.11	10.8 (4.91)	3.7 (1.68)	1.19 (0.54)	1.08 (0.49)
12	0.1	0.14	10.6 (4.82)	3.7 (1.68)	1.48 (0.67)	1.06 (0.48)
13	0.13	0.08	10.8 (4.91)	3.7 (1.68)	0.87 (0.4)	1.41 (0.64)
14	0.13	0.11	10.6 (4.82)	3.7 (1.68)	1.16 (0.53)	1.38 (0.63)
15	0.13	0.14	10.3 (4.68)	3.7 (1.68)	1.45 (0.66)	1.34 (0.61)
16	0.16	0.08	10.6 (4.82)	3.7 (1.68)	0.85 (0.39)	1.69 (0.77)
17	0.16	0.11	10.3 (4.68)	3.7 (1.68)	1.14 (0.52)	1.65 (0.75)
18	0.16	0.14	10.1 (4.59)	3.7 (1.68)	1.41 (0.64)	1.62 (0.74)
19	0.19	0.08	10.3 (4.68)	3.7 (1.68)	0.83 (0.38)	1.96 (0.89)
20	0.19	0.11	10.1 (4.59)	3.7 (1.68)	1.11 (0.5)	1.92 (0.87)
21	0.19	0.14	9.9 (4.5)	3.7 (1.68)	1.38 (0.63)	1.87 (0.85)
22	0.16	0.16	9.9 (4.5)	3.7 (1.68)	1.6 (0.73)	1.6 (0.73)
23	0.16	0.18	9.8 (4.45)	3.7 (1.68)	1.8 (0.82)	1.6 (0.73)

TABLE 2-8: Ratios of NaOH to silica fume for optimal strength development.

NaOH/Fly ash	BC	CL
0.10	1.3	1.3
0.13	1.6	1.2
0.16	1.1	2.0
Average	1.41	

TABLE 2-9: Compression test results for geopolymer made from BC and CL ashes.

Mix ID	NaOH/ Fly Ash	Silica Fume/Fly Ash	7-Day Strength psi (MPa)	28-Day Strength psi (MPa)	Standard Deviation
BC-10	0.1	0.08	3,405 (23.5)	4,131 (28.5)	88.5
BC-11	0.1	0.11	2,482 (17.1)	3,157 (21.8)	30.3
BC-12	0.1	0.14	671 (4.6)	1,042 (7.2)	4.7
BC-13	0.13	0.08	4,933 (34)	5,558 (38.3)	77.3
BC-14	0.13	0.11	4,780 (33)	5,241 (36.1)	262.9
BC-15	0.13	0.14	2,402 (16.6)	2,908 (20.1)	155.0
BC-16	0.16	0.08	2,530 (17.4)	3,136 (21.6)	157.4
BC-17	0.16	0.11	5,096 (35.1)	5,454 (37.6)	196.2
BC-18	0.16	0.14	7,068 (48.7)	7,064 (48.7)	89.0
BC-19	0.19	0.08	4,554 (31.4)	4,644 (32)	657.4
BC-19b	0.19	0.08	3,846 (26.5)	No Data	
BC-20	0.19	0.11	6,777 (46.7)	No Data	
BC-21	0.19	0.14	6,621 (45.7)	No Data	
BC-22	0.16	0.16	5,368 (37)	6,264 (43.2)	98.1
BC-23	0.16	0.18	4,818 (33.2)	5,308 (36.6)	138.3
CL-10	0.1	0.08	6,620 (45.6)	7,625 (52.6)	193.1
CL-11	0.1	0.11	4,613 (31.8)	5,683 (39.2)	200.9
CL-12	0.1	0.14	2,117 (14.6)	2,728 (18.8)	37.2
CL-13	0.13	0.08	8,593 (59.2)	9,122 (62.9)	367.9
CL-14	0.13	0.11	9,833 (67.8)	1,0665 (73.5)	353.0
CL-15	0.13	0.14	8029 (55.4)	8962 (61.8)	440.0
CL-16	0.16	0.08	9459 (65.2)	10337 (71.3)	327.9
CL-17	0.16	0.11	8592 (59.2)	8956 (61.7)	209.1
CL-18	0.16	0.14	9835 (67.8)	10281 (70.9)	158.5
CL-19	0.19	0.08	No Data	No Data	

Mix ID	NaOH/ Fly Ash	Silica Fume/Fly Ash	7-Day Strength psi (MPa)	28-Day Strength psi (MPa)	Standard Deviation
CL-20	0.19	0.11	6501 (44.8)	No Data	
CL-21	0.19	0.14	8062 (55.6)	No Data	
CL-22	0.16	0.16	7413 (51.1)	8153 (56.2)	96.3
CL-23	0.16	0.18	7224 (49.8)	8016 (55.3)	150.0

2.2.3 Strength development

2.2.3.1 CL ashes

The CL ashes produced their highest compressive strength concrete of 10,665 psi (73.5 MPa) with activator #14, which is characterized by 0.13 NaOH/fly ash and 0.11 silica fume/fly ash. The plotted results of the compressive strength tests shown in FIGURE 2-6 indicate that 0.13 and 0.16 NaOH/fly ash activator solutions produce approximately the same results. There is no clear trend towards a peak strength at either of these two alkalinity levels. FIGURE 2-8 shows that for the lower alkalinity concrete mixes, greater amounts of silica fume were associated with increased development of compressive strength between the 7^{th} and 28^{th} day.

The average coefficient of variation for cylinders made in this series is 2.7%. Although ASTM does not publish guidelines for “within-test precision” for 3”x6” (76mmx152mm) cylinders, its acceptable coefficient of variation for 4”x8” (102mmx205mm) cylinders is 3.2% (ASTM, 2005). This indicates that the cylinders were made uniformly within tolerances set forth by ASTM.

2.2.3.2 BC ashes

The BC ashes produced the highest compressive strength concrete with activator #18, characterized by 0.16 NaOH/fly ash and 0.14 silica fume/fly ash. This resulted in a strength of 7,064 psi (48.7MPa). As is seen in

FIGURE 2-7, strength results for this mix up to and past the optimum form a clear peak. Data for the other activator designs are less clear in their trends because the lower part of the curve is missing.

The average coefficient of variation for compressive strength of cylinders made from BC ashes was 3.6%. This includes BC-19, which had a strong outlier. If this batch is removed from the data, the average coefficient of variation is 2.7%.

2.2.3.3 General trends

Since the overall objective of these experiments was to discover the optimum activator design to achieve structural strength concrete, it is necessary to study general trends in strength development between the two fly ash types used.

Strength Development Over Time

As is evident from FIGURE 2-8 and FIGURE 2-9, there is the greatest 7-28 day strength gain in concretes made with the lower alkalinity activator solutions. For BC ashes, this increase ranged from <2% for activator #19, which is characterized by 0.19 NaOH/fly ash and 0.08 silica fume/fly ash. The greatest 7-28 day strength gain in BC ashes was >35% and occurred in the batch made with activator #12 , which is characterized by 0.10 NaOH/fly ash and 0.14 silica fume/fly ash. The same trend held true for CL ashes, where the average strength gain for the 0.10 NaOH/fly ash activators

was 18%, 8% for the 0.13 activators and 6% for the 0.16 NaOH/fly ash activators. This indicates that, while lower alkalinity activating solutions produce lower final compressive strengths, there is a greater degree of strength gain over the course of the first month than with higher alkalinity activating solutions.

Another disadvantage of the higher alkalinity activating solutions was found to be reduced workability. Several times, activators with the 0.19 NaOH/Fly ash ratios caused concrete to set-up in the mixer before cylinders could be made. When the concrete was workable enough to produce cylinders, these were always of lower visual quality than cylinders made with lower alkalinity activating solutions. These had variations in color as well as more small voids near the surface. Overall, the results of using the high alkalinity solutions were less predictable.

For the same activator solutions, CL ashes tended to produce stronger concretes than the BC ashes. Because their chemical compositions as determined by XRF are very similar, there is no data available on which to speculate about the cause of this trend. In the literature, researchers have determined that amorphous content and particle size are important factors in fly ash performance as a source material for geopolymer (Sun, 2005; van Jaarsveld et al., 2003). Tests for these two features were not been completed, but might illuminate the difference in strength development.

For both sets of ashes, the results indicate that as the alkalinity of the solution increases, additional silica fume is also required to generate the maximum improvement in compressive strength. Although the strength results plotted in FIGURE 2-6 and

FIGURE 2-7 do not indicate a clear trend, when viewed in tabular form as in TABLE 2-8, they are more appreciable.

This indicates that the optimal strength is developed with the activating solution containing a mass ratio of NaOH to silica fume of 1.41. If the process for producing the sodium silicate solution used in these experiments follows the reaction shown in Equation (2-1), the weight ratio should be 1.3.

$$2NaOH + SiO_2 + H_2O \rightarrow Na_2O + SiO_2 + 2H_2O \quad (2\text{-}1)$$

2.3 Conclusions

1) Activators other than those with NaOH/silica fume ratios near 1.4 need not be tested.
2) The 0.19 NaOH/fly ash activators should not be tested further as they do not produce workable mixes.
3) The w/c ratio of 0.28 can produce workable concretes if superplasticizer is added to the mix.
4) Ashes from the CL source should be used for further work as they seem to produce stronger concrete.

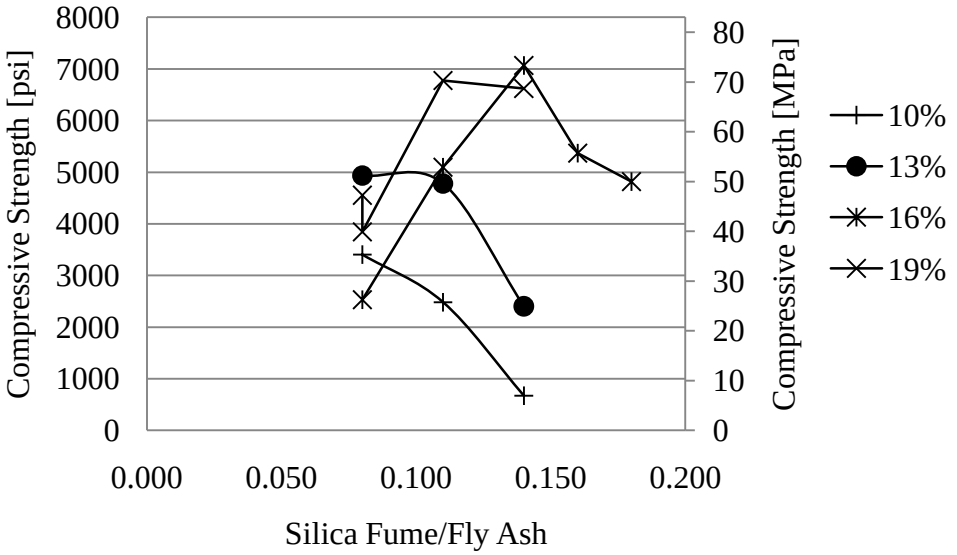

FIGURE 2-6: Activator Design and 28-Day Strength for CL Ashes.

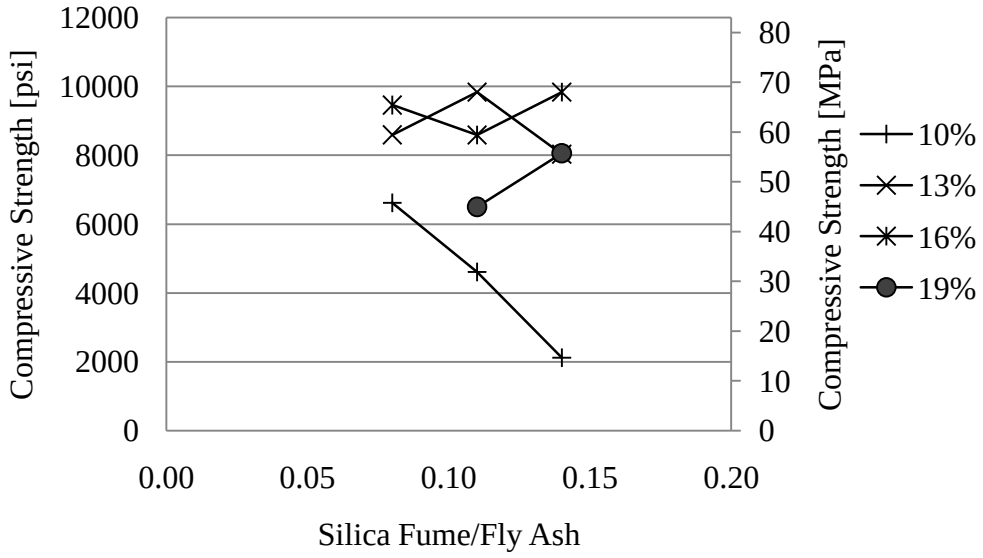

FIGURE 2-7: Activator design and 28-day strength for BC ashes.

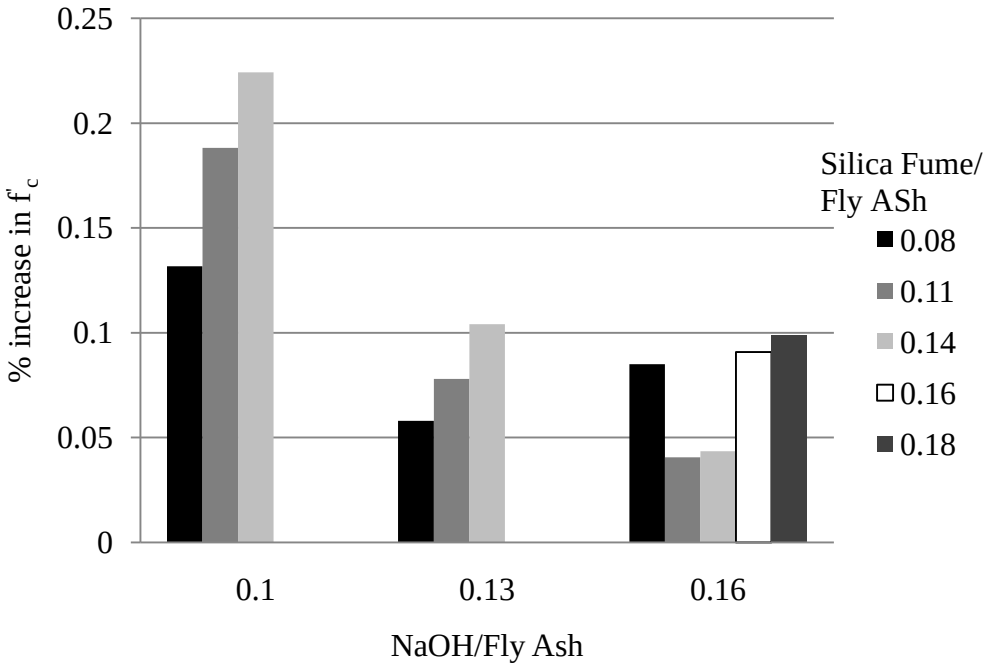

FIGURE 2-8: Increase in compressive strength between day 7 and day 28 for CL ashes.

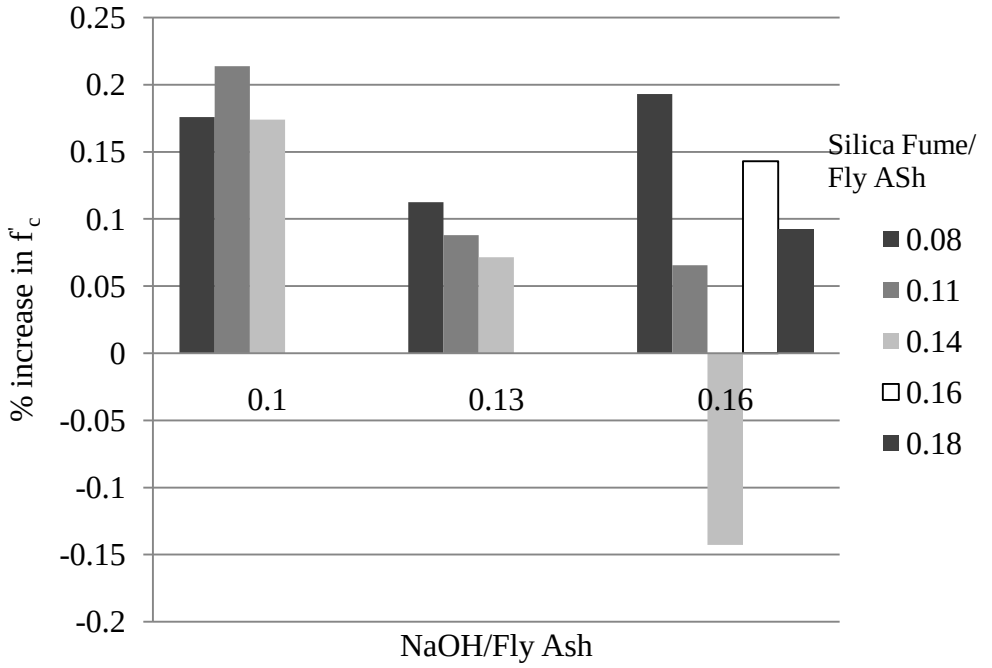

FIGURE 2-9: Increase in compressive strength between day 7 and day 28 for BC ashes.

2.4 Preparation of concrete materials for constitutive property characterization

Following the development of the guidelines presented in the previous section, several batches of GCC material were prepared in order to generate data on the constitutive properties of the concrete.

2.4.1 Fly ash

Fly ashes used in these experiments were sourced from a southeastern steam station. They were collected in a silo used for distribution of concrete-grade, Class-F ashes to tanker trucks, as shown in FIGURE 2-10. This allowed them to be transported and stored in a dry condition to preserve their reactivity. Depending on the quantity sampled for research, the ashes were stored in a variety of containers including 3 cubic yard hoppers (2.3 cubic meter), 55 gallon steel drums (208 l) and 2 ton (1.8 tonne), polyethylene lined tote sacks. The ash oxide characteristics are described in TABLE 2-10 as determined by XRF analysis. As many ashes were used in the course of this research, these ashes are identified by the initials "CL."

2.4.2 Aggregates

The aggregates used in this phase of the work were sourced from local quarries. The coarse aggregate was a 3/8", granite stone and the fine aggregate was silica concrete sand. The gradations for these aggregates are given in TABLE 2-3.

FIGURE 2-10: Fly ash storage silo.

TABLE 2-10: XRF analysis of CL ashes.

% by Mass	CL
SiO_2	56.20
TiO_2	1.46
Al_2O_3	28.00
Fe_2O_3	5.22
MnO	0.02
MgO	1.00
CaO	1.52
Na_2O	0.21
K_2O	2.74
P_2O_5	0.18
Totals	96.55
LOI	3.32

2.5 Mixing process

1) Preparing the Activating Solution

The sodium silicate activating solution is prepared by mixing the required amount of sodium hydroxide in the specified amount of water, as is demonstrated in FIGURE 2-11. Next, the silica fume is added slowly. The reaction between the silica fume and the sodium hydroxide is fairly violent and requires that additions be made slowly. After all the silica fume is included, the solution is mixed for two minutes at low speed with a paddle stirrer mounted in a hand drill. The sodium silicate solution is placed in a polyethylene pitcher, partially sealed and placed in a 167° F (75° C) oven overnight (~20 hours). A small amount of water 0.4-0.6 lb (200-500g) is usually withheld from the activating solution so that it can be used to disperse any admixtures through the dry ingredients immediately prior to mixing. Adding this small amount of mixing water also helped reduce the dust and fly ash leaving the mixer.

2) Preparing the Aggregate

The coarse aggregate is brought to a saturated-surface-dry condition by soaking it overnight in tap water and then drying the surface of the stones with terrycloth towels. The fine aggregate is oven-dried at 167 ° F (75° C) overnight. Immediately before mixing, the aggregates and fly ash are measured out in the proportions specified for the mix under consideration, as is demonstrated in FIGURE 2-12.

3) Mixing the concrete

The dry ingredients are added to the mixer with the mixing water and admixtures, and the mixer is started. After a two minute mixing session the activating solution is

added to the dry ingredients, seen in FIGURE 2-13. Because the batches being created are fairly small, sometimes the material is tilled by hand in order to eliminate dry pockets in the mixer. Once the activating solution is thoroughly dispersed (as evidenced by no more dry pockets), the mixer is allowed to operate for five minutes.

4) Making Cylinder Specimens

Once mixed, the concrete is placed in 3"x6" (76mmx152mm) plastic cylinder molds as per the ASTM C192, "Standard Practice for Making and Curing Concrete Test Specimens in the Laboratory" (ASTM, 2007) . Cylinders are consolidated by rodding, as shown in FIGURE 2-14. The cylinders are left to age at room temperature for a specified time period before being placed in a 167° F (75° C) oven for the elevated temperature curing period, as is shown in FIGURE 2-15. Following elevated temperature curing, the cylinders are conditioned at ambient indoor conditions until required for testing.

FIGURE 2-11: Preparing activating solution.

FIGURE 2-12: Measuring aggregates.

FIGURE 2-13: Adding activating solution.

FIGURE 2-14: Consolidating geopolymer concrete in 3X6" cylinders.

FIGURE 2-15: Oven for curing geopolymer concrete specimens.

2.6 Experimental procedures

Three 1.5 ft^3 (0.04 m^3) batches of geopolymer concrete were made in the lab. The aggregates used were the same as described in TABLE 2-3. The proportions for the three batches are presented in TABLE 2-11. For mix #1 and #2, 60 3"x6" (76mmx152mm) cylinders were made. 18 cylinders were made for mix # 3. Mixing was performed in a 3ft^3 (0.08 m^3) rotary mixer according to the procedure described in the previous section. Procedures for creating the cylinders followed ASTM C192 (ASTM, 2007). For consistency, the step of vibrating all the cylinders for 1 minute after rodding was added.

TABLE 2-11: Mixing proportions lb/yd^3 (kg/m^3).

Mix #	1	2	3
Fly Ash	834 (495)	798 (474)	766 (455)
Water	274 (163)	274 (163)	274 (163)
NaOH	83 (49.5)	103 (61.6)	122 (72.7)
Silica Fume	62 (37.1)	77 (46.2)	91 (54.5)
Fine Aggregate	1336 (793)	1336 (793)	1336 (793)
Coarse Aggregate	1336 (793)	1336 (793)	1336 (793)

TABLE 2-12: Number of cylinders made for each aging and curing regimen.

Aging	Curing	
	24 hours	48 hours
0 hours	10	10
24 hours	10	10
48 hours	10	10

The cylinders were aged and cured according to the schedule presented in TABLE 2-12. The aging process occurred under ambient conditions in the structures lab at UNC Charlotte. After the cylinders were made, the 0-hour aging batch was placed directly in the 167°F (75°C) curing oven. The other cylinders were left out in the lab and added to the oven after either 24 or 48 hours of aging. Cylinders were demolded immediately after they were removed from the oven and were stacked on a pallet under ambient conditions in the lab until testing on the 28th day.

From each batch and curing group, three cylinders were tested in compression in accordance with ASTM C39, three were tested in splitting according to ASTM C496 and three were tested for the static modulus of elasticity according to ASTM C469 (ASTM, 2002a; ASTM, 2004b; ASTM, 2007). The procedures were carried out on a universal testing machine at UNC Charlotte as depicted in FIGURE 2-16 and FIGURE 2-17.

FIGURE 2-16: Splitting tensile test set-up.

FIGURE 2-17: Static modulus of elasticity test set-up.

2.7 Material characteristics tests results

The compression tests revealed that the material strength ranged from a minimum of 4,700 psi to a maximum of 9,800 psi (32-68 MPa). The results show that strength development is related to all three variables that were manipulated in this experiment: activator concentration, aging time and curing time. These results verify trends found by other researchers as well as provide insight into their interrelation.

The average mix strength was highest for the Mix 2 group and lowest for the Mix 3 group. Thus, strength seemed to improve when the alkalinity of the activating solution was increased from 10% NaOH/fly ash to 13% NaOH/fly ash, but declined when the alkalinity was further increased to 16% NaOH/fly ash. Despite these general trends with strength development related to the alkalinity of the activating solution, there is an important influence from the aging and curing schedule.

The results presented in TABLE 2-13 show two main trends in strength development for the aging and curing routines used in this course of experiments. Increasing aging time from 0 to 2 days improved the 28-day compressive strength in all cases. Increased curing time at 167° F (75° C) also improved the 28 day strength in all cases. These results are illustrated in FIGURE 2-18. For the Mix 1 specimens, high temperature curing for an additional day improved the compressive strength an average of 12%. For these same specimens, the impact of additional aging was an average of 6% increase in compressive strength. For the Mix 2 specimens, the effect of additional high temperature curing time was an average compressive strength increase of 13%. The impact of additional aging time on these specimens was an increase of strength by 8% on average. Mix 3 showed the greatest improvement in strength with both increased aging time and 24 hours of curing. However, the maximum strength was achieved for Mix 2.

FIGURE 2-18 also shows that there might be room for further improvement in compressive strength by aging the specimens for more than two days prior to heat curing. Whereas the improvement in strength for Mix 1 has leveled off by day two, Mixes 2 and 3 appear to still be increasing at day two. Further experimental work would be required to examine this trend.

TABLE 2-13: Results of compression and tension tests.

Mix #	Aging Time (days)	Curing Time (hours)	f'_c psi, (MPa)	f_t psi, (MPa)
1	0	24	5,302 (37)	474 (3.3)
1	0	48	6,010 (41)	558 (3.9)
1	1	24	5,915 (41)	420 (2.9)
1	1	48	6,465 (45)	544 (3.8)
1	2	24	5,939 (41)	485 (3.3)
1	2	48	6,978 (48)	550 (3.8)
2	0	24	7,356 (51)	708 (4.9)
2	0	48	7,983 (55)	764 (5.3)
2	1	24	7,732 (53)	555 (3.8)
2	1	48	9,308 (64)	696 (4.8)
2	2	24	8,287 (57)	879 (6.1)
2	2	48	9,787 (67)	851 (5.9)
3	0	24	4,708 (32)	
3	0	48	6,336 (44)	
3	1	24	6,171 (43)	
3	1	48	6,780 (47)	
3	2	24	7,926 (55)	
3	2	48	8,094 (56)	

The benefit of aging for longer periods versus curing for longer periods is demonstrated in FIGURE 2-19 through FIGURE 2-21. Mixes 1 and 2 both showed compressive strength gains of approximately 25% through the combination of increased aging and curing periods. By comparing the batches that were aged for 0 days and cured for 24 hours with those aged for 2 days and then cured for 24 and 48 hours, it is possible to determine the effect of each process on the final strength development. These differences are illustrated in FIGURE 2-19 by the regions labeled “A” and “B.” Region “A” is the difference in compressive strength of cylinders that were aged for 0 days and cured for 24 hours and the strength of cylinders that were aged for 2 days and cured for 24 hours. Thus, it describes the effect of two days of aging time. Region “B” quantifies

the difference in compressive strength of cylinders aged for two days and cured for 24 or 48 hours. For Mixes #1 and #2, 38% of the gains between the batch not aged and cured for only 24 hours and the batch aged for two days and cured for two days were related to aging while 62% were related to heat curing. The higher alkalinity Mix #3 showed much different behavior with 95% of the strength gains being attributable to aging and only 5% attributable to heat curing.

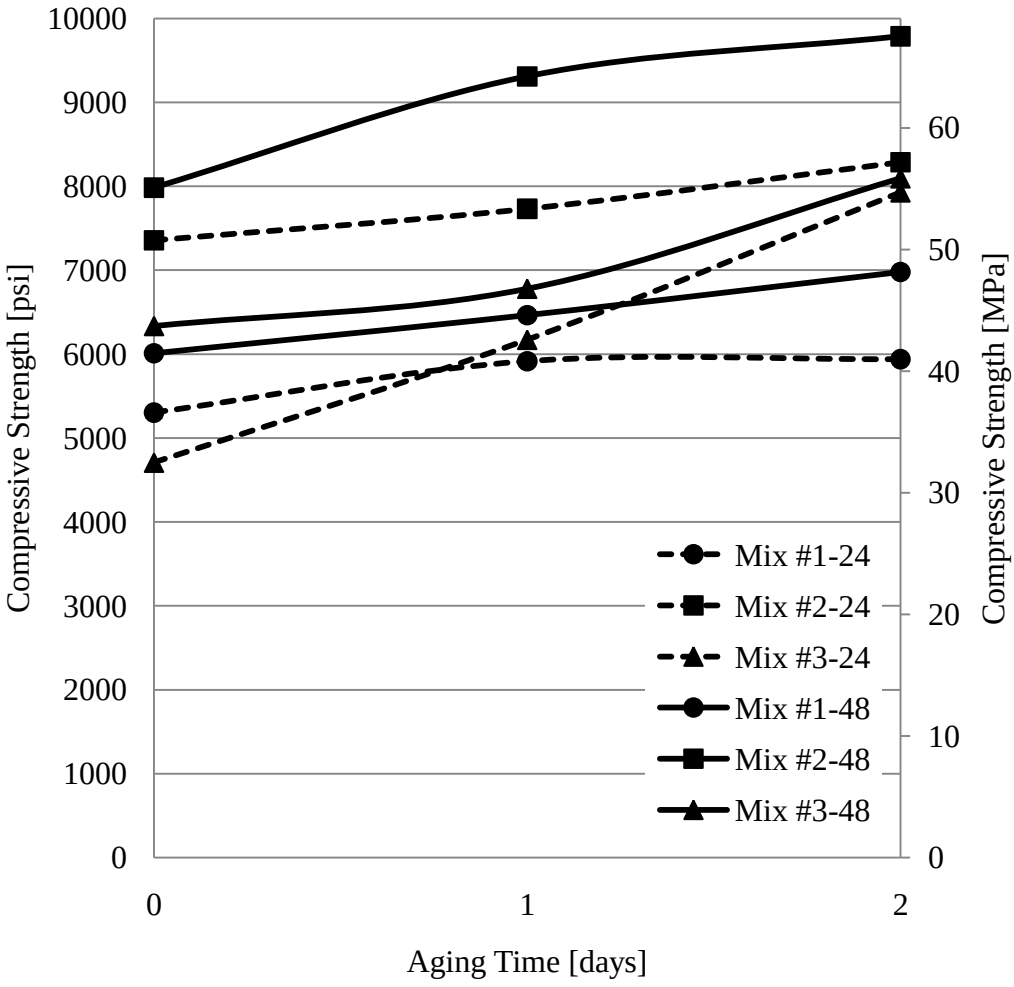

FIGURE 2-18: Compressive strength development with aging and curing time.

It would appear that heat is playing a role in two different reaction mechanisms. For instance, in the lower alkalinity concretes, the heat might help strength development by improving the dissolution processes by increasing the solubility of silica. In higher alkalinity systems the heat is probably not required to improve dissolution due to the greater quantity of available OH^- ions. This may be explained by the very small difference in strength between Mix #3 specimens aged for 2 days and cured for 24 hours versus those cured for 48 hours.

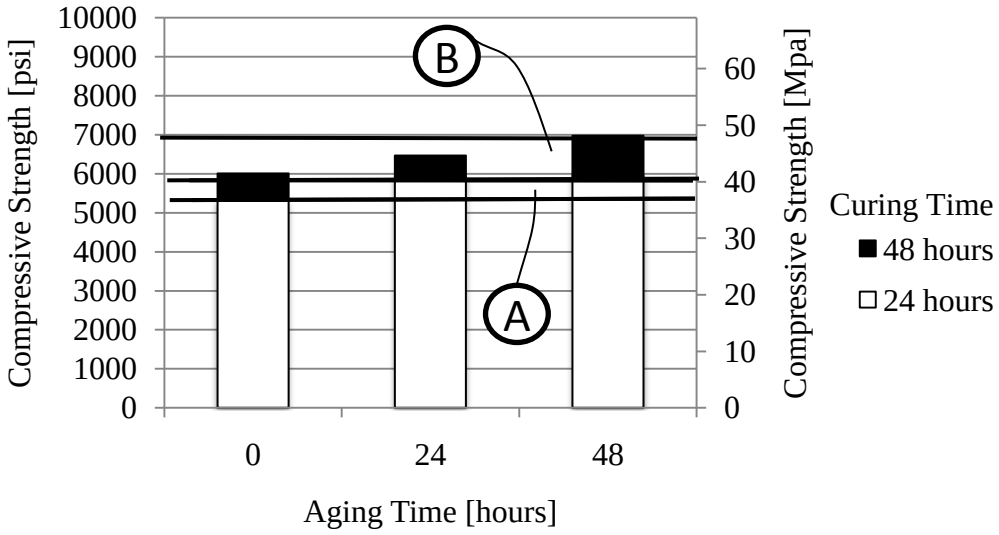

FIGURE 2-19: Compressive strength after 24 and 48 hours of curing for Mix #1.

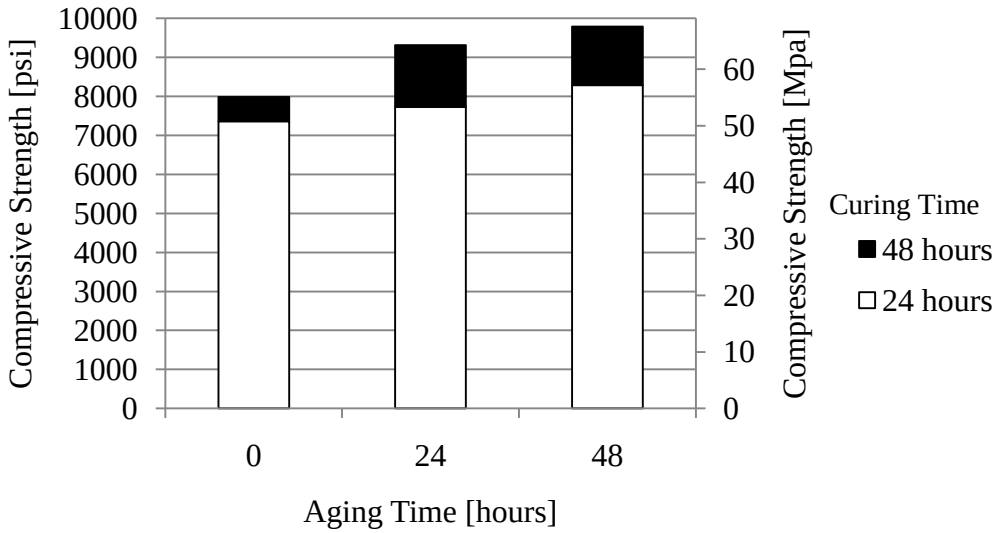

FIGURE 2-20: Compressive strength after 24 and 48 hours of curing for Mix #2.

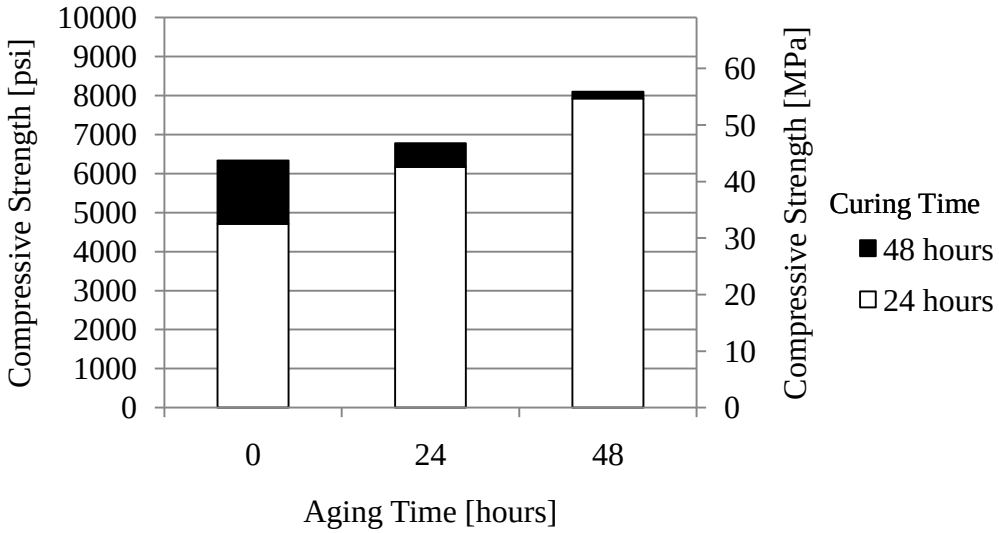

FIGURE 2-21: Compressive strength after 24 and 48 hours of curing for Mix #3.

2.8 Mechanical properties

2.8.1 Tensile strength

As with Portland cement concrete, the split cylinder tensile strength of the geopolymer cement concrete specimens was found to be proportional to the compressive strength. TABLE 2-13 shows that the tensile strength ranged from 7.1% to 10.6% of the compressive strength. Large numbers of combined results from Portland cement split cylinder tests have revealed an average tensile strength, $\bar{f}_{ct}$, of (MacGregor and Wight, 2005)

$$\bar{f}_{ct} = 6.4\sqrt{f_c'} \text{ [psi]} \quad (2\text{-}2)$$

$$\bar{f}_{ct} = 0.53\sqrt{f_c'} \text{ [MPa]} \quad (2\text{-}3)$$

$$\bar{f}_{ct} = X\sqrt{f_c'} \quad (2\text{-}4)$$

where:

$\bar{f}_{ct}$: concrete cylinder splitting stress

f_c': concrete cylinder compressive strength

FIGURE 2-22 shows a strong relationship between the tensile and compressive strength of GCC cylinders. A non-linear multiple regression analysis was used to establish the value of the parameter "*X*" in Equation (2-4) The value, *X*=0.616, creates the regression line shown in FIGURE 2-22 and matches the data with *R*=0.796 for compressive strength in MPa. For English customary units, the parameter is 7.4. These Equations are

$$\bar{f}_{ct} = 7.4\sqrt{f_c'} \text{ [psi]} \quad (2\text{-}5)$$

$$\bar{f}_{ct} = 0.616\sqrt{f_c'} \text{ [MPa]} \quad (2\text{-}6)$$

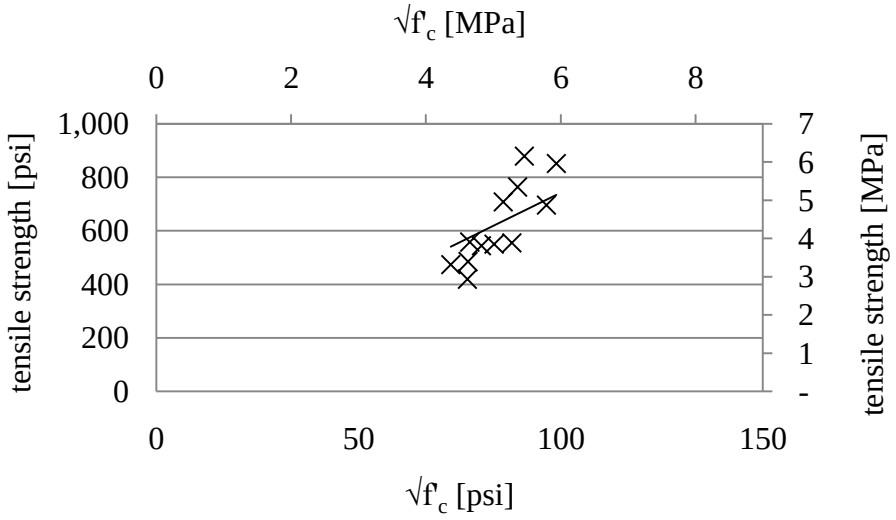

FIGURE 2-22: Relationship between splitting tensile and compressive strength of GCC cylinders

2.8.2 Modulus of elasticity

The modulus of elasticity of the concrete was measured using the procedure given in ASTM C469 "Standard Test Method for Static Modulus of Elasticity and Poissons's Ratio of Concrete in Compression" (ASTM, 2002a). The results are plotted in FIGURE 2-23 and show a clear trend towards increasing modulus with increased compressive strength. It is typical in concrete design to estimate the modulus of elasticity of concrete by relating it to compressive strength via the formula given via the equations.

$$E_c = w_c^{1.5} 33 \sqrt{f_c'} \text{ [psi]} \quad (2\text{-}7)$$

$$E_c = w_c^{1.5} 0.043 \sqrt{f_c'} \text{ [GPa]} \quad (2\text{-}8)$$

where:

w_c : unit weight of the concrete

The unit weight of the geopolymer cement concrete has been found to be 140 lb/ft^3. However, because all the concrete produced in this study had essentially the same

unit weight, there is no basis to use the unit weight as a predictor of GCC modulus of elasticity. More data would be required to make such correlations. The relationship between cylinder compressive strength and modulus of elasticity found for the materials produced in this study is given by

$$E_c = 41{,}193\sqrt{f_c'} \text{ [psi]} \quad (2\text{-}9)$$

$$E_c = 3{,}421\sqrt{f_c'} \text{ [GPa]} \quad (2\text{-}10)$$

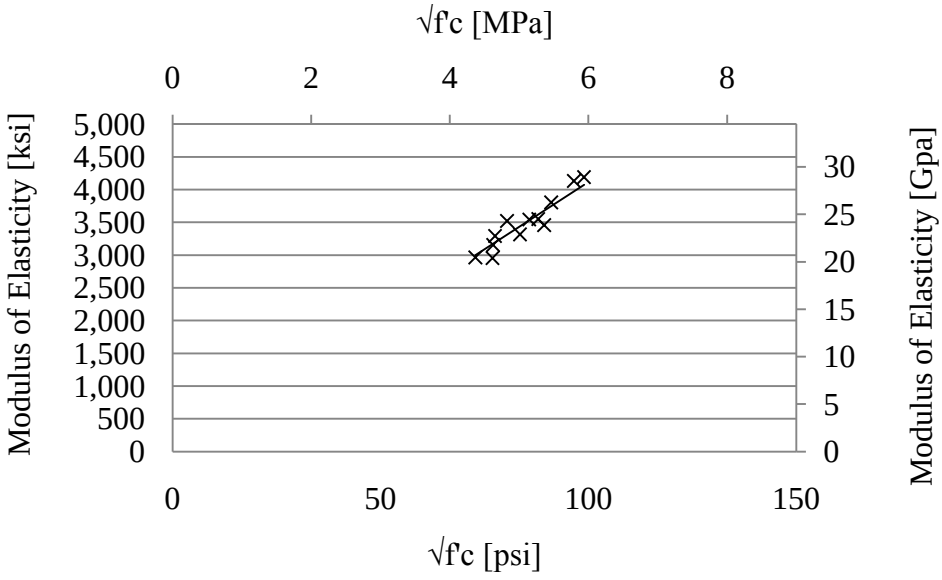

FIGURE 2-23: Compressive strength and Young's Modulus for Mix #1 and Mix #2.

2.9 Creep

The time-dependent deformation of concrete under sustained loads is referred to as creep. In Portland cement concrete, the paste fraction undergoes dimensional changes while the aggregates tend to restrain creep-related deformation. After concrete cures and enters service, a series of processes that result in volumetric changes occur, including free shrinkage strain ε_{sh}, basic creep ε_{bc}, drying creep ε_{dc}, and elastic strains ε_e. The total

strain measured in a concrete element is a combination of these constituent strains, as given by

$$\varepsilon_{total} = \varepsilon_{sh} + \varepsilon_{bc} + \varepsilon_{dc} + \varepsilon_{e} \quad (2\text{-}11)$$

The summation of these strains is the total measurable strain.

The ratio of creep strain, ε_{cr}, to elastic strain, ε_e, is known as the creep coefficient, C, as given by

$$C_t = \frac{\varepsilon_{cr}}{\varepsilon_e} \quad (2\text{-}12)$$

The creep coefficient changes over time as the strains attributable to creep processes become similar in magnitude to and greater than elastic strains. For design purposes, ACI Committee 209 provides the equation

$$C_t = \frac{t^{0.6}}{D+t^{0.6}} C_u \quad (2\text{-}13)$$

where:

t: time (days)
D: constant usually taken as 10 (days)
C_u. Ultimate creep

as a means of estimating the creep coefficient at a given time interval, *t* days, as a function of the ultimate creep, C_u. Ultimate creep for Portland cement concrete is known to range from 1.30 to 4.15, with an average value of 2.35 (Branson, 1976).

The measurement of creep in controlled laboratory settings is undertaken by preparing concrete cylinders, allowing them to cure for a specified period of time and then subjecting them to a stress that does not exceed the proportional limit for the material. The range typically used is less than 40% of the cylinder's compressive strength. In order to compare the results of tests completed using differing stress

intensities the factor, specific creep φ, is defined as the ratio between creep strain and applied stress σ. This relationship is given by

$$\varphi = \frac{\varepsilon_{cr}}{\sigma} \tag{2-14}$$

where:

φ: specific creep
ε_{cr}: creep strain
σ: applied stress

2.9.1 Creep measurement procedures

In order to study the creep behavior of the materials developed in this work, specimens were prepared from two batches of concrete, GCC-2 and PCC-1. The mix proportions for each of these batches are given in

TABLE 2-14. The PCC mix serves as a reference point to compare the results of the GCC batch. Both concretes were mixed in a mixer truck, placed in 6”X12” (152mmx305mm) cylinders and consolidated by rodding, as shown in

FIGURE 2-24. Gage studs were fixed along two opposite sides of the cylinder with an 8” (203mm) gage length, as shown in FIGURE 2-25.

After mixing and placing, the GCC materials were aged for two days at ambient conditions in the lab and then cured for two days in a dry, 167° F (75° C) oven. The PCC material was removed from the cylinder mold after 1 day and placed in a 100% humidity curing room until the time of the test. All specimens, GCC and PCC, were initially loaded at an age of 28 days with a common load of 35,000 lb (156 kN). This corresponds to a stress on the cylinder of 1,238 psi (8.5 MPa). Strain measurements were made with a

demountable mechanical strain gage at the intervals specified in ASTM C512 (ASTM, 2002b).

The cylinders were capped with a sulfur compound and loaded in pairs into the frame shown in FIGURE 2-26. The load was transmitted from the end plates to the cylinders through small cylinder slices of similar strength concrete, also visible in FIGURE 2-26. The loads were maintained on the specimens via heavy springs to prevent small dimensional changes in the concrete from creating large reductions in stress. The magnitude of the load was monitored with a load cell connected to a digital read-out. If the load was found to differ from 35,000 lb (156 kN) by more than 2%, it was adjusted with a hydraulic pump.

TABLE 2-14: Mix proportions for creep specimens lb/yd^3 (kg/m^3).

Material	Mix Designation	
	GCC-1	PCC-1
Portland Cement	0	386 (229)
Fly Ash	835 (495)	89 (53)
Water	275 (163)	173 (103)
NaOH	84 (50)	0
Silica Fume	63 (37)	0
Fine Aggregate	1,336 (793)	709 (421)
Coarse Aggregate	1,336 (793)	1,127 (669)

FIGURE 2-24: Consolidating creep specimens.

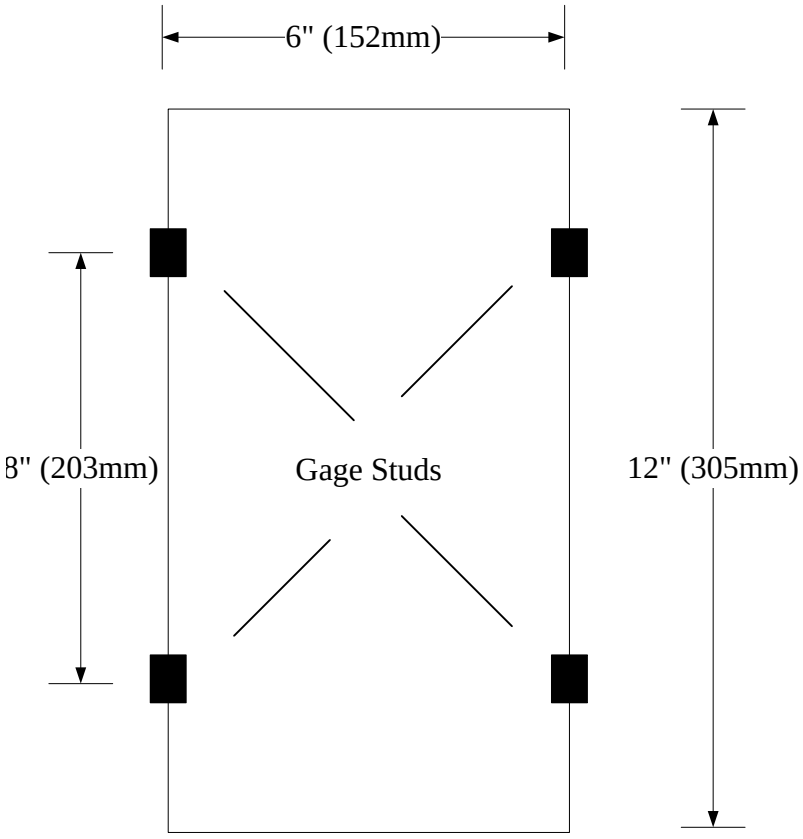

FIGURE 2-25: Gage stud layout for creep specimens.

FIGURE 2-26: Creep specimen loading apparatus.

2.9.2 Results

Strains were measured at two points along opposite sides of each specimen. These strains were then averaged across the two specimens that were prepared for each mix. The strains from the loaded specimens were reduced by the average strain found in the unloaded specimens in order to eliminate shrinkage strains from the measurements. Measurements taken immediately after the load was applied were used to compute the initial elastic modulus, E_i, shown in TABLE 2-15. Also given in this TABLE is the 28-day compressive strength of the concrete materials used in these specimens.

TABLE 2-15: Compressive strength and initial elastic modulus of creep specimens

Concrete	28-day f_c', psi (MPa)	E_i, psi (GPa)
GCC 2	9,500 (65.5)	2,842,271 (19.6)
PCC	11,200 (77.2)	5,170,922 (35.6)

The concrete materials produced the expected hyperbolic curve relating creep strains with time. FIGURE 2-27 and FIGURE 2-28 show the relationship of creep strain with total strain for the GCC and PCC specimens. Included in the total strain are elastic strains, shrinkage strains and creep strains. It is apparent that both the total strain and the creep strain were larger in magnitude for the PCC specimens despite their having a much higher initial elastic modulus.

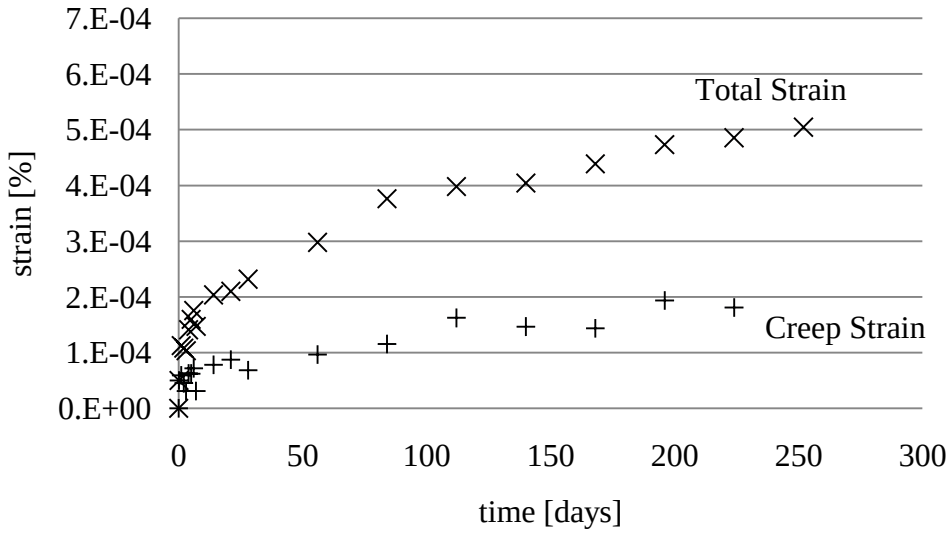

FIGURE 2-27: Relationship of creep strain with time for GCC specimens.

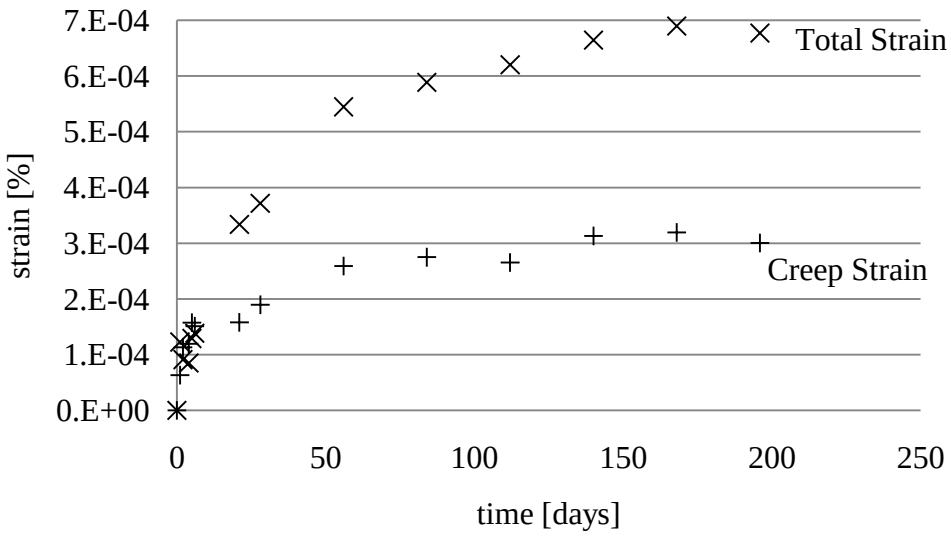

FIGURE 2-28: Relationship of creep strain with time for PCC specimens.

The ratio of elastic strains and creep strains is described by the creep coefficient. It approaches a limiting value of ultimate creep, C_u, which represents the maximum strain that would be found after a long period of time under loading. In FIGURE 2-29, Equation (2-13) is used to plot the creep coefficient using the upper and lower bound ultimate creep values for typical Portland cement concrete.

The PCC control specimens displayed typical behavior. The ultimate creep appears that it will lie within the range of expected values for Portland cement concretes. After 100 days of loading, the creep coefficient equaled 1.25, as compared to 0.09 as the lower end of creep behavior

FIGURE 2-29 shows that C_u for the GCC appears to be less than 1.0. Although data are only presented for 200 days of loading, creep does not seem to be increasing significantly for successive measurements beyond the 100th day. The range defined by C_u=1.30 and C_u=4.15 on the charts denote the typical range of ultimate strain for Portland cement concrete. The GCC is well outside the lower end of this range. This indicates

that the creep behavior of GCC is significantly improved over the expected behavior of PCC.

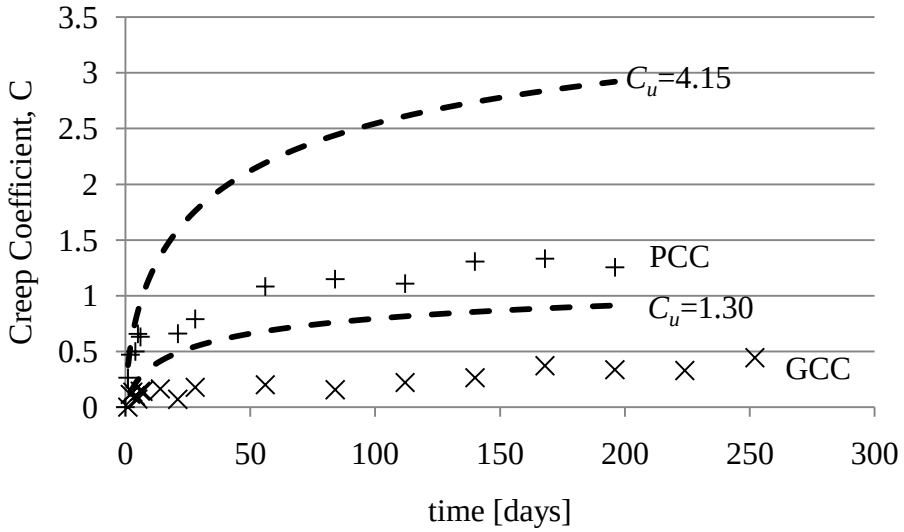

FIGURE 2-29: GCC and PCC creep compared to the range of ultimate creep values for Portland cement concrete.

2.10 Shrinkage

Removal of water from the concrete matrix causes shrinkage strains as the overall volume of the monolith is reduced. When the water is removed from fresh concrete, the resulting shrinkage is known as plastic shrinkage. The effects of plastic shrinkage are manifested in crack patterns that negatively impact the appearance and durability of concrete surfaces. In hardened concrete, shrinkage processes are a result of the continued removal of water from the pore system of the concrete either by self-desiccation in autogenous shrinkage, by chemical reaction in carbonation shrinkage or by evaporation (Mindess et al., 2003).

Predicting the magnitude of shrinkage is important to the design of concrete structures. If the designer can properly locate contraction joints and control restraint

against shrinkage, cracks can be eliminated or limited to acceptable locations. Passive or prestressing reinforcement is also a design requirement to restrain shrinkage in concrete structures, with minimum steel ratios given by ACI 318 (American Concrete Institute, 2008).

Shrinkage of concrete is a process that involves many variables for structures in service. These include the duration of wet curing, air content, aggregate characteristics and temperature, and relative humidity around the structure. ACI committee 209 provides guidelines for estimating shrinkage of concrete after periods of time. Prediction of the magnitude of the shrinkage is made with

$$(\varepsilon_{sh})_t = \frac{t^{\alpha}}{f+t^{\alpha}}(\varepsilon_{sh})_u \tag{2-15}$$

where:

$(\varepsilon_{sh})_t$: shrinkage strain at time, t $(\varepsilon_{sh})_u$=800x10^{-6} in/in (mm/mm) for PCC
α: power of t ~1.0
f: constant taken as 20-130 days
$(\varepsilon_{sh})_u$: ultimate shrinkage, 800x10^{-6} in/in [mm/mm]

Although shrinkage can cause serious durability and aesthetic problems in all types of concrete structures, it presents a special concern in prestressed concrete sections. As shrinkage strains increase in the concrete, the elongation of the prestressing steel tendons is reduced, causing a net reduction in the effective prestress. The magnitude of this reduction is related to the modulus of the steel as given by

$$\Delta f_{sh} = \varepsilon_{sh} E_{ps} \tag{2-16}$$

where:

Δf_{sh}: change in stress in the prestressing steel due to concrete shrinkage, psi or MPa
ε_{sh}: shrinkage strain

E_{ps}: modulus of elasticity for prestressing steel, psi or MPa

2.10.1 Measurement of shrinkage

In order to determine shrinkage experimentally, concrete is cured and aged under controlled environmental conditions that are set at temperature and humidity levels of interest. Generally, the environmental conditions used to establish baseline shrinkage magnitudes are 73°F (22.7°C) and 50% relative humidity. General procedures for conducting shrinkage measurements are given by ASTM 157 (ASTM, 2008b). 3”x3”x11.25” (76mmx76mmx286mm) concrete prisms are formed and outfitted with gage studs in each end. The length of the prism is measured after the concrete initially sets, again after the primary curing is completed and then at intervals through 64 weeks.

Three batches of concrete were prepared using the mixing proportions given in TABLE 2-16. Data were collected for the shrinkage behavior of three concrete mix types. PCC is a Portland cement concrete mix, GCC-2 represents a geopolymer cement concrete with virgin aggregates and GCC-R represents a geopolymer cement concrete with 45% of the virgin aggregates replaced by recycled aggregates. Four prisms were prepared from each concrete mix. In order to not confound the results with processes that are not related to drying shrinkage, the PCC specimens were handled in accords with ASTM 157 (ASTM, 2008b). The specimens were removed from the molds after 24 hours, placed in lime-saturated water for 1 hour and then an initial measurement was made. The specimens were stored in the lime water for a period of 28 days, after which readings were made at 4, 7, 14, 28 and 56 days.

GCC-2 and GCC-R were handled slightly differently from the ASTM procedures since these guidelines do not have provision for geopolymer cement concretes. The specimens were consolidated in the forms by rodding, covered with plastic and allowed to age for two days. Following the aging period, they were cured at 167°F (75°C) for 48 hours. During preparation of GCC-R, there were problems with the heating apparatus and the temperature in the curing chamber did not reach the target temperature during the initial 24 hours of the curing period. Therefore, it was permitted to cure for additional time to allow at least 48 hours at the target temperature, 167°F (75°C).

Following removal from the forms after curing at elevated temperature, the GCC specimens were measured immediately with a length comparator and then stored for the duration of the test in an environmental chamber set at 73°F (22.7°C) and 50% relative humidity. Length measurements were made at 4, 7, 14, 28, and 56 days.

TABLE 2-16: Mixing proportions for shrinkage specimens lb/yd^3 (kg/m^3).

Component	Mix Designation		
	PCC-1	GCC-2	GCC-R
Portland Cement	386 (229)	0	0
Fly Ash	89 (53)	835 (495)	815 (483)
Water	173 (103)	275 (163)	268 (159)
NaOH	0	84 (49.5)	81 (48)
Silica Fume	0	63 (37.1)	61 (36)
Fine Aggregate	709 (421)	1,336 (793)	1304 (773)
Coarse Aggregate	1127 (669)	1,336 (793)	718 (426)
Recycled Coarse Aggregate			587 (348)

2.10.2 Shrinkage test results

Data was available for 224 days of post-curing shrinkage for PCC and GCC-2. However, data only extend 56 days for the GCC-R batch. TABLE 2-17 provides the average strain for each group of four prisms. FIGURE 2-30 through 2-32 illustrate the increase in shrinkage strain with time. The largest shrinkage strains were found in the PCC mix. Shrinkage increased rapidly between day 0 and day 28. The strains appear to be approaching 700 X 10^{-6} %, which is within the typical range for Portland cement concrete. Moist-cured Portland cement concrete has an average ultimate strain of 800 X 10^{-6} %.

The GCC-2 concrete indicates a more gradual approach to an upper value of 220X10^{-6}% at 112 days. Some data from cylinders created for creep testing was supplemented in FIGURE 2-31 since the data from the shrinkage tests 4, day 14 and day 28 were strong outliers. The cylinders were stored in the same environmental chamber and were instrumented for precision measurements over a gage length of 8" (203 mm). The same shrinkage trends are seen in the cylinders as in the shrinkage prisms and the proximity of the data points along the curve in FIGURE 2-31 verify the behavior in place of the missing measurements.

TABLE 2-17: Shrinkage test results.

Batch	Microstrain at Day							
	0	4	7	14	28	56	112	224
PCC-1	-40	180	230	430	480	510	630	760
GCC-2	0	-	60	-	-	120	240	220
GCC-R	0	260	130	-	260	270	-	-

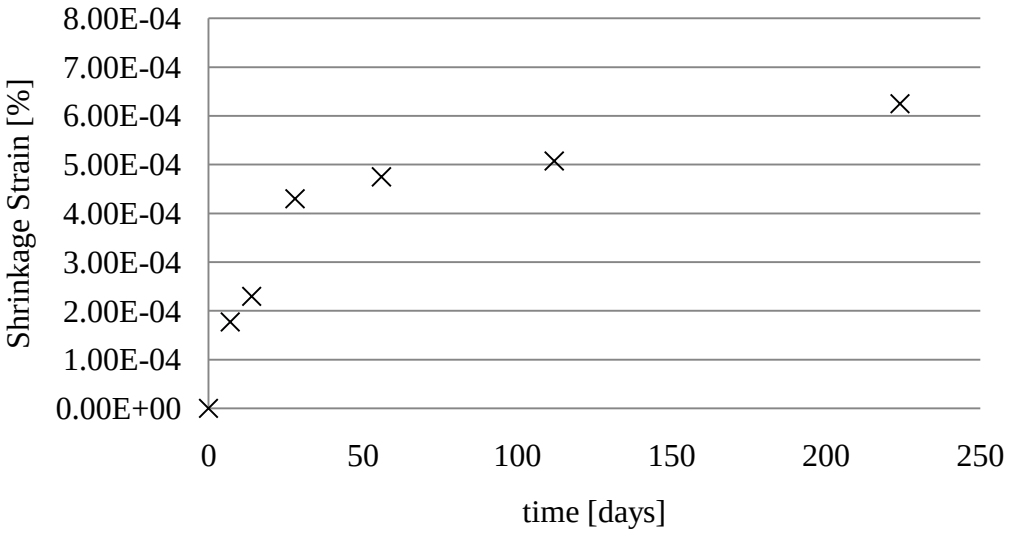

FIGURE 2-30: PCC-1 shrinkage strain versus time.

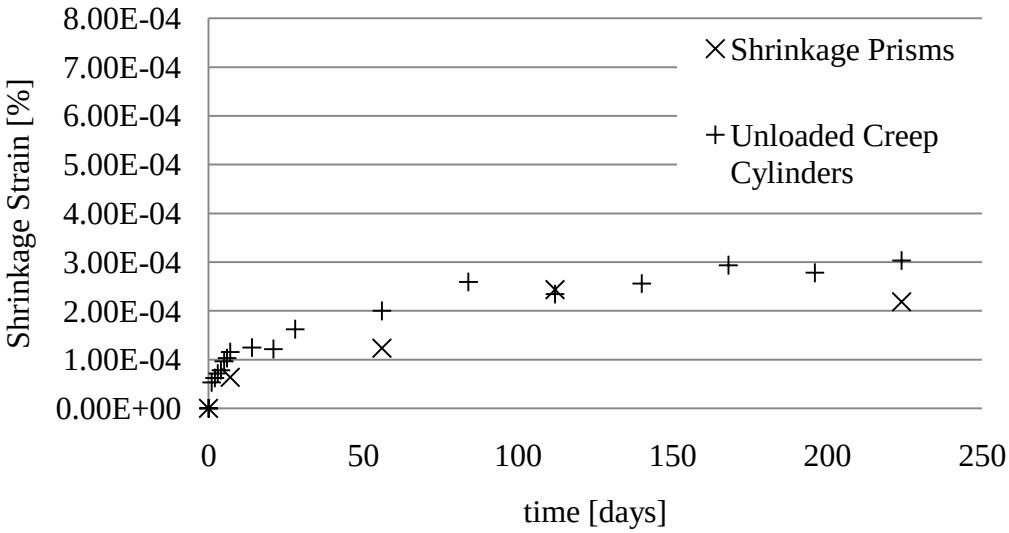

FIGURE 2-31: GCC-2 shrinkage strain versus time.

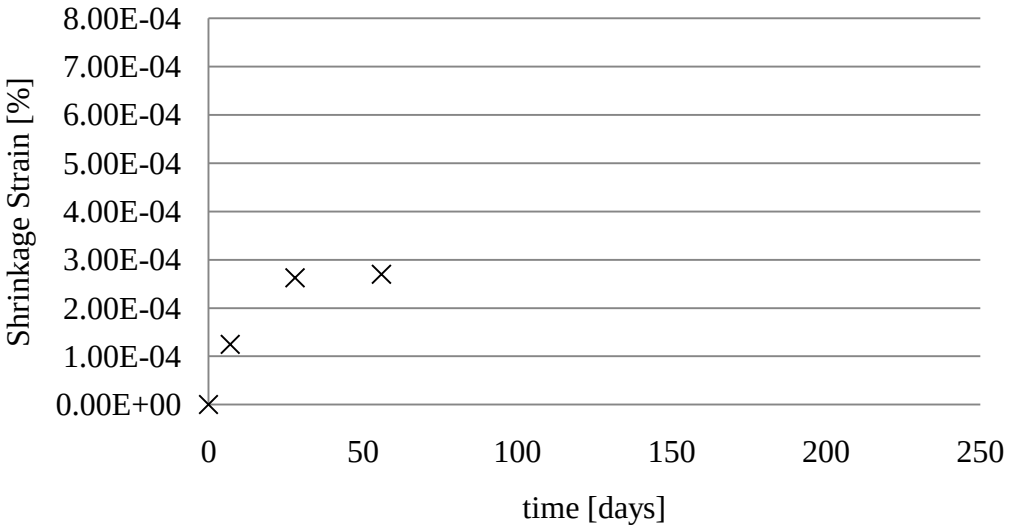

FIGURE 2-32: GCC-R shrinkage strain versus time.

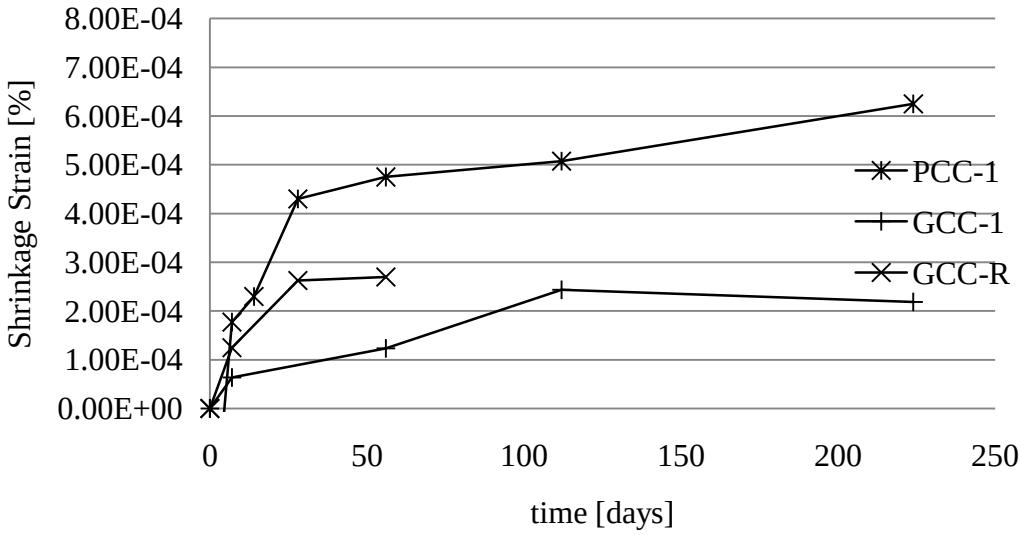

FIGURE 2-33: Comparison of shrinkage in PCC-1, GCC-2 and GCC-R specimens.

GCC-R approaches an upper value of $270X10^{-6}$ at 56 days. Although the test duration was shorter than for GCC-2, it appears that the ultimate shrinkage will be higher for the concrete containing recycled aggregates. This indicates that the recycled

aggregates have made some impact on the shrinkage characteristics of the concrete. Without mineralogical or microstructural data to evaluate, the exact cause of the additional shrinkage is not apparent. However, it may be related to the proportion of concrete mortar in the matrix which could have undergone swelling and shrinkage as a result of remixing in the geopolymer. Also, the presence of calcium from the old cement particles in the recycled aggregate could have also lead to the formation of C-S-H phases that coexist with the geopolymer. The C-S-H could make the concrete more prone to autogenous shrinkage.

2.10.3 Analysis of gcc-2 results

In order to use Equation (2-15) to estimate shrinkage in concrete, the terms α and f must be determined. As Equation (2-15) is simply a hyperbolic equation, reducing α below values of 1.0 will tend to steepen the ascending branch of the curve. Values of f affect how quickly the curve approaches the asymptotic value, $(\varepsilon_{sh})_u$. Using a multi-parameter curve fitting tool in MathCAD, values for α and f were found to describe the behavior of the GCC-2 materials. In the model $(\varepsilon_{sh})_u$ was taken to be 300 X 10^{-6}. With values of α=0.8 and f=0.9, the curve fits the data with R=0.952. A plot showing this curve is given in FIGURE 2-34.

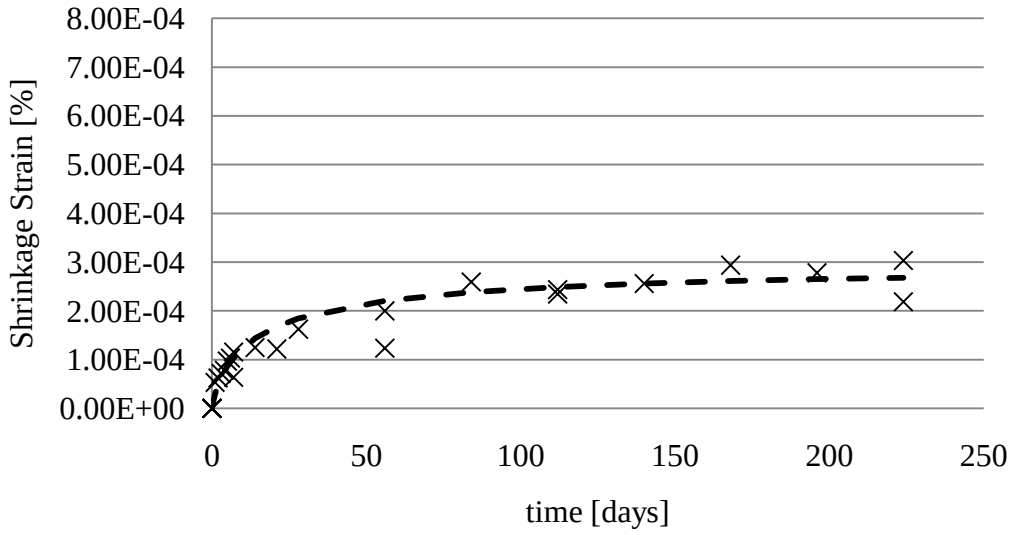

FIGURE 2-34: Prediction of shrinkage using α=0.8 and f=0.9.

2.11 Discussion of results and conclusions

Both geopolymer cement concretes tested for shrinkage resulted in lower strains at each time increment than Portland cement concrete. Strains in the PCC batch were more than 200% of the strains found in both geopolymer materials. Although the duration of the tests are not long enough to provide a conclusive magnitude for the ultimate shrinkage strain $(\varepsilon_{sh})_u$ the data do appear to approach an asymptote. For PCC the shrinkage strains appear to approach 700 X 10^{-6} in/in (mm/mm), which is typical for moist cured Portland cement materials. For the GCC-2 batch, the limit appears that it will be in the range of 300 X 10^{-6} in/in (mm/mm). Data for GCC-R do not extend far enough to extrapolate their upper limit. Equation (2-15) is effective at modeling shrinkage in geopolymer cement concrete with virgin aggregates. For the materials tested, α=0.8 and f=0.9.

It is important to note that the test procedure is only set-up to measure shrinkage in the GCC that occurred after high temperature curing. However, it will be important to understand and predict any volume changes that occur in the GCC as it undergoes the aging process and the high temperature curing process. These changes could be attributable to both the action of water evaporation from pore spaces in the GCC as well as to the formation of polymeric bonds during the hardening phase. A technique to measure these strains would need to account for the thermal expansion that occurs during elevated temperature curing.

CHAPTER 3: RECYCLED AGGREGATES IN GEOPOLYMER CEMENT CONCRETE

The sustainability benefits of geopolymer cement concretes (GCC) are related to its use of the waste material, fly ash. By incorporating the fly ash into the concrete, the dual environmental challenges of landfilling the ash and reducing the amount of Portland cement-related greenhouse gas emissions are addressed. One means of improving the sustainability farther is by the incorporation of recycled material for aggregate. Once mix designs were developed using virgin, granite aggregates as described in 0, portions of the aggregate were replaced by crushed demolition rubble. This chapter describes the process of collecting and evaluating the rubble as well as developing mix designs that incorporate it in the GCC.

3.1 Background on recycled concrete aggregate use

Demolition rubble comprises 8% of the construction and demolition waste produced in Mecklenburg County, North Carolina. In 2005, this equaled more than 31,000 tons (Mecklenburg County Land Use and Environmental Services Agency, 2006). When it is diverted from the landfill, its current uses are largely restricted to low-grade, non-structural applications such as road sub-base and erosion control. While researchers have used RCA to manufacture structural strength concretes, there have been problems associated with the high water absorption capacity and interrupted interfacial transition zone of reclaimed aggregates (Topçu and Sengel, 2004; Tu et al., 2006). These challenges might not have the same impacts in geopolymer concretes due to the absence

of hydration processes and the ability of geopolymer to bond with Portland cement mortar.

RCA is used in concrete in order to reduce the natural resource demands of concrete production as well as to create an outlet for a large waste stream. The aggregates are produced by crushing pieces of concrete that are generated from demolition projects. This sort of demolition work is often aligned with large-scale material disposal undertakings. Examples include clean-up in the aftermath of earthquakes and other natural disasters as well as wrecking large facilities like the Stapleton Airport in Denver, Colorado. Elias-Ozkan (2001) suggests that municipalities can control the quantities of concrete rubble destined for landfills or unsuitable dumping grounds by more tightly controlling the issuance of demolition permits. The opportunities for reclaiming material for aggregate in this manner could include production of aggregates on-site in the case of demolition-rebuild projects (Elias-Ozkan, 2001). Doing so would reduce the energy required for transporting construction materials to the site and would control the source content.

The crushed pieces may be regraded in order to produce material suitable for use in concrete. However, there are other quality issues related to using a material of such variable consistency. Oikonomou (2005) surveyed the current state of RCA knowledge and determined that industrial and municipal requirements for greater use include a control system for collection and sorting of demolition waste, greater public support, more technical studies and development of specifications. While there are preliminary documents published by RILEM and BRE, Oikonomou categorizes the information required for the safe and sustainable use of RCA as:

1) Historical data on the make-up of antiquated concretes
2) Physical characteristics- presence of contaminants, water absorption, specific gravity
3) Mechanical characteristics- abrasion, degradation
4) Environmental characteristics- leaching potential

Although the original, virgin aggregates might be visible, between 25 and 60% of volume occupied by a single RCA particle is the mortar paste that remains adhered (Tu et al., 2006). The presence of this paste affects the performance and characteristics of the aggregate in several ways. The absorption capacity of recycled aggregates tends to be higher and can require larger amounts of water to achieve adequate workability (Topçu and Sengel, 2004). Hydration might also be delayed as a result of the absorption capacity. The workability of the mix is also affected by the greater angularity of RCA.

Tam et al. (2007) conducted research whereby the cement mortar was removed from the aggregate particles by treating them with acidic solutions. The acid attacks the CaO in the mortar and was found to be effective at reducing some of the negative physical characteristics of the RCA surrounding absorption capacity and affected surface at the interfacial zone. The process was determined to be cost effective when the benefits of waste diversion from the landfill were included (Tam et al., 2007).

The impact of RCA use on compressive strength has been well researched. In general, researchers have found that compressive strength decreases as the ratio of recycled aggregate to virgin aggregate increases. Tupcu and Sengel (2004) created concrete specimens with target strengths of 2300 psi and 2900 psi (15.9 MPa -20.0 MPa) and then replaced virgin aggregates with RCA at the rate of 30, 50, 70 and 100%. The

specimens were subjected to compressive testing, freeze-thaw cycling and flexural testing. It was found that the compressive strength decreased at a rate relative to the addition of RCA. However, the freeze-thaw cycling had little effect on the flexural or compressive strength of the specimens (Topçu and Sengel, 2004).

Tu et al explored the use of RCA in high performance concrete (HPC). The research group tested concretes in strength ranges suitable for structural applications (3,000-6,000 psi) (20.7-41.4 MPa) that had been created with either recycled coarse or recycled coarse and fine aggregates. It was determined that, while a strength reduction of 20-30% could be expected due to aggregate replacement, the durability of the concrete matrix and its ability to protect steel from chloride intrusion was suitable for reinforced, structural applications (Tu et al., 2006).

The challenges to maintaining stringent mechanical performance standards while using RCA in concrete mixes have been overcome by adapting either the batching process or reducing the proportion of recycled material. Tam et al. (2005) have adapted the mixing process into two stages- the first to coat the aggregate in a rich cement slurry, and the second to complete the addition of mixing water. The author found that this technique filled microcracks along the interfacial transition zone and also allowed fresh paste to reach the surface of the mineral aggregate. The problem of high water absorption capacity in RCA has been addressed by simple techniques such as presoaking aggregates prior to batching (American Concrete Pavement Association, 2009).

State departments of transportation as well as national level agencies, such as the National Cooperative Highway Research Program (NCHRP), National Ready Mix Concrete Association (NRMCA), the American Concrete Pavement Association (ACPA)

and the Federal Highway Administration (FHWA) have produced guidance on the implementation of projects that permit or encourage recycled concrete aggregates in new PCC applications.

Control of concrete quality when RCA is used is achieved via several strategies that are given in state department of transportation materials specifications or in the guidance published by the previously listed agencies. These strategies include the following major themes:

1) Limitation to the quantity of RCA in the concrete
2) Preparation and handling guidelines
3) Limits to the source of acceptable materials
4) Restrictions on the type of elements permitted to contain RCA
5) Characterization requirements

TABLE 3-1 provides a sampling of the specifications and guidelines given by various groups. Perhaps the most conservative risk reduction technique for specifying RCA concrete products is to limit the type or allowable proportion of recycled material in the mix design. For instance, Texas Department of Transportation (TXDOT) permits a maximum of 20% recycled fine aggregate in certain non-structural concrete elements (Texas Department of Transportation, 2004). A strategy introduced in Europe encourages the segregation of incoming material by source or quality so as to maintain stockpiles of rubble having known origins and quality. The Michigan Department of Transportation (MDOT) specification only permits RCA that was collected from MDOT demolition projects. In this way, the source material is known to have met Michigan quality standards when it was originally created (Michigan Department of Transportation,

2003). The NRMCA has proposed similar recommendations for returned concrete aggregates- suggesting that they be divided by the grade of concrete in the truck (Obla et al., 2007).

TABLE 3-1: Various guidelines for use of RCA.

Topic	MDOT	TXDOT	FHWA	NRMCA	ACPA
Document Type	*Specification*	*Specification*	*Guideline*	*Guideline*	*Guideline*
Limitation of the quantity of RCA in the concrete	None given	Recycled fine aggregate limited to 20%.	Recycled fine aggregate limited to 10-20%	10% for general source RCA, 30% for returned material > than 21 MPa	10%-20% limit on recycled fine aggregate
Preparation and handling guidelines	Must maintain separate stockpiles to avoid non MDOT source material	None given	Sprinkle stockpiles to keep aggregates saturated; store separately from other materials	Separate incoming material according to quality; maintain SSD conditions with sprinklers	None given
Limits to the source of acceptable materials	MDOT concrete	None given	None proposed	Higher-quality returned material	None given
Restrictions on the type of elements permitted to contain RCA	Curb and gutter, valley gutter, sidewalks, barriers, driveways, temporary pavements, ramps with commercial ADT 250, shoulders	Inlets, manholes, gutters, curbs, retards, sidewalks, driveways, backup walls, anchors, riprap, small signs, pavements (all of these applications require <21 MPa concrete)	Recommendations only relate to pavements	Structural elements should contain less than 10%, non-structural applications up to 30%	Recommendations only relate to pavements
Characterization requirements	Project by project freeze-thaw characterization	None given	Deleterious materials such as chloride, sulfate	Weekly verification of absorption and specific gravity	Perform freeze-thaw evaluation on materials exhibiting D-cracking or containing fly ash

(American Concrete Pavement Association, 2009; Federal Highway Administration, 2008; Michigan Department of Transportation, 2003; Obla et al., 2007; Texas Department of Transportation, 2004)

Other waste stream constituents have also been researched as virgin aggregate replacements. Kou et al. studied the possibility of replacing fine aggregates with small particles of discarded PVC pipe. By mixing the material into a concrete at river-sand replacement rates of 5, 15, 30 and 45%, it was found that the PVC granules reduced the compressive strength, modulus of rupture, elastic modulus and workability. However, quantity of charge passed by the concrete was reduced, indicating that PVC could improve the durability of concrete. It was also found that drying shrinkage was reduced by adding PVC pieces. The author suggests PVC for use in non-structural applications at a sand replacement rate of 15% (Kou et al., 2009).

3.2 Collecting recycled concrete aggregates for gcc use

UNC Charlotte researchers observed the demolition of an elementary school facility in order to study the physical processes included in the tear-down as well as the decision making process for the disposal or the recycling methods applied to the demolished materials. The construction of the school was typical for a wide range of commercial and institutional buildings at the time. Therefore, the information presented here regarding the demolition process should be relevant to many of the buildings in the local inventory. Walls were reinforced and unreinforced masonry, the roof was a combination of prestressed concrete double-tees and steel framing, and the floor system was a concrete slab-on-grade. The demolition process was found to be very orderly and included many techniques that simplified the separation of materials such that contamination of the rubble destined for the crusher was minimized. General steps followed in the demolition (in sequential order) were:

1) Removal of hazardous materials such as asbestos

2) Removal of valuable metals such as copper and non-critical steel structures (such as awnings)
3) Demolition of non-masonry partition walls, drop ceilings, and fenestration
4) Collection and disposal of materials listed in #3
5) Demolition and removal of roof framing, decking and covering
6) Demolition and removal of masonry partition walls
7) Demolition and removal of the concrete slab

The demolition strategy used in the case of the elementary school is referred to as "top-down." The non-rubble generating materials such as gypsum wall board, wood finishings, fixtures, and the like are removed first. Secondly, the masonry materials that constitute the walls are crushed and removed separately. Third, the concrete floor slab is crushed and hauled off-site. While the top-down process may not be used for smaller projects in which separation of wastes is not economical, it is a practical technique for mid to large scale demolition work and also lends itself to source separation. The concrete slab was used as a sorting pad for demolished materials before they were hauled to the crusher, landfill, steel recycling facility or other location. In addition to providing a surface for the loading equipment to drive on, the concrete slab could be cleared between phases to prevent the introduction of foreign materials such as cellulose, plastics and metals into the rubble for RA. UNC Charlotte researchers found that segregating the rubble materials before they were crushed helped improve the quality and predictability of the RA.

Prior to the commencement of demolition, 2.5" (64mm) diameter core specimens were removed from the section of slab that would be crushed to produce aggregate. A portable coring drill was used to obtain the samples. A total of seven core samples were

removed from three locations in the slab. Of these, due to the relatively shallow thickness of the slab-on-grade, five core samples were found to be suitable for compression testing. The ends of the cylinders were trimmed with a wet diamond saw and the specimens were tested to failure in a universal testing machine. Due to the location of the reinforcing mesh and the slab thickness, the length to diameter ratios of the trimmed cylinders were typically less than two. The compressive strength was discounted by interpolating between the values given in TABLE 3-2, which are provided in ASTM C42 (ASTM, 2004a). The results of these compression tests are given in

TABLE 3-3. The average adjusted compressive strength was found to be 6,800 psi (47 MPa). This indicates that the aggregates should be suitable for concrete products in the range of 5,000-7,000 psi (34-48 MPa).

In addition to collecting compressive strength information from core specimens, Schmidt Hammer readings were taken from the slab in proximity to the location of the core specimens. The procedure is outlined in ASTM C805 (ASTM, 2008a). No clear correlation was found between the rebound hardness measured in situ and the compressive strength of the core specimens determined in the lab.

TABLE 3-2: Strength reduction factors for specimen aspect ratios less than 2.0.

Length to Diameter Ratio	Strength Reduction Factor
1.75	0.98
1.50	0.96
1.25	0.93
1.00	0.87

TABLE 3-3: Compressive strength of cores removed from the slab.

Specimen	L/D	Reduction Factor	f_c', psi (MPa)	Adjusted f_c' [MPa]
1	1.1	0.90	7,411 (51.1)	6,672 (46.0)
2	1.3	0.94	6,396 (44.1)	6,034 (41.6)
3	1.2	0.92	8,528 (58.8)	7,817 (53.9)
4	1.2	0.93	7,934 (54.7)	7,368 (50.8)
5	2.0	1.00	6,469 (44.6)	6,454 (44.5)

Concrete slab-on-grade materials from the demolition case study were separated on-site, transported, and then crushed at the demolition contractor's aggregate production facility. Once crushed, these aggregates were taken to UNC Charlotte for study. The crushed aggregate was characterized in terms of gradation, bulk density and absorption capacity. The sieve analysis is presented in TABLE 3-4.

TABLE 3-4: Gradation of recycled aggregates produced from Idlewild Elementary School demolition rubble.

Sieve Opening, in (mm)	% Finer
0.75" (19)	100
0.50" (13)	100
0.375" (9.5)	85.0
0.187" (4.75)	14.0
0.0935" (2.36)	3.0
Pan	0.0

The bulk density of the recycled concrete aggregates was found to be 80.0 lb/ft^3 (1,281 kg/m^3), which is lower than typical granite aggregates used in the region. The

absorption rate of the recycled aggregate was found to be 7.6%, which is considerably higher than locally available granite aggregate.

3.3 Incorporation of recycled aggregate in GCC

The materials collected from the demolition project described in the previous section were incorporated at various rates into the GCC-1 mix devised in 0 and using the same procedures presented there. Concrete cylinders were prepared from the recycled aggregate mixes and were tested after 7 and 28 days. The compressive strength developed after 28 days as well as the ease of mixing was used to select a mix design to employ in the creation of mild steel reinforced and prestressed concrete beam specimens.

3.3.1 Production process

Since it is known that recycled aggregates have very high absorption rates, all aggregates were prepared by soaking them overnight in water. Prior to weighing the aggregates, they were towel dried on their surface to bring them to saturated surface dry (SSD) conditions. The weight quantity of the recycled aggregates was adjusted because of the lower bulk density relative to virgin aggregates. This was done to maintain a consistent volume between batches. The mixing proportions are shown in TABLE 3-5.

3.3.2 Compressive strength of recycled aggregate mixes

Two sets of cylinders were made using the mix designs given in TABLE 3-5. Thus, two batches representing each virgin aggregate replacement ratio was mixed two times. The cylinders were aged for two days and then cured at 167°F (75°C) for two days. The cylinders were tested in compression using ASTM C39 procedures at cylinder ages of 7 days and 28 days (ASTM, 2005). The results of the compression test are

provided in TABLE 3-6. The strength ranged from 4,997 psi (34.5 MPa) to 7,290 psi (50.3 MPa) at 7 days. 28 day cylinder strengths ranged from 5,310 psi (36.6 MPa) to 8,359 psi (57.6 MPa). All mix designs showed an increase in compressive strength between the 7th and 28th day.

TABLE 3-5: Mixing proportions for GCC containing recycled aggregate, lb/yd^3 (kg/m^3).

Component	Virgin Aggregate Replacement Ratio						
	100%	80%	50%	40%	30%	20%	10%
Fly Ash	815 (484)	815 (484)	815 (484)	815 (484)	815 (484)	815 (484)	815 (484)
Water	268 (160)	268 (160)	268 (160)	268 (160)	268 (160)	268 (160)	268 (160)
NaOH	82 (48)	82 (48)	82 (48)	82 (48)	82 (48)	82 (48)	82 (48)
Silica Fume	61 (36)	61 (36)	61 (36)	61 (36)	61 (36)	61 (36)	61 (36)
Fine Aggregate	1304 (774)	1304 (774)	1304 (774)	1304 (774)	1304 (774)	1304 (774)	1304 (774)
Coarse Aggregate	0 (0)	261 (155)	652 (387)	783 (464)	913 (542)	1044 (619)	1174 (697)
Recycled Coarse Aggregate	1305 (774)	1044 (619)	652 (387)	522 (310)	391 (232)	261 (155)	131 (77)

TABLE 3-6: Compressive strength results for GCC mixes containing recycled aggregate, psi (MPa).

	Virgin Aggregate Replacement Ratio						
	100%	80%	50%	40%	30%	20%	10%
Batch 1, 7-Day	5,490 (37.9)	4,997 (34.5)	6,388 (44)	6,964 (48)	5,218 (36)	4,607 (31.8)	6,771 (46.7)
Batch 1, 28-Day	6,336 (43.7)	6,220 (42.9)	7,505 (51.7)	8,127 (56)	5,310 (36.6)	6,111 (42.1)	7,570 (52.2)
Batch 2, 7-Day	6,715 (46.3)	6,157 (42.5)	7,290 (50.3)	6,694 (46.2)	6,657 (45.9)	6,517 (44.9)	7,163 (49.4)
Barch 2, 28-Day	7,209 (49.7)	6,677 (46)	8,359 (57.6)	7,310 (50.4)	7,318 (50.5)	7,324 (50.5)	7,938 (54.7)

As is apparent in FIGURES 3-1 and 3-2 compressive strength declined as the proportion of virgin aggregates replaced increased from 10 to 30%. However, in both batches, there was a spike in compressive strength with the addition of 40-50% recycled aggregates. Following the peak, compressive strength tended to decline with each increase in recycled aggregate content until the virgin aggregates were fully replaced.

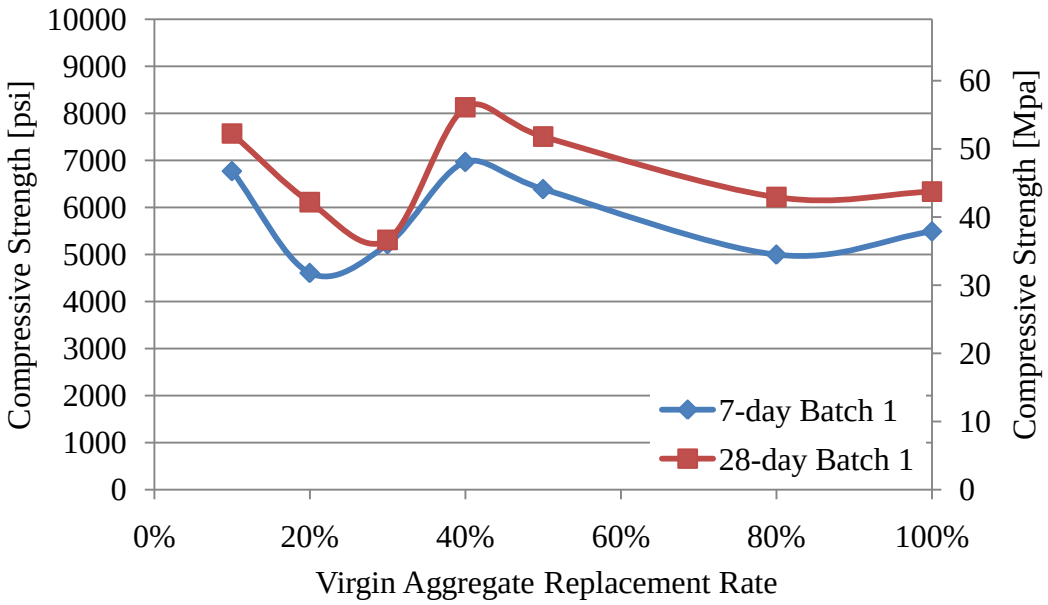

FIGURE 3-1: Batch 1 compressive strength at 7 and 28 days.

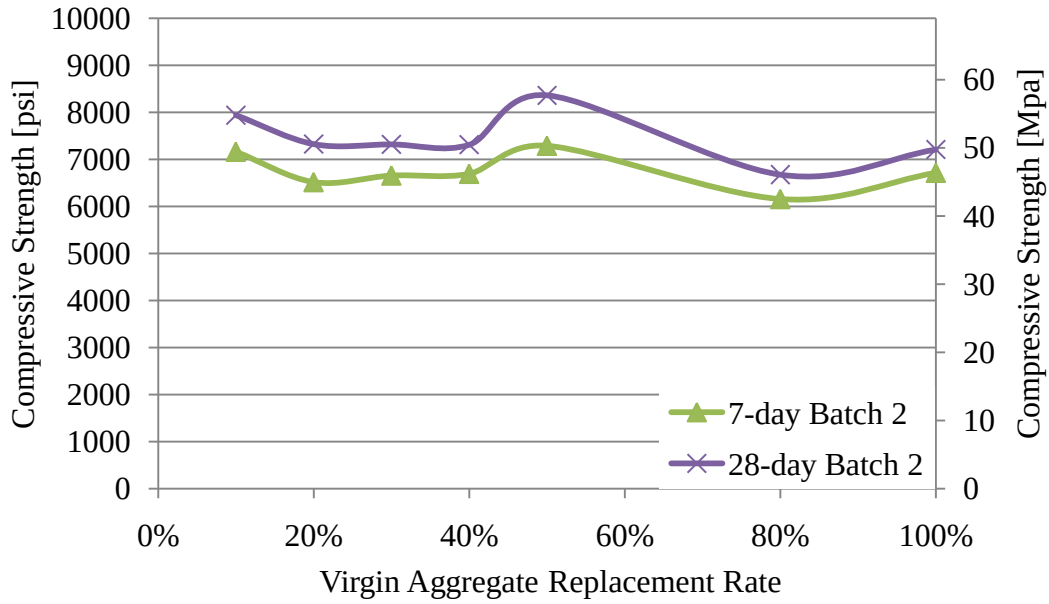

FIGURE 3-2: Batch 2 compressive strength at 7 and 28 days.

3.4 Discussion of results

The results from the two sets of GCC mixed with recycled aggregates indicate that it is possible to develop compressive strength suitable for structural applications while using significant proportions of recycled aggregates. All replacement ratios from 10% through 100% provided concrete with greater than 6,000 psi (41.4 MPa) at 28 days. For strength development purposes, the optimal quantity of recycled aggregate to replace, as determined by this study, is between 40 and 50% by weight.

The spike in compressive strength when 40-50% of the virgin aggregate is replaced by recycled aggregate could result from numerous factors. Many of these would not be differentiable without chemical or microanalysis of the mortar structure to determine what type of binding materials have formed. However, one probable reaction that is occurring is related to the calcium brought to the mix by the old cement in the recycled aggregate. The presence of calcium is known to accelerate the hardening of geopolymer

matrices. Although not quantified, stiffening of the fresh material was experienced by the research team during sample preparation. The extent of the reduced workability was directly related to the proportion of recycled aggregate contained in the mix. Researchers have detected the formation of C-S-H gels in geopolymer matrices formed in the presence of calcium. In some cases, the calcium was found to improve the mechanical strength characteristics of the hardened product. This was characterized by finer pore structures, lower setting temperatures and improved compressive strength (Guo et al., 2009; Temuujin et al., 2009).

In systems with moderate alkalinity (<7.5 M), C-S-H gel was detected as forming in conjunction with the geopolymer gels (Yip et al., 2005). The improvements in compressive strength were thought to have resulted from the C-S-H gel bridging geopolymer gel phases with unreacted particles. The formation is much reduced in systems having alkalinity greater than 7.5M (Yip et al., 2005).

The results of this study indicate that adding recycled aggregate can improve the mechanical properties of the GCC. This may be for the reasons presented by other research teams with regards to calcium modifying the microstructure of the geopolymer matrix. To proceed with the practical study of GCC in this research, a mix incorporating 45% recycled aggregate was selected for further analysis. The mix is referred to as GCC-R throughout this dissertation.

CHAPTER 4: BEAM TESTS

The ability of geopolymer cement concrete (GCC) to be formed into structural members that are common in precast concrete construction, as well as its ability to develop compressive strength similar to that of Portland cement concrete (PCC) make structural uses a prime application. The engineering properties of geopolymer cement concrete have been evaluated using small specimens, but they have only rarely been demonstrated in scaled structural concrete elements. In this phase of the research, a series of mild steel reinforced concrete beams and prestressed concrete beams were created and destructively tested to demonstrate the performance of GCC in structural applications as well as to verify the relevance of existing concrete design formulas.

4.1 Concrete for demonstration beams

4.1.1 Concrete mixture proportions

The concrete mix used to create the demonstration beams featured the mix designs developed and described in CHAPTERS 2 and 3 of this dissertation and are summarized in TABLE 4-1. Each series of beams (the mild steel reinforced beams and the prestressed beams) included a GCC with virgin aggregates mixture, a GCC with recycled aggregates mixture and a PCC with virgin aggregates mixture as a reference.

TABLE 4-1: Mix designs for concrete used to prepare beam specimens, lb/yd^3 (kg/m^3).

Component	Mix Designation			
	GCC-1	GCC-2	PCC-1	GCC-R
Portland Cement	0	0	386 (229)	0
Fly Ash	834 (495)	835 (495)	89 (53)	815 (483)
Water	274 (163)	275 (163)	173 (103)	268 (159)
NaOH	83 (49.5)	84 (49.5)	0	81 (48)
Silica Fume	62 (37.1)	63 (37.1)	0	61 (36)
Fine Aggregate	1,336 (793)	1,336 (793)	709 (421)	1,304 (773)
Coarse Aggregate	1,336 (793)	1,336 (793)	1,127 (669)	718 (426)
Recycled Coarse Aggregate				587 (348)

4.1.2 Mixing the concretes

The dry ingredients were weighed out into 55 gallon (200 liter) drums several days ahead of time and left in the ambient conditions of the workshop to equilibrate. The activator was similarly proportioned and mixed in a 55 gallon (200 liter) drum that was fitted with a special valve for dosing it into the mixer truck in a controlled fashion. The activator drum was placed into an oven and held at 167°F (75°C) overnight.

The GCC was mixed in a ready-mix truck designed for delivering small batches of PCC. As much as was practicable, the same mixing procedure designed for the smaller batches of GCC made during previous phases of the research was used here. The dry ingredients were added to the drum of the truck with 1/3 of the water, as shown in FIGURE 4-1. After the dry ingredients were well combined, the activator was added and the mixer ran for 250 revolutions. The mixing period lasted approximately ten minutes beyond the addition of the activating solution.

FIGURE 4-1: Adding materials to mixing truck.

After the mixing period, the truck was able to enter the lab facility where the formwork and reinforcing had been prepared. GCC was added to the molds and a vibrator was used to ensure proper consolidation. Due to the flowable nature of the GCC, the truck was able to pause at just a few positions along the beam in order to deliver concrete to the whole length. As the beams were filled, an assortment of 3”x6” (76mmx152mm) cylinder specimens was also prepared. A curing oven was assembled over the specimens and they were left to age for two days before heaters inside the oven were started. The heaters maintained a 167°F (75° C) curing condition for two more days. The oven is shown in FIGURE 4-2. The beams were identified as per the descriptions in TABLE 4-2.

The PCC used to prepare the reference beams was sourced from a local ready-mix plant and delivered in the same mixer truck that mixed the GCC batches. The mix design is given as PCC-1 in TABLE 4-1.

FIGURE 4-2: Beam and heater inside curing oven.

4.2 Mild steel reinforced beams

Four mild steel reinforced concrete beams were prepared. Each beam reflected a variation either in the concrete materials or the reinforcing. TABLE 4-2 describes the characteristics of each beam. The cross-section GCC-1-B1 is shown in FIGURE 4-3 with reinforcing details in TABLE 4-3. Elevations, cross sections, and reinforcement details of GCC-2-B2, PCC-1-B3 and GCC-R-B4 are shown in FIGURE 4-4 and TABLE 4-4.

TABLE 4-2: Concrete cylinder compressive strength at time of testing.

Beam ID	Concrete Mix	Characteristic	Compressive Strength, psi (MPa)
GCC-1-B1	GCC-1	First batch of geopolymer cement concrete with virgin aggregates	11,000 (75.8)
GCC-2-B2	GCC-2	Second batch of geopolymer cement concrete with virgin aggregates	11,900 (82.0)
PCC-1-B3	PCC-1	Portland cement concrete	12,500 (86.2)
GCC-R-B4	GCC-R	Geopolymer cement concrete with 45% recycled aggregates	9,200 (63.4)

The beams were designed to achieve a ductile, flexural failure, with the longitudinal reinforcing steel reaching yield in tension well before the compression concrete began compressive crushing. For preliminary design, a speculative strength of 6,500 psi (45 MPa) was assumed, although much higher strengths were ultimately obtained. This affected the applicability of the initial design calculations, however, all beams achieved ductile failures.

TABLE 4-3: Reinforcing steel schedule for GCC-1-B1, inches (mm).

Bar Type	Grade	Diameter	Dimension					
			1	2	3	4	5	6
A	40	0.625 (15.9)		140 (3,560)				
B	60	0.375 (9.5)	4.5 (114)	5.0 (127)	9 (229)	5 (127)	9 (229)	4.5 (114)

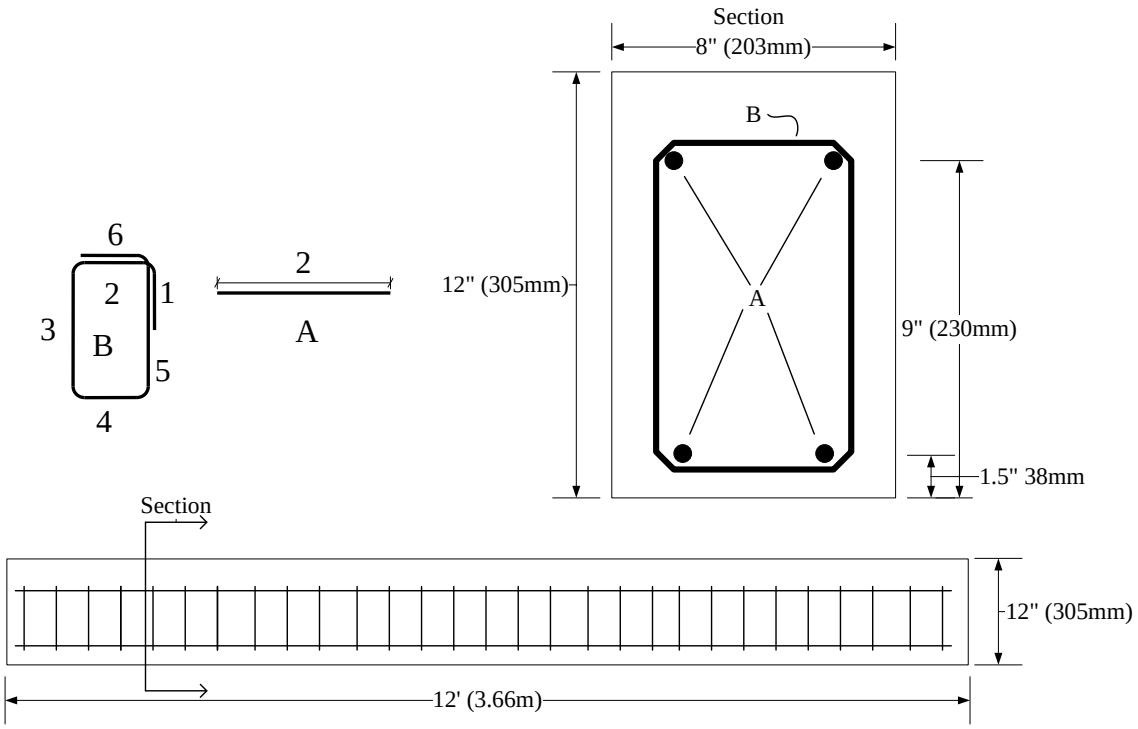

Stirrups spaced 5” (127mm) on center

FIGURE 4-3: Placement and size of reinforcing steel in GCC-1-B1.

TABLE 4-4: Reinforcing steel schedule for GCC-2-B2, PCC-1-B3 and GCC-R-B4.

Bar Type	Grade	Diameter	Dimension					
			1	2	3	4	5	6
A	60	0.5 (12.7)		140 (3,560)				
B	60	0.375 (9.5)	4.5 (114)	5.0 (127)	9 (229)	5 (127)	9 (229)	4.5 (114)

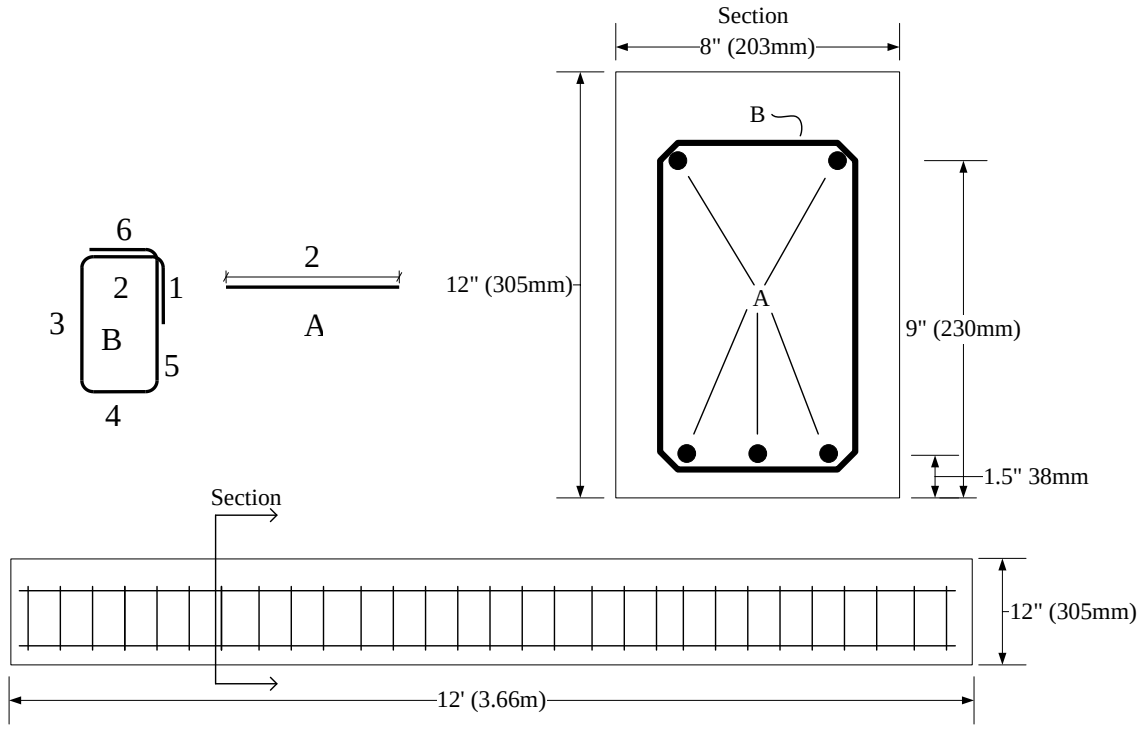

Stirrups spaced 5” (127mm) on center

FIGURE 4-4: Placement and size of reinforcing steel in GCC-2-B2, PCC-1-B3, and GCC-R-B4.

4.2.1 Test set-up for the mild steel reinforced beams

Beams were supported and loaded as shown in FIGURE 4-5. Equal loads were applied at the 1/3 span points. Displacements were measured at the beam centerline as well as directly under the loading points. The load was applied through a deep steel spreader beam and was generated with a hydraulic cylinder mounted to the load-frame. The application rate was metered with a manually controlled hydraulic pump and metered such that it increased at 100 lb per second (445 N per second). FIGURE 4-6 shows an example of the beam loaded in the test frame. Also visible in the picture are the spreader beam, as well as the loading jack. At the beams end supports, plates were provided between the support rollers and the bottom of the beams to prevent crushing. These are shown in FIGURE 4-7.

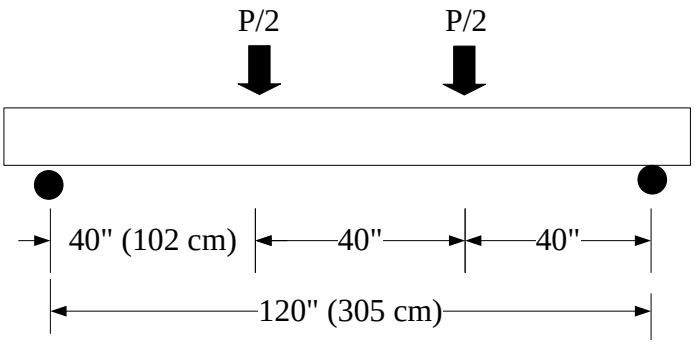

FIGURE 4-5: Beam loading and support geometry.

FIGURE 4-6: Mild steel reinforced beam loaded in the test frame.

FIGURE 4-7: Support conditions for mild steel reinforced beams.

4.2.2 Instrumentation

Four general purpose strain gages were mounted on the reinforcing bars. Two gages were on the bottom bars and two gages on the top bars. The gages were protected

with vinyl adhesive tape as shown in FIGURE 4-8. The load was measured with a pressure transducer capable of readings from 0-10,000 psi (0-69 MPa) attached to the pump. Displacements were measured directly beneath the load application points and at midspan by cable extension transducers. All data was recorded at the rate of 1 Hz with a National Instruments data acquisition system attached to a PC.

FIGURE 4-8: Strain gage mounted to reinforcing steel.

4.2.3 Performance of the mild steel reinforced beams

The response of reinforced concrete beams to increasing loads can be observed by deflection measurements along the length of the beam. FIGURE 4-9 depicts the relationship between load and deflection that is typical of reinforced concrete beams. The load history is marked by the events labeled “A” through “D” on the diagram and described in TABLE 4-5.

TABLE 4-5: Description of reinforced concrete beam load history.

Event	Description
A	First crack
B	Initiation of tensile steel yielding
C	Initiation of concrete crushing in compression
D	Rupture of concrete in compression

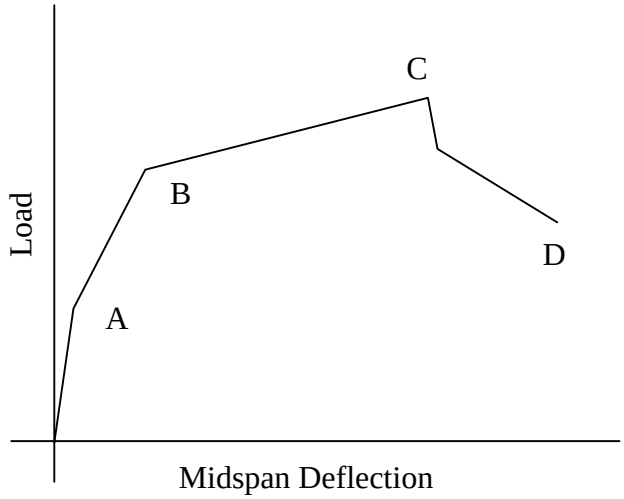

FIGURE 4-9: Load-deflection relationship for reinforced concrete beams.

As the beams were designed to achieve a ductile failure, they all exhibited similar behavior. Each failure was characterized by a long period of steel yielding, during which cracks grew and the deflection increased prominently. Completion of the test was marked by the rupture of concrete in the compression zone.

The moment-midspan deflection charts are given in FIGURE 4-10 through FIGURE 4-13. In the case of GCC-1-B1, the test was inadvertently discontinued prior to ultimate failure, so a full load-deflection profile is not available. However, all other beams exhibited the type of behavior anticipated (see FIGURE 4-9).

FIGURE 4-14 provides a comparison of the four beams' load-deflection behavior. There is a large variation in the magnitude to the load which caused initial concrete cracking and also the magnitude of the ultimate moment. However, the deflection behavior which is related to the elastic and inelastic properties of the steel reinforcing is uniform for all beams. This is reflected in the slope of the load-deflection curve between points A and B, and B and C (as identified in FIGURE 4-9).

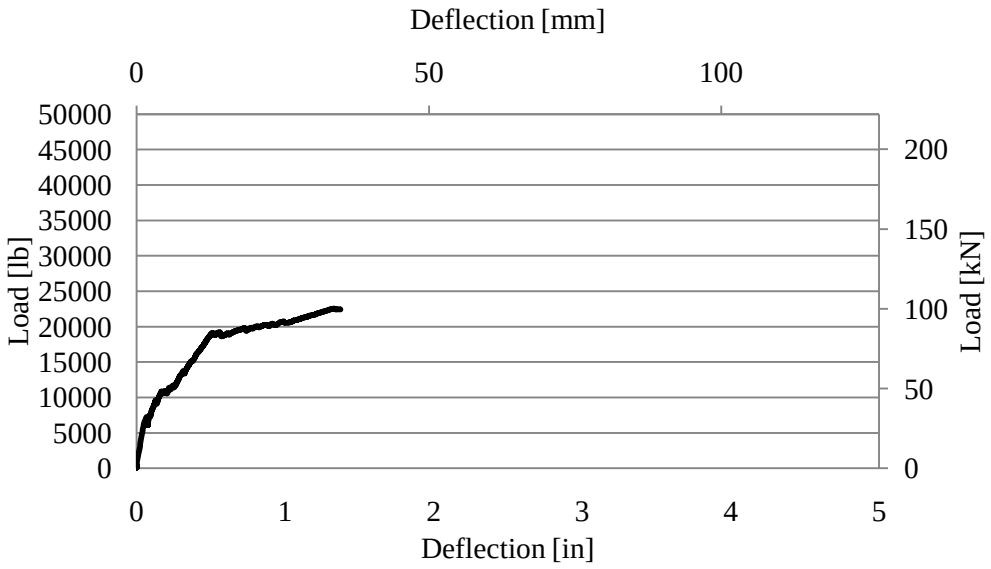

FIGURE 4-10: GCC-1-B1 load vs. mid-span deflection.

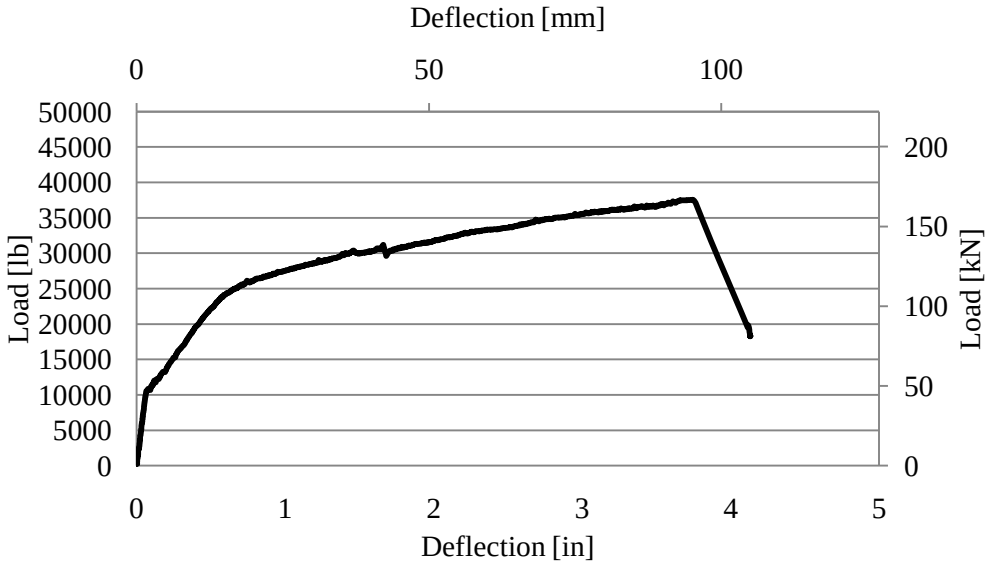

FIGURE 4-11: GCC-2-B2 load vs. mid-span deflection.

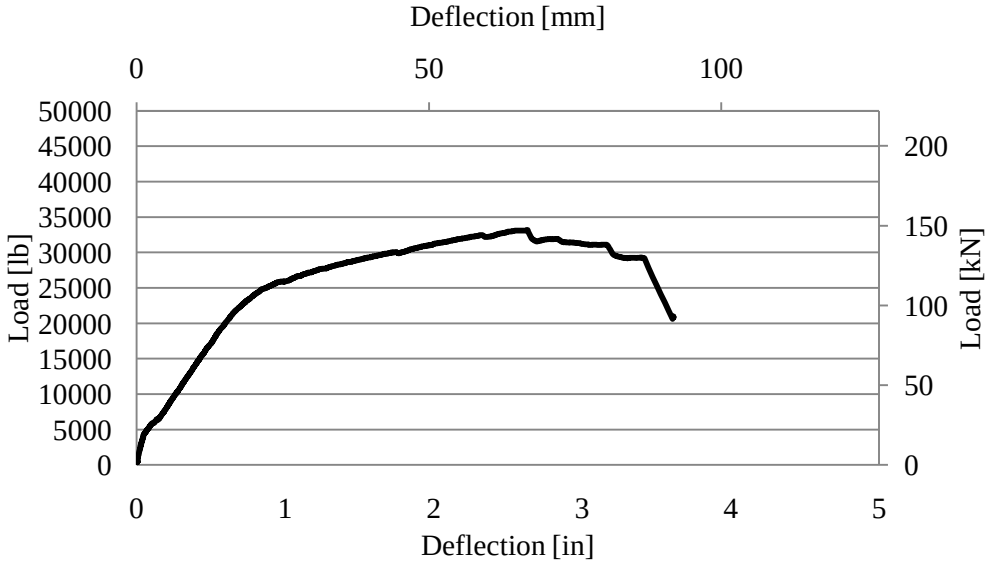

FIGURE 4-12: PCC-1-B3 load vs. mid-span deflection.

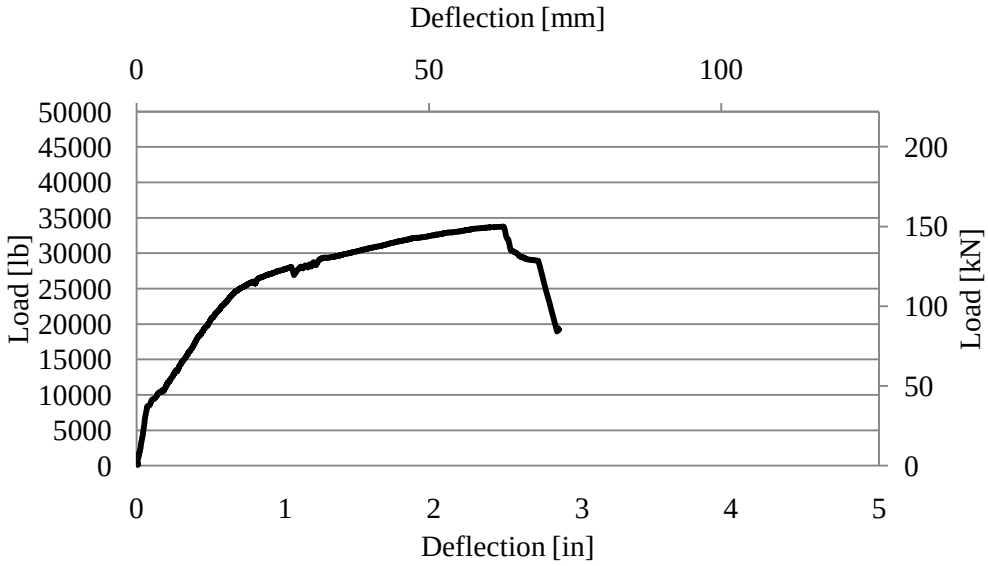

FIGURE 4-13: GCC-R-B4 load vs. mid-span deflection.

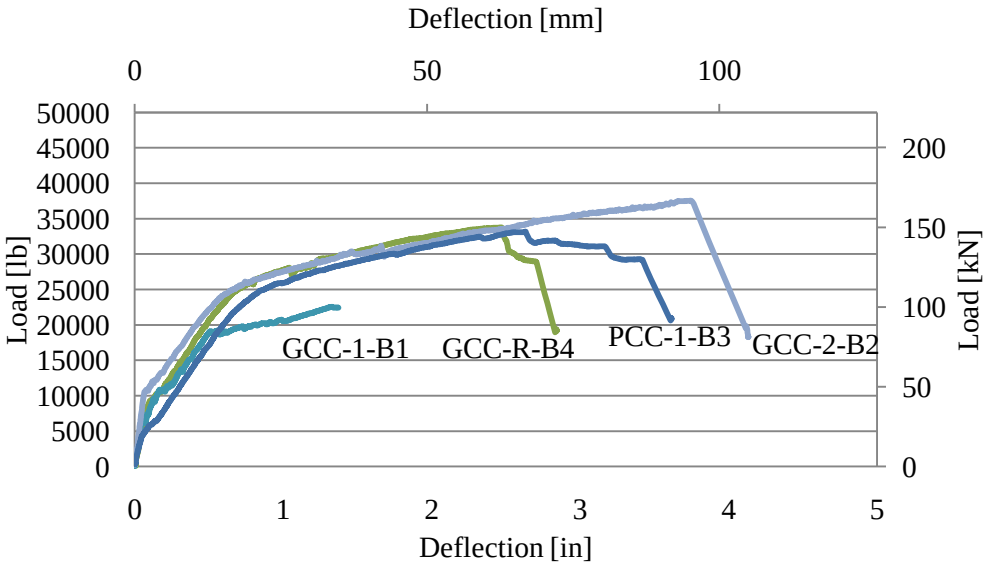

FIGURE 4-14: Combined plots of load vs. mid-span deflection.

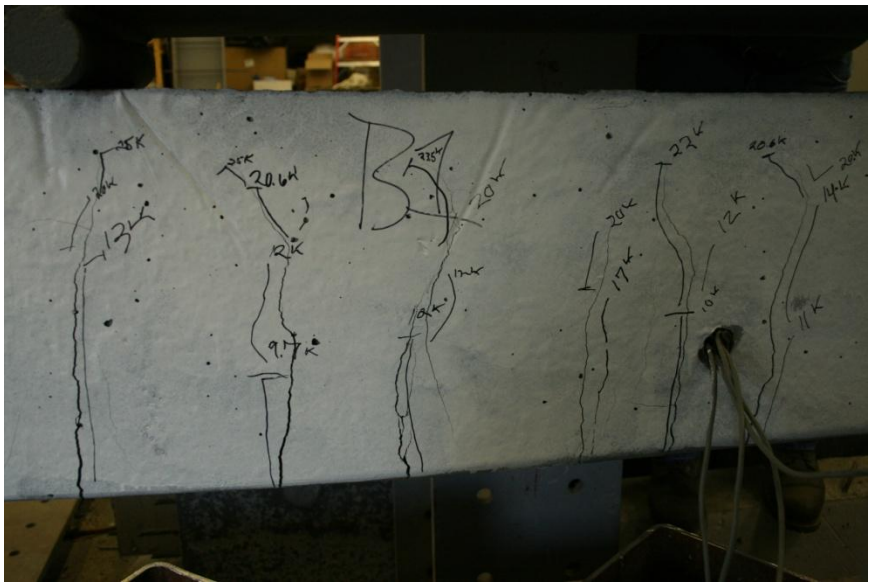

FIGURE 4-15: GCC-1-B1 at maximum load.

FIGURE 4-16: Crushing failure in GCC-2-B2.

FIGURE 4-17: Crushing failure in PCC-1-B3.

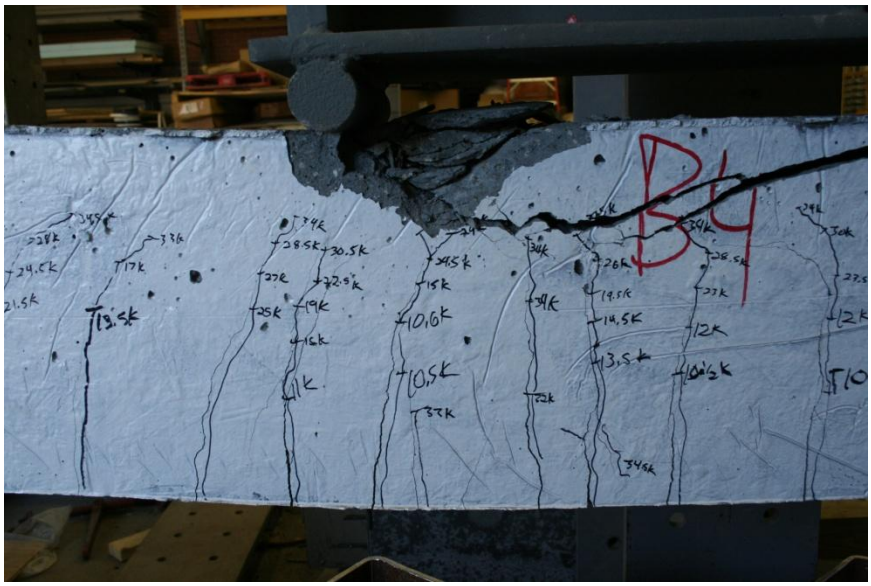

FIGURE 4-18: Crushing failure near load application in GCC-R-B4.

4.3 Prestressed concrete beams

Three prestressed concrete beams were prepared. As with the mild steel reinforced beams, each beam featured a different concrete mix, as described in TABLE 4-6.

TABLE 4-6: Prestressed beam concrete details.

Beam ID	Concrete Mix	Characteristic	f'_c, psi (MPa)
GCC-2-P2	GCC-2	Second batch of geopolymer cement concrete with virgin aggregates	11,900 (82.0)
PCC-1-P3	PCC-1	Portland cement concrete	12,500 (86.2)
GCC-R-P4	GCC-R	Geopolymer cement concrete with 45% recycled aggregates	9,200 (63.4)

4.3.1 Beam design and construction

FIGURE 4-21 shows the cross section and reinforcing details of the prestressed concrete beams. In addition to the stirrups shown in the figure, extra 8" (200 mm) steel hoops were placed around the prestressing strands within 300 mm of the end of the beam to prevent rupture of the concrete during prestress transfer, as shown in FIGURE 4-20. All steel was grade 60. Stirrups were #3 (71 mm^2) bars and longitudinal steel was #4 (129 mm^2) bars. Prestressing tendons were 0.5" (13mm) diameter, seven wire, grade 270, low relaxation strand. Stress-strain profiles for all the reinforcing steel products are available in Appendix A.

As with the mild reinforced concrete beams, the formwork was lined with polyethylene sheeting to preserve the wood, as shown in FIGURE 4-19. Cover blocks were used on the sides and bottom of the reinforcing cage in order to maintain the desired geometry and cover. Since the forms were 18" (457mm) tall, cross-ties braced the top of

the formwork from bowing under the pressure of the fresh concrete. These ties are also visible in FIGURE 4-19.

FIGURE 4-19: Reinforcing cage and prestressing tendons in formwork.

FIGURE 4-20: Extra reinforcing near the end of the prestressed beams.

TABLE 4-7: Reinforcing steel schedule for GCC-2-B2, PCC-1-B3 and GCC-R-B4, in (cm).

Bar Type	Grade	Diameter	Dimension					
			1	2	3	4	5	6
A	60	0.5 (1.27)		212 (538)				
B	60	0.375 (.95)	4.5 (114)	8.0 (20)	16 (41)	8 (20)	16 (41)	4.5 (11)
C	270	0.5 (1.27)		216 (549)				

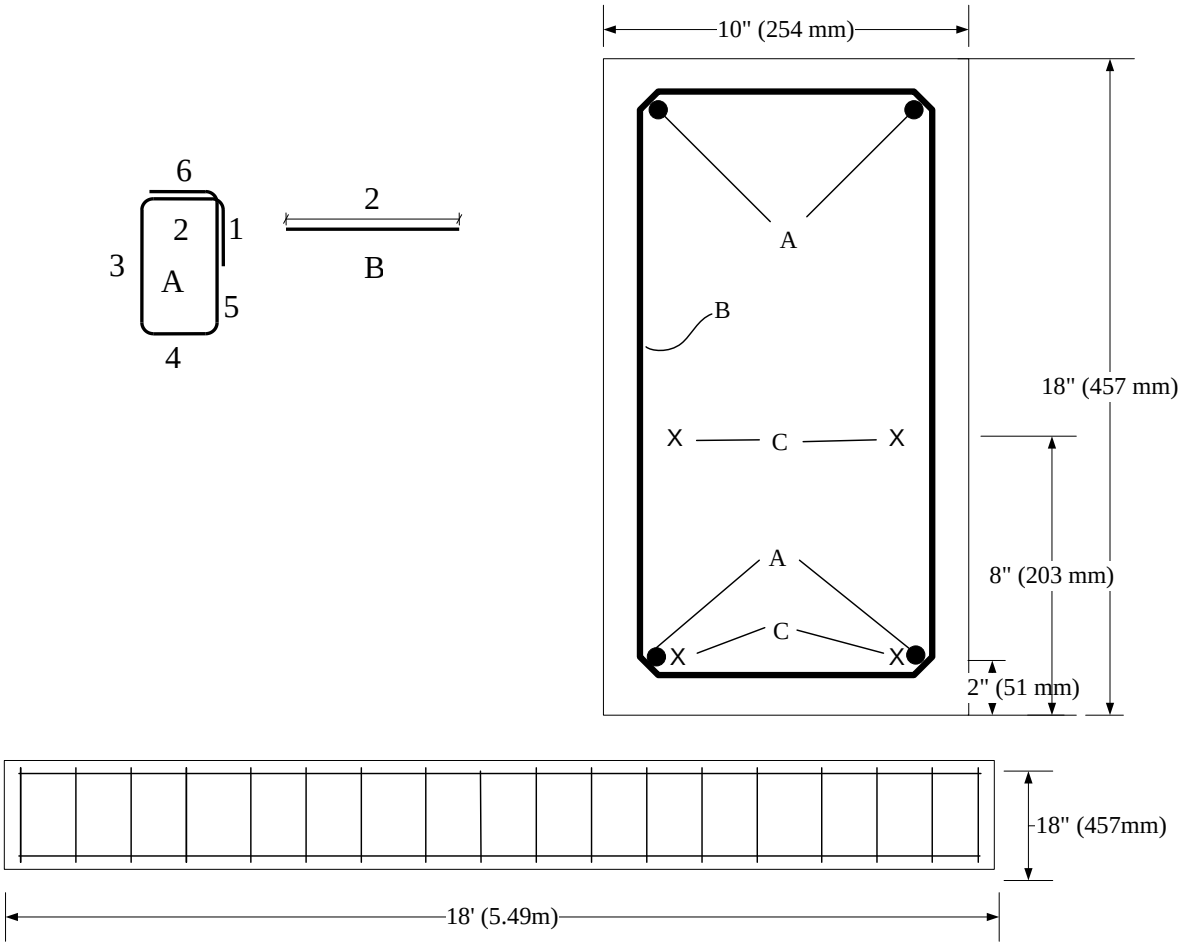

Stirrups spaced 12” (305mm) on center

FIGURE 4-21: Reinforcing steel placement and beam cross section for prestressed beams.

4.3.2 Prestressing the beams

The three beams were prestressed in-house. This was accomplished by constructing the formwork and reinforcing cage between two abutments in a strong-wall load frame. The strands were secured to the abutments with reusable prestressing strand chucks and were tensioned with a hollow-core hydraulic jack. The configuration of the jack and chucks is shown in FIGURE 4-22. The chucks and abutments are shown in FIGURE 4-23. During the prestressing operation, tension on the strand was measured with a pressure transducer attached to the hydraulic hose as well as by a load cell mounted between the strand chuck and the jack. The tension was maintained by the abutment throughout the casting and curing phase of beam construction. Once cylinder tests ensured that the concrete had developed sufficient strength to transfer prestress from the abutments to the beam, the strands were cut with an acetylene torch.

After prestressing beams GCC-2-P2 and PCC-1-P3, it was noted that some prestress was being lost as the load was transferred from the jack to the chuck. This loss occurred as the jaws of the chuck slid into the bore of the chuck. For GCC-R-P4 a set of rudimentary load cells were fabricated by attaching strain gages to thick steel tubes that were mounted between the chuck and the abutment. With these load cells, it was possible to continue monitoring tension in the strand after the jack was removed. It was noted that approximately 30% of the prestress was lost due to chuck seating. This was accounted for in subsequent computations requiring values for effective prestress.

FIGURE 4-22: Jacking configuration used to tension prestressing tendons.

FIGURE 4-23: Prestressing tendons passing through the abutment.

4.3.3 Prestressed concrete beam test set-up

Using the test set-up shown in FIGURE 4-24, the beams were loaded until they failed. Load was applied through the spreader beam that is visible in FIGURE 4-25 and was generated by a hydraulic jack attached to a manually controlled hydraulic pump. The load application was monotonic and proceeded at a rate of 3,000 lb/sec (13 kN/sec) during the linear portions of the load-deflection history.

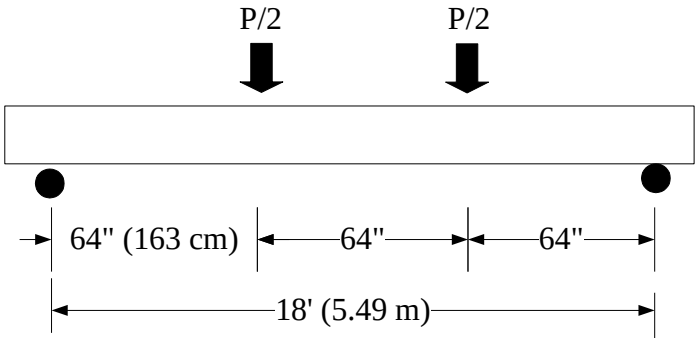

FIGURE 4-24: Prestressed beam test set-up.

FIGURE 4-25: Prestressed beam loaded in the test frame.

4.3.4 Prestressed beam instrumentation and test monitoring

Strain gages were placed on the upper and lower mild steel reinforcing bars at midspan. Although the gages were protected with a vinyl adhesive tape, many of them failed to function during the test. External instrumentation included three cable extension displacement transducers set at midspan, and points directly under the load application plates, as shown in FIGURE 4-24.

The load was measured with a pressure transducer capable of readings from 0-10,000 psi (0-69 MPa) attached to the pump. Displacements were measured beneath the load application points and at midspan by cable extension transducers. All data was recorded at the rate of 1 Hz with a National Instruments data acquisition system attached to a PC. Additionally, the development of crack patterns along the beam was monitored until the beam approached 80% of its predicted failure load, after which the research assistants moved away from the beam for safety.

4.3.5 Prestressed beam test results

FIGURE 4-26 through FIGURE 4-28 present the load-deflection history of the prestressed beams. As is apparent in FIGURE 4-30 through FIGURE 4-32, all beam failures occurred by crushing of the concrete on the compression face of the beam. It should be noted that the crushing originated near one of the loading points for all three prestressed beams. Broad steel plates were used beneath the spreader beam, however localized bearing stresses may have been involved in the failure mechanism for the compression concrete. The failure loads were very similar for all three beams, as is reported in TABLE 4-8. Here the forces have been expressed as midspan flexural

moments as determined by beam geometry and the magnitude of the measured point loads.

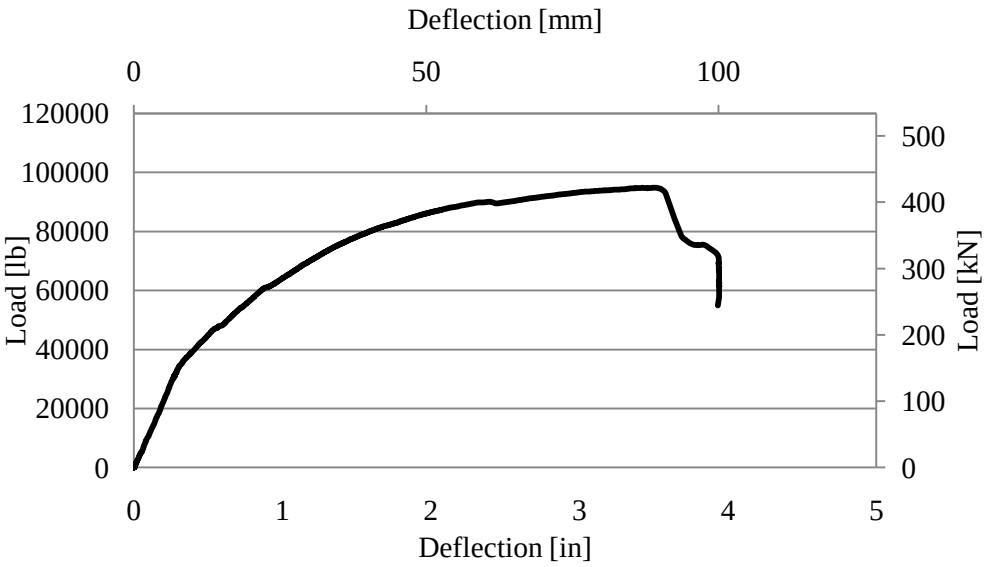

FIGURE 4-26: GCC-2-P1 beam load vs. midspan deflection.

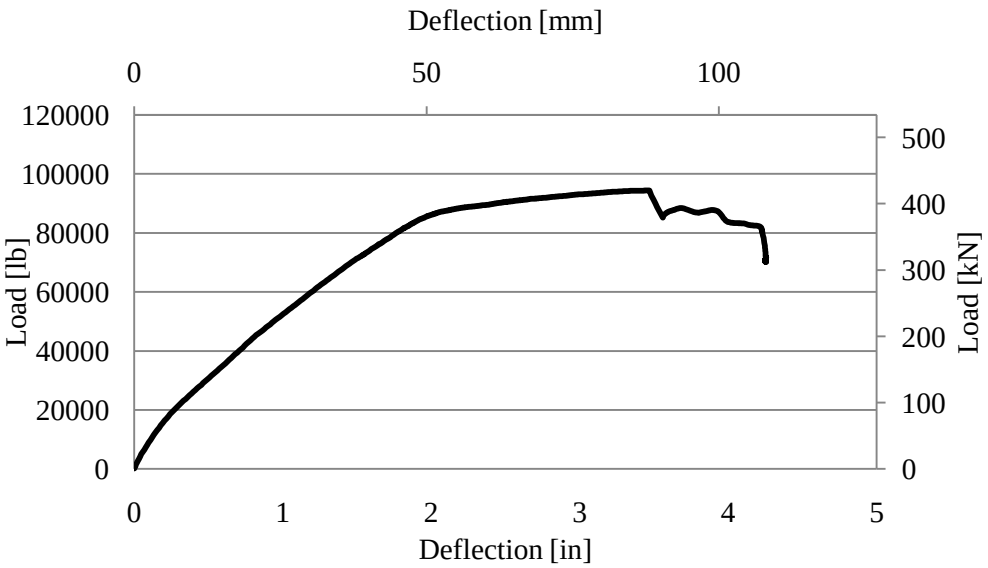

FIGURE 4-27: PCC-1-P2 beam load vs. midspan deflection.

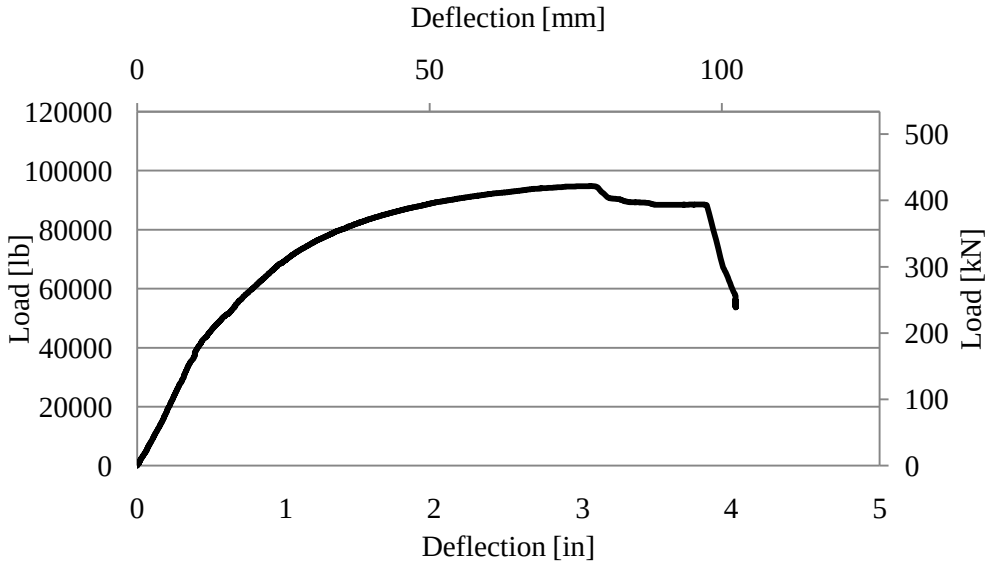

FIGURE 4-28: GCC-R-P3 beam load vs. midspan deflection.

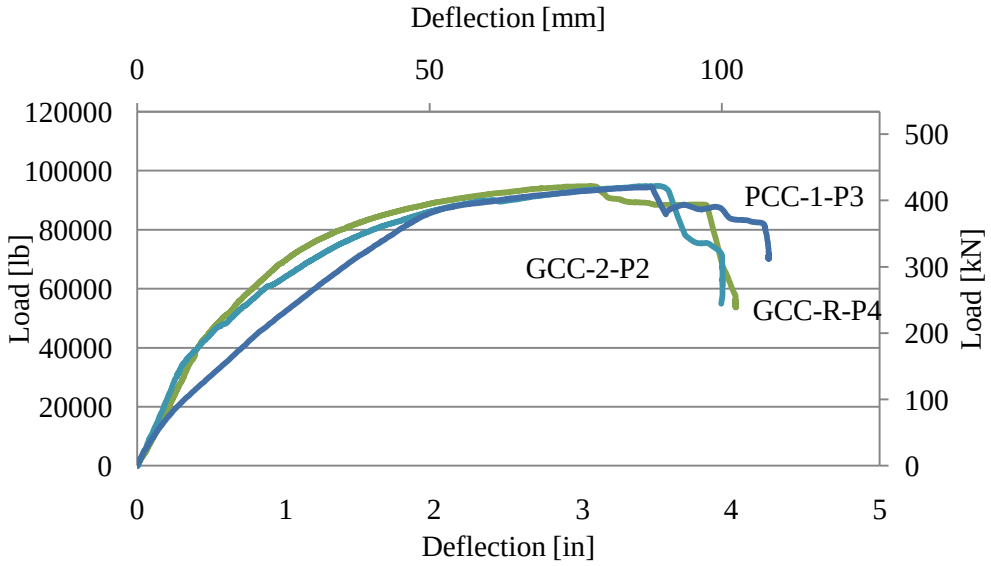

FIGURE 4-29: Load deflection curves for prestressed beams plotted together.

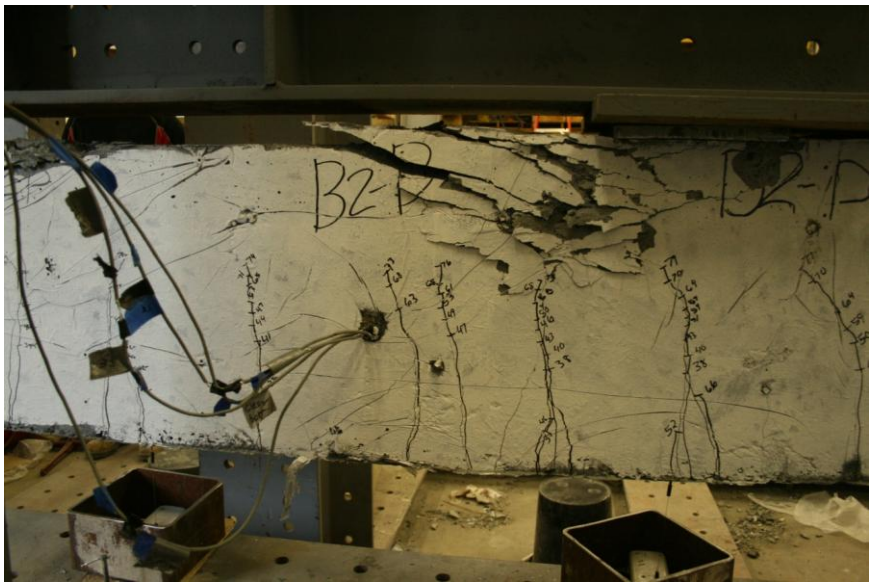

FIGURE 4-30: GCC-2-P1 beam failure by concrete crushing.

FIGURE 4-31: PCC-1-P2 beam failure by concrete crushing.

FIGURE 4-32: GCC-R-P3 beam failure by concrete crushing.

TABLE 4-8: Critical points in prestressed beam load histories.

Beam ID	M_{cr} kip-in (kN-m)	M_n kip-in (kN-m)
GCC-2-P1	989 (118)	3,125 (353)
PCC-1-P2	Not observed	3,112 (352)
GCC-R-P3	1,261 (142)	3,124 (353)

CHAPTER 5: FLEXURAL BEAM-COLUMN TESTS

5.1 Analysis of stress and strain under compressive loading

As stresses in concrete increase beyond approximately 30-40% of the compressive strength, microcracks begin to form. Once this cracking is initiated, the load response of the concrete shifts from one that is essentially linear and elastic to one that is non-linear and inelastic. Thus, the stress-strain relationship resembles that shown in FIGURE 5-1, where the peak stress, f_c', occurs well beyond the linear and elastic portion of the stress-strain curve. Beyond f_c' stress reduces with increasing strain, until a limiting strain, ε_u, is reached. The magnitude of ε_u is taken as 0.003 % for purposes of design (American Concrete Institute, 2008).

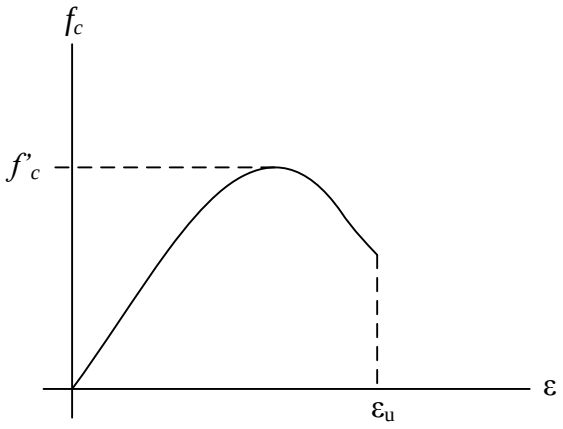

FIGURE 5-1: stress-strain relationship of concrete in compression.

In concrete beams, ultimate failure is typically marked by crushing of concrete at the compression face once strain in this region has reached ε_u. Although it is assumed

that the strain distribution at points throughout the beam cross-section remains linear, the non-proportional relationship between stress and strain results in stress distributions that resemble parabolas. The hatched area in FIGURE 5-2a represents the compression zone of a beam in positive flexure. The strain distribution for this segment of the cross-section is linear as in FIGURE 5-2b; however, these strains are related to stresses as per the curve shown in FIGURE 5-1 and so create the stress distribution shown in FIGURE 5-2c.

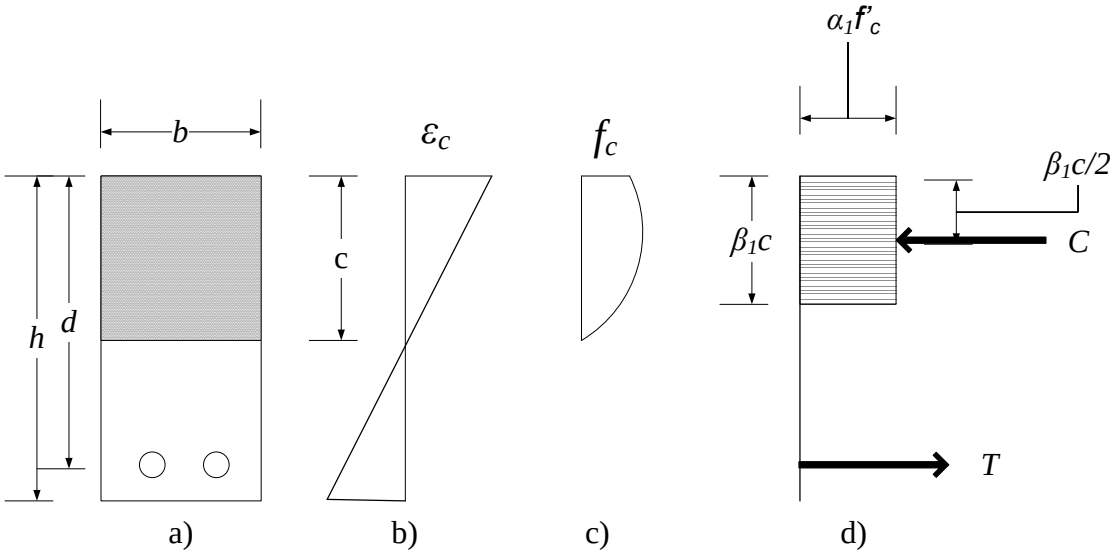

FIGURE 5-2: Stresses and strains in concrete beams.

For design purposes, the Whitney Stress Block, shown in FIGURE 5-2d is used as an approximation of the area enclosed by the parabolic area shown in FIGURE 5-1c (Whitney, 1937). The block is defined by the factors shown in FIGURE 5-3, where:

k_1: ratio of average compressive stress to maximum compressive stress

k_2: ratio of distance from top of beam to the force *C*, and the depth to the neutral axis, *c*

k_3 : ratio of cylinder concrete strength to beam concrete strength

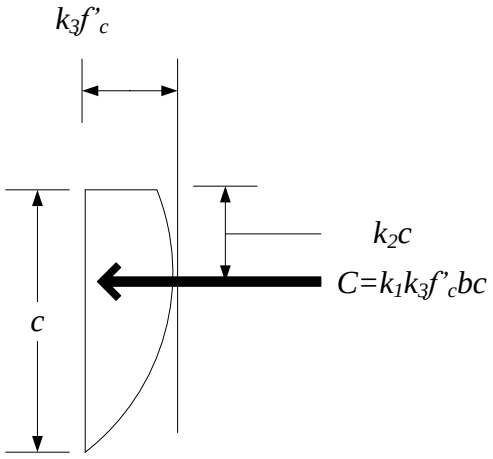

FIGURE 5-3: Relationship of k_1, k_2 and k_3 to the resultant compressive force.

There are many challenges in determining the stress-strain relationship shown in FIGURE 5-1 experimentally. Although concentric compression tests can be used to determine stress-strain relationship through the initiation of crushing, the post-peak behavior is typically obscured by the rapid release of strain energy stored in the testing device. In unreinforced beams, the tensile limit of the concrete is reached well in advance of the ultimate compressive stresses developing. Even in reinforced beams, the impact of tensile stresses and cracks developing below the neutral axis is sufficient to make analysis very difficult. For purposes of estimating k_1 k_2 and k_3 as well as measuring the stress-strain relationship, a combined axial-flexure test was developed by Hognestad (1955).

In this procedure, a short beam-column is loaded axially while an eccentric load is applied through two "arms" attached to the ends of the specimen. The eccentric load produces a moment that maintains a neutral face on one side of the beam-column while the opposite side approaches the compressive strain limit. In this way, the area between

the compression face and the neutral axis of a flexural beam is simulated without the effects of tensile stresses and a shifting neutral axis as would be found in a reinforced beam. As is not possible in concentric tests, the stress and strain gradient that is found in flexural components is duplicated in the test piece. The test geometry is shown in FIGURE 5-4 with P_1 representing the primary axial load and P_2 representing the eccentric load.

Based on static analysis of the system, k_1k_3 and k_2 can be calculated directly from the beam dimensions and the magnitude of the loads P_1 and P_2 shown in FIGURE 5-4 and 5-5. When the maximum stress in the concrete reaches f_c', the resultant compression force, C (as shown in FIGURE 5-3) is equal to the sum of the applied forces, P_1 and P_2. From the free body diagram given in FIGURE 5-5

$$\sum f = 0 = k_1 k_3 f_c' bc - (P_1 + P_2) \tag{5-1}$$

and, solving for k_1k_3

$$k_1 k_3 = \frac{P_1 + P_2}{f_c' bc} \tag{5-2}$$

where b and c are the cross sectional dimensions shown in FIGURE 5-2.

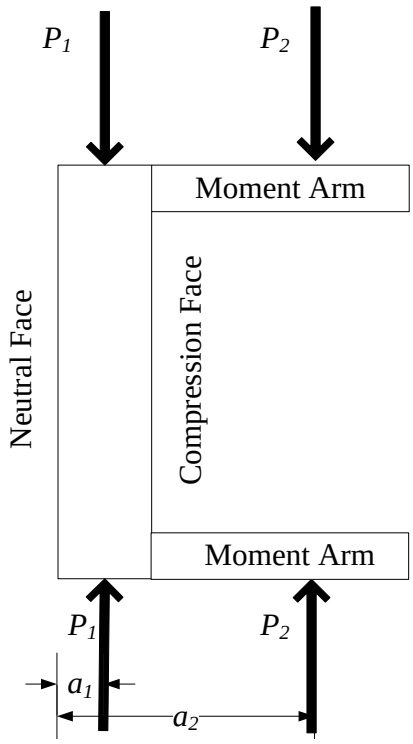

FIGURE 5-4: Hognestad flexural beam-column test set-up.

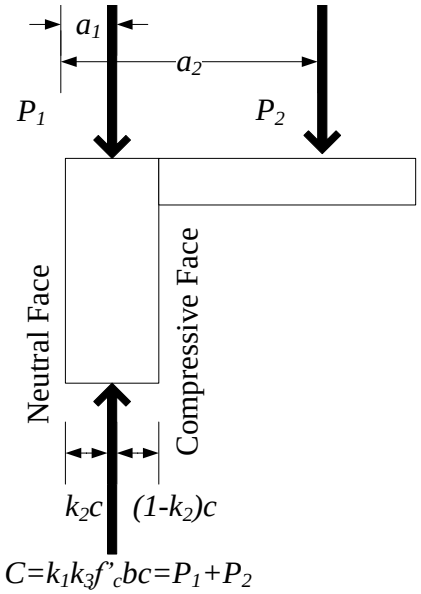

FIGURE 5-5: Free body diagram of the beam-column specimen cut at midheight.

Summing moments about the neutral face of the beam generated by the forces shown in FIGURE 5-5, leads to

$$\sum M = 0 = (P_1 + P_2)(1 - k_2)c - P_1 a_1 - P_2 a_2 \qquad (5\text{-}3)$$

$$k_2 = 1 - \frac{P_1 a_1 + P_2 a_2}{(P_1 + P_2)c} \qquad (5\text{-}4)$$

The relationship between stress and strain must be determined by a process of numerical integration. It is necessary to assume that f_c is a function of ε_c, such that $f_c = F(\varepsilon_c)$ and that ε_c is a linear distribution across c as shown in FIGURE 5-6. However, since the function $F(\varepsilon_x)$ is not known, some substitution of known or measurable quantities must be made to determine f_c from data collected during experiments.

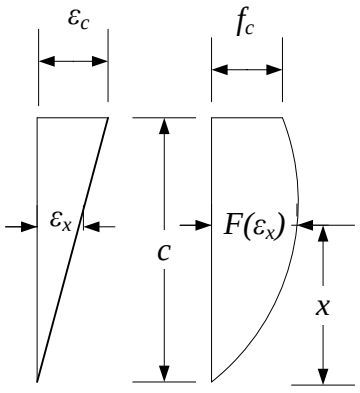

FIGURE 5-6: Quantities f_c, ε_c and c.

C, the resultant compressive force, may be defined by using

$$C = b\int_0^c F(\varepsilon_x)dx = \frac{bc}{\varepsilon_c}\int_0^{\varepsilon_c} F(\varepsilon_x)\, d\,\varepsilon_x = P_1 + P_2 = f_0 bc \qquad (5\text{-}5)$$

and the moment, *M*, by using

$$M = b\int_0^c F(\varepsilon_x)xdx = \frac{bc^2}{{\varepsilon_c}^2}\int_0^{\varepsilon_c} F(\varepsilon_x)\,\varepsilon_x d\,\varepsilon_x = P_1a_1 + P_2a_2 = m_0bc^2 \qquad (5\text{-}6)$$

The average stress on the cross-section is,

$$f_0 = \frac{P_1+P_2}{bc} \qquad (5\text{-}7)$$

and from Equation (5-6), a term for average moment is,

$$m_0 = \frac{P_1a_1+P_2a_2}{bc^2} \qquad (5\text{-}8)$$

Differentiating the third and last terms of Equation (5-5) with respect to ε_c results in Equation (5-9). Substituting the relationship in Equation (5-10), which is obtained by manipulating the third and fifth terms of Equation (5-5), into Equation (5-9) leads to Equation (5-11), in which $\frac{df_0}{d\varepsilon_c}$ is approximately equal to $\frac{\Delta f_0}{\Delta\varepsilon_c}$, two quantities that are measured during testing. The unknown function $F(\varepsilon_x)$ has been removed from the analysis, permitting the measured quantities P_1, P_2 and ε_c to be used to directly calculate f_c.

$$\int_0^{\varepsilon_c} F(\varepsilon_x)\,d\varepsilon_x = f_0\varepsilon_c \qquad (5\text{-}9)$$

$$f_c = \frac{df_0}{d\varepsilon_c}\varepsilon_c + f_0 \qquad (5\text{-}10)$$

Using the same strategy

$$f_c = \frac{dm_0}{d\varepsilon_c}\varepsilon_c + 2m_0 \quad (5\text{-}11)$$

5.2 Flexural beam-column test procedure

5.2.1 Specimen preparation

In order to carry out the flexural test to collect the quantities described above, a series of five beam-columns were constructed. The specimens had the cross sectional and elevation details shown in FIGURE 5-7. The formwork was constructed of ¾" (19mm) thick oriented strand board and was heavily braced in order to maintain its geometry under the pressure of the fresh concrete. The forms were also lined with polyethylene sheeting in order to prohibit the absorption of water or the alkaline activator by the wood. The beam-columns were cast in an upright orientation as shown in FIGURE 5-8.

Sleeves fabricated from 3/8" (9.5mm) thick 8"X8" (203mmx203mm) square tubing were cast onto each end of the specimen. The holes were precisely located to accommodate the bolting pattern from the moment arm end-plates (FIGURE 5-9).

Passages for the bolts were blocked out with lengths of PVC pipe that were removed after the concrete hardened. Hoops bent in grade 60, #3 (metric #10) rebar provided reinforcing inside of the sleeve. #4 (metric #13) bars extended 9" (229mm) beyond the end of the sleeve in order to transfer forces from the loaded ends of the beam-column into the unreinforced central portion of the specimen. The end reinforcing is shown in FIGURE 5-10.

The specimens were instrumented with five concrete strain gages manufactured by Vishay, as shown in FIGURE 5-11. Two gages were mounted on the compression face of the beam-column and two were mounted on the neutral face within 2” (51mm) of the centerline. A single gage was also mounted on one of the side faces. These gages were attached with the AE-10 epoxy kit manufactured by Vishay.

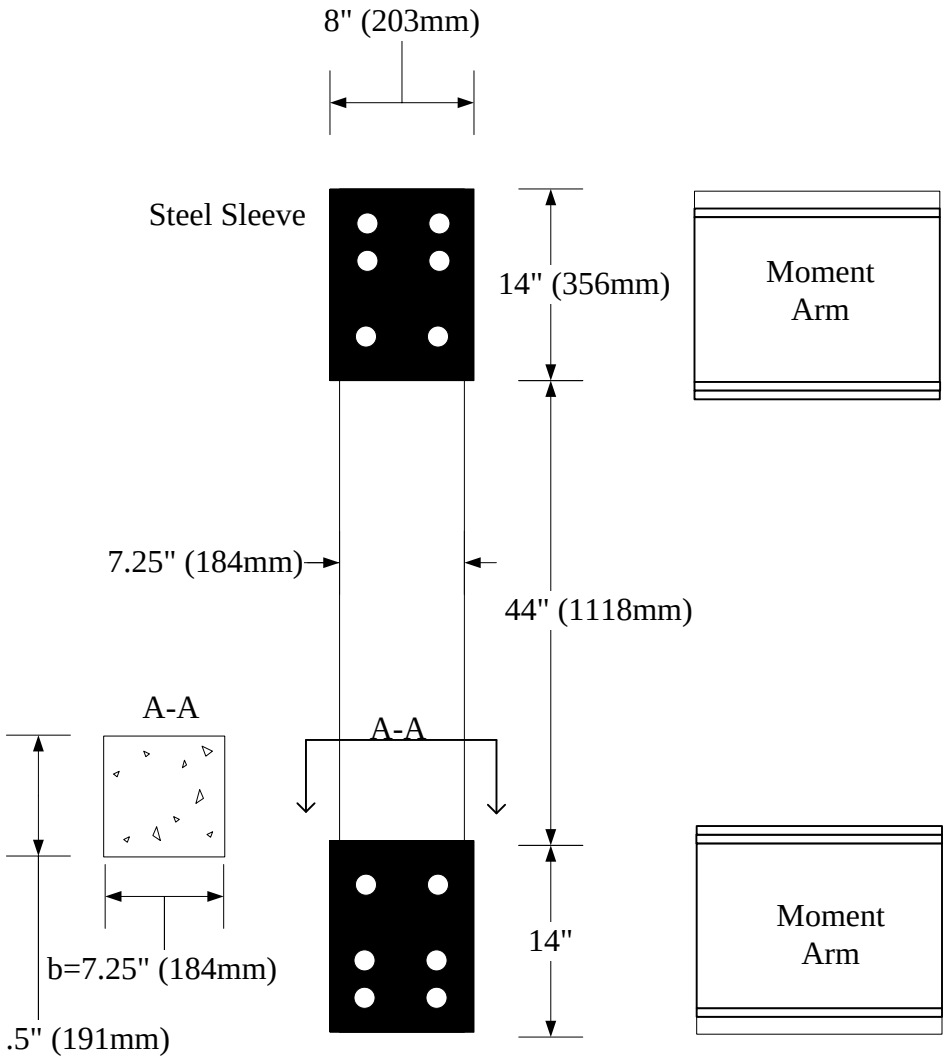

FIGURE 5-7: Beam-column specimen dimensions.

FIGURE 5-8: Casting beam-column specimens.

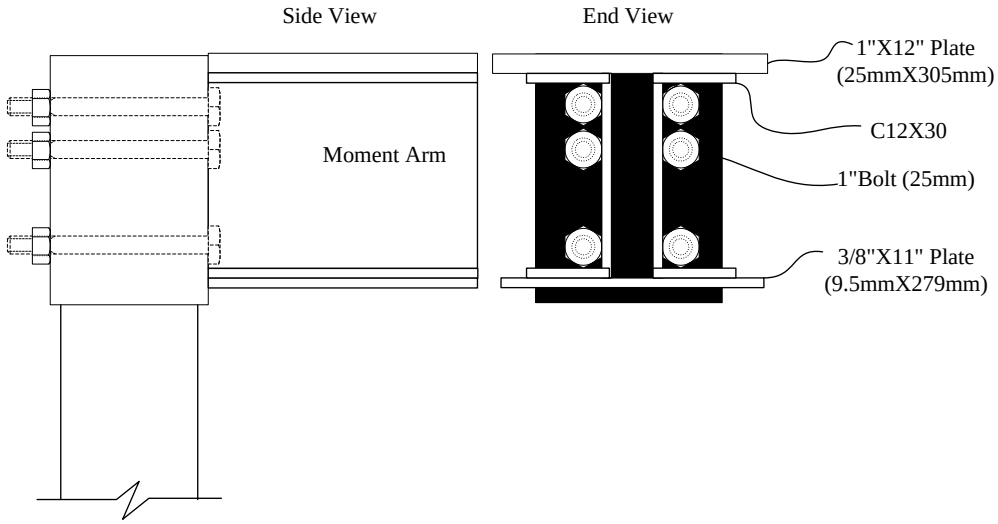

FIGURE 5-9: Moment arm section and end-plate details.

FIGURE 5-10: Reinforcing at the ends of the beam-columns.

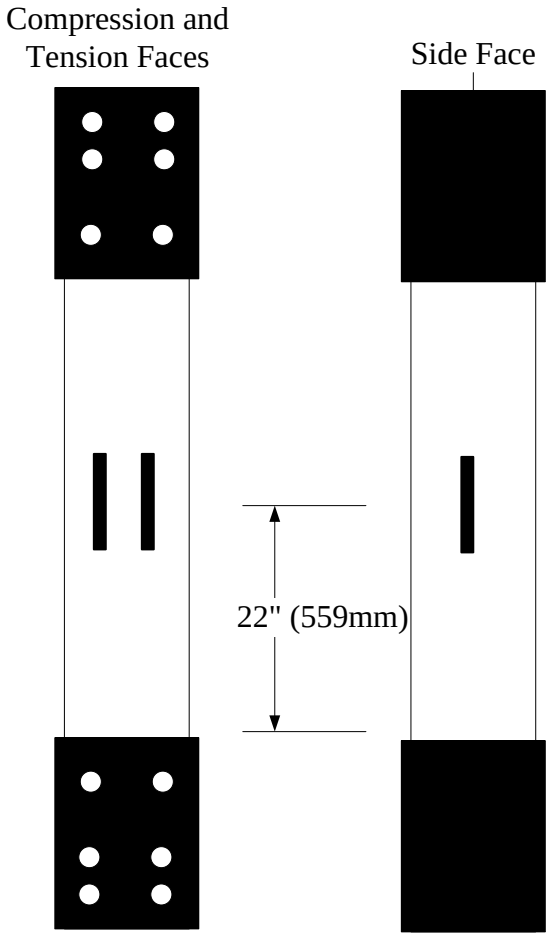

FIGURE 5-11: Strain gage locations on beam-column specimens.

5.2.2 Loading apparatus

Cross sectional details for the steel moment arms are given in FIGURE 5-9. The arms were fixed to the specimens with six, 1" (25.4mm) diameter bolts. The arms were secured to the load frame with loose chains that did not impede their movement during the test but kept them under control after specimen failure. The beam-columns were loaded in an apparatus that was built into the load frame at UNC Charlotte. Two 4' (1.2m) sections of steel were bolted to the bottom rung of the load frame to form abutments, as shown in FIGURE 5-12. Also in FIGURE 5-12 is the 420 ton (4,000 kN)

jack that applied the primary axial load, P_1. The end-plate of the abutment was stiffened to prevent deformation as the axial load was applied. The force was transferred to the specimen through a roller system consisting of 3" (76mm) thick steel plate with a trough machined along the middle to accept a 2" (51mm) diameter bar (FIGURE 5-12). Although the top surface of the specimen had been float finished during casting, a sheet of ¾" (19mm) plywood was placed between the roller and the specimen in order to accommodate any high spots. Force was generated by a manually controlled hydraulic pump. The flow-rate was regulated to apply approximately 500 lb/sec (2.2 kN/sec) to the specimen and the load was measured with an electronic pressure transducer.

FIGURE 5-12: 4' abutment, primary axial load application piston and end roller.

The secondary, moment load was applied via heavy steel cantilevers bolted to the specimen through the holes in the end sleeve, as shown in FIGURE 5-7. The steel sections used to create the moment arm are shown in FIGURE 5-9. A 30 ton (300 kN) hollow core jack applied the load P_2 to the moment arms through a 0.6" (15.2mm)

diameter prestressing strand anchored with a strand chuck as shown in FIGURE 5-13. Force was generated by a hand-operated pump connected to the jack. The load was applied as needed to maintain the lower face of the beam-column at zero strain within 50 millionths. The magnitude of P_2 was measured with a 50,000 lb (222 kN) load cell.

FIGURE 5-13: Application of P_2 with a 30 ton jack and prestressing strand.

FIGURE 5-14: Full test set-up for flexural beam columns.

5.3 Test results and data reduction

A set of 3”x6” (76mmx152mm) cylinders was cast with each of the five beam-column specimens. These cylinders were tested to determine the cylinder compressive strength on the same day as the beam-column tests. The compressive strength results are given in TABLE 5-1. Although all mixes followed the same proportioning, there is great variation in the compressive strength. During the mixing process, small amounts of water were added to the concrete to improve workability. This addition was not closely monitored but seems to have sufficiently affected the w/c ratio to cause reductions in concrete strength.

TABLE 5-1: Cylinder compressive strength for beam-column concrete.

Beam-Column	f'_c , psi (MPa)
GCC-3-BC1	7,900 (54)
GCC-4-BC2	9,000 (62)
GCC-5-BC3	6,700 (46)
GCC-6-BC4	7,300 (50)
GCC-7-BC5	4,000 (28)

During the testing process, measurements were recorded by a data acquisition system set to make a reading twice per second. The system recorded the loads P_1 and P_2, strain from each of the five strain gages and displacement at the inside and outside of the beam at midspan. As each test required approximately 15 minutes to complete, the quantity of data recorded was too great for the numerical integration technique that was to be employed to analyze the results. Small errors in each collected data point, which are caused by the accuracy limits of the instruments as well as electromagnetic interference,

translated into considerable scatter in the analysis output. Therefore, prior to performing the integration, each data set was reduced in size by 95% by selecting one point out of each 20 that was defined by the average value of the 10 points ahead and 10 points behind. This provided a moving average while reducing the number of data points from approximately 1,800 per test to fewer than 100, based on the actual duration of each test.

The displacement data recorded during the test was used to compute additional stresses caused by secondary moments. These additional stresses were calculated with

$$m_0 = \frac{P_1(a_1+e)+P_2(a_2+e)}{bc^2} \quad (5\text{-}12)$$

where e is eccentricity (in) (mm)

5.3.1 Neutral face strain and midspan eccentricity

FIGURE 5-15 through 5-24 display the strain recorded on the neutral face of the beam during the loading as well as the midspan deflection due to the applied forces. In all cases, the eccentricity was less than 0.1" (2.54mm). Strains were controlled within about 20 millionths at points prior to the failure approach.

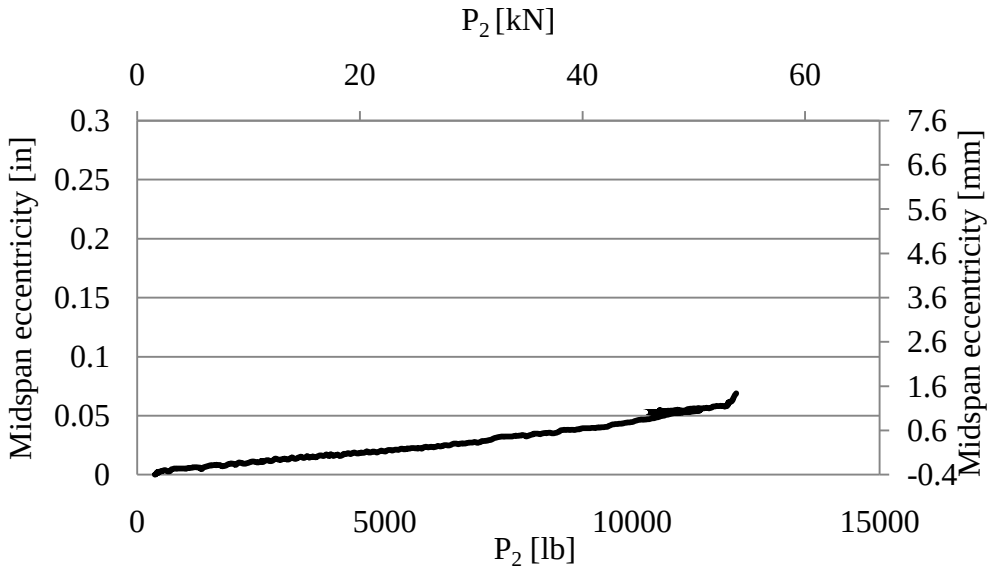

FIGURE 5-15: Midspan deflection vs. P_2 for GCC-3-BC1.

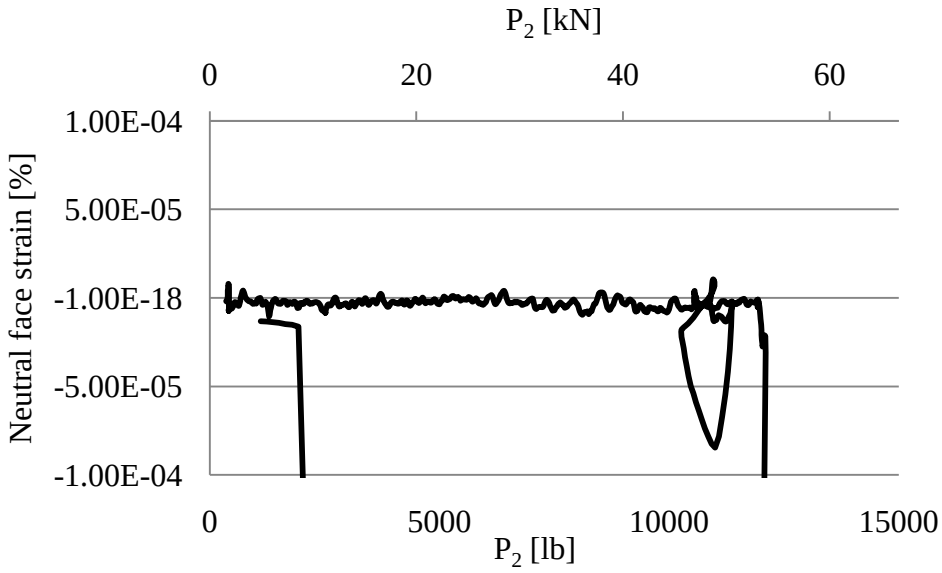

FIGURE 5-16: Neutral face strain vs. P_2 for GCC-3-BC1.

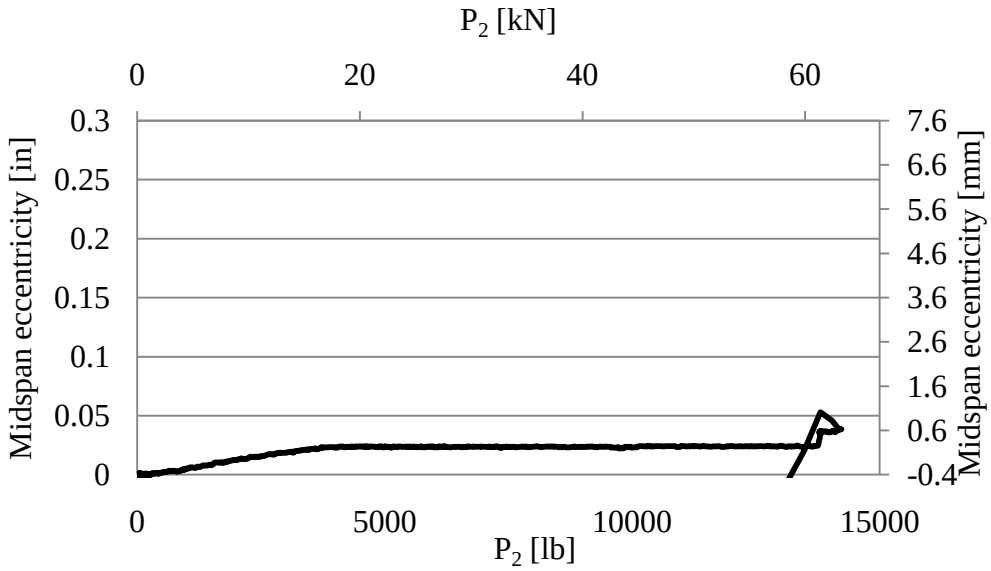

FIGURE 5-17: Midspan deflection vs. P_2 for GCC-4-BC2.

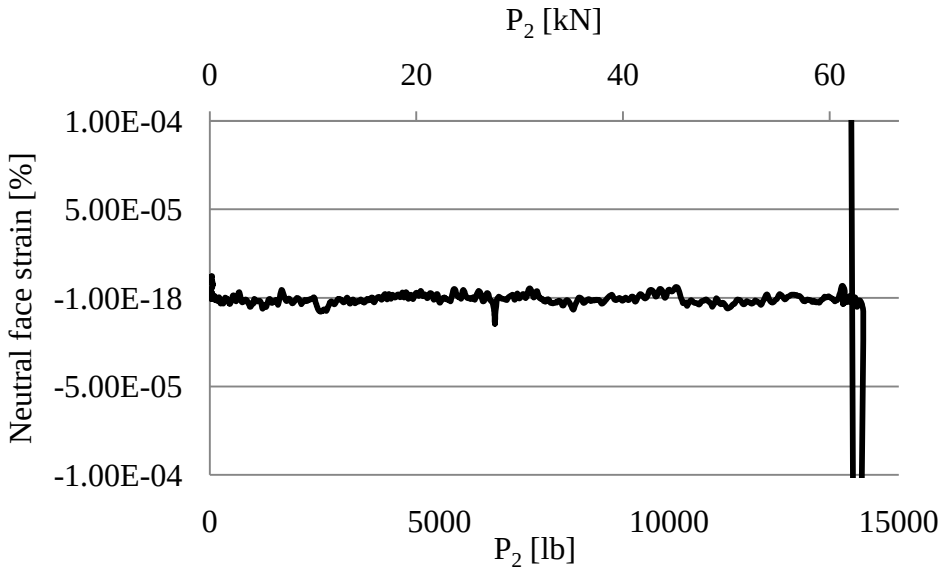

FIGURE 5-18: Neutral face strain vs. P_2 for GCC-4-BC2.

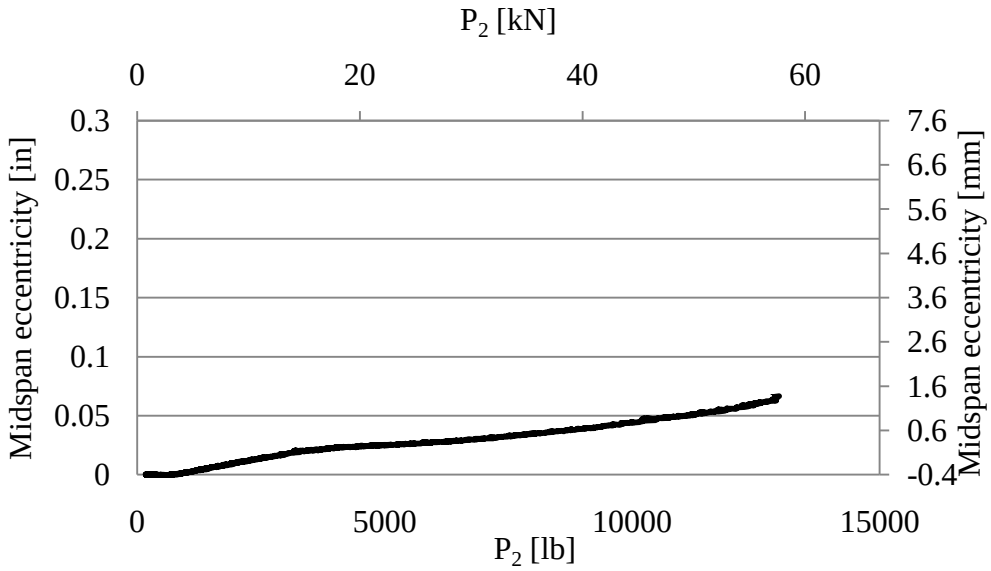

FIGURE 5-19: Midspan deflection vs. P_2 for GCC-5-BC3.

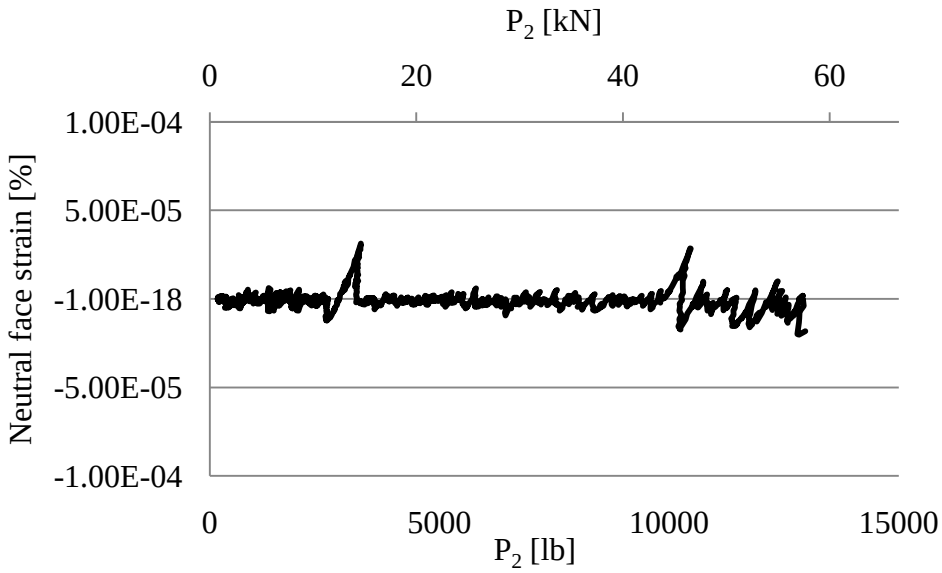

FIGURE 5-20: Neutral face strain vs. P_2 for GCC-5-BC3.

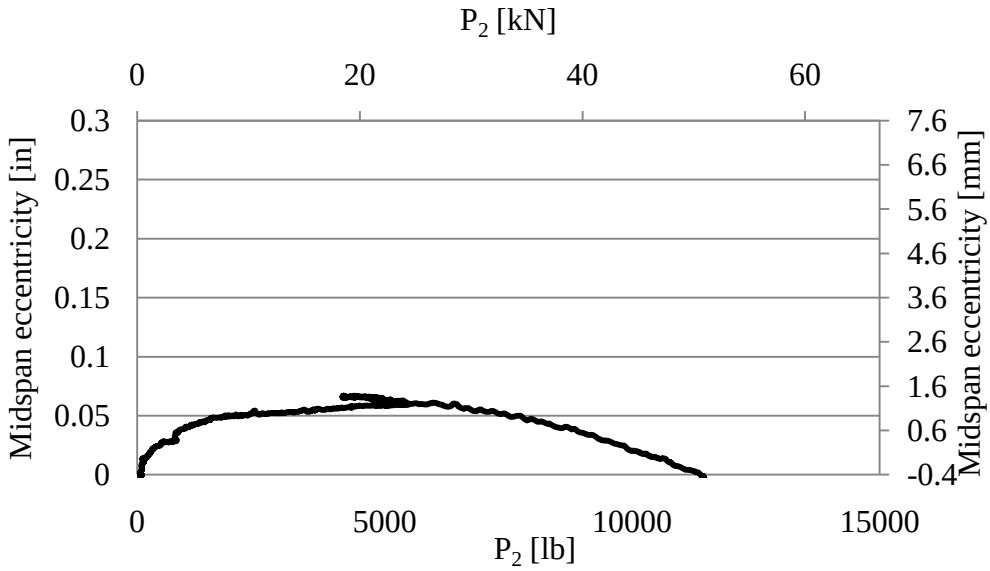

FIGURE 5-21: Midspan deflection vs. P_2 for GCC-6-BC4.

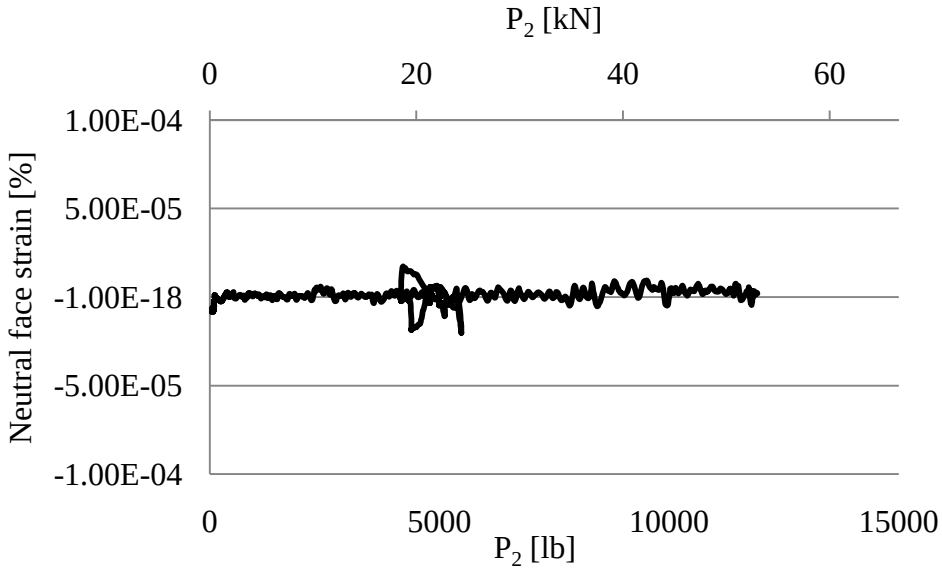

FIGURE 5-22: Neutral face strain vs. P_2 for GCC-6-BC4.

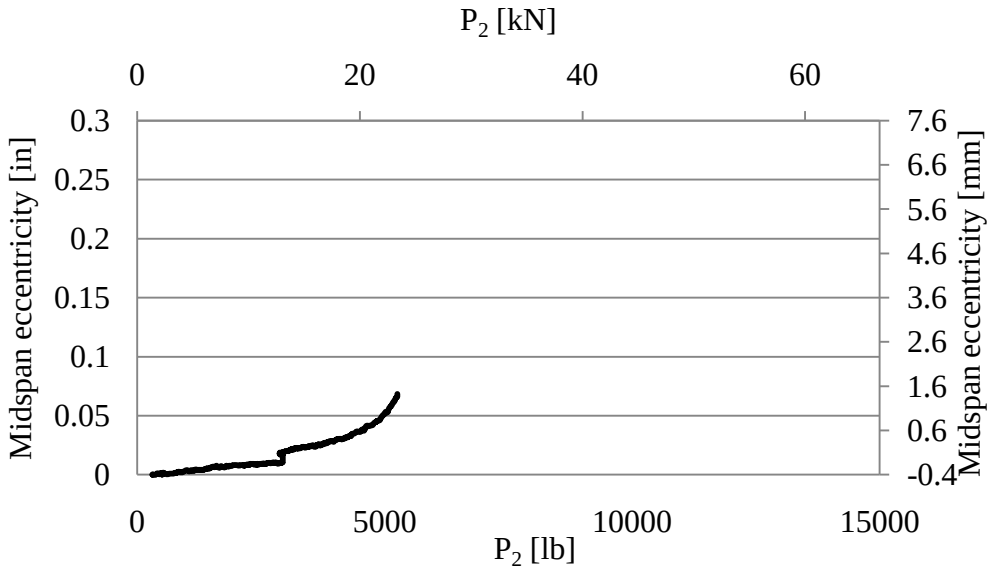

FIGURE 5-23: Midspan deflection vs. P_2 for GCC-7-BC5.

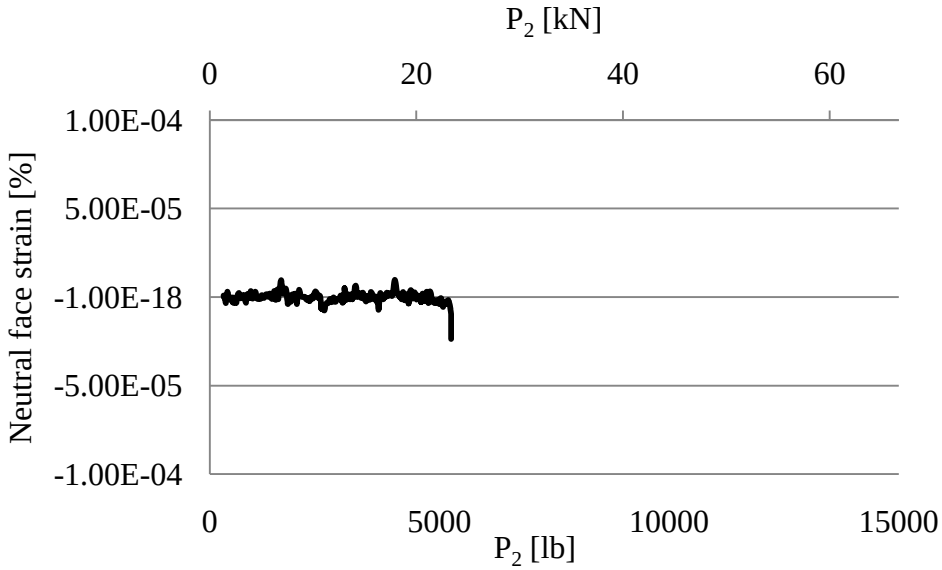

FIGURE 5-24: Neutral face strain vs. P_2 for GCC-7-BC5.

Failure of the beam columns was initiated by crushing on the compressive face of the specimen. As the depth of crushing became greater, it was not possible to control the decrease in P_2 to maintain the neutrality of the beam-column face opposite of the crushing face. Therefore, later stages of failure usually included some form of tension

cracking. FIGURE 5-25 through 5-29 illustrate the failure modes of each of the five beam-column specimens.

FIGURE 5-25: Failure of GCC-3-BC1.

FIGURE 5-26: Failure of GCC-3-BC2.

FIGURE 5-27: Failure of GCC-5-BC3.

FIGURE 5-28: Failure of GCC-6-BC4.

FIGURE 5-29: Failure of GCC-7-BC5.

The stress in the concrete, f_c, was computed numerically using both m_0 from Equation (5-12) and f_0 from Equation (5-7). These two calculation methods resulted in slightly different values for f_c, as seen in FIGURE 5-30. Therefore, an average value was used as the final result as plotted in FIGURE 5-31 through FIGURE 5-35, the results of all five beam-columns.

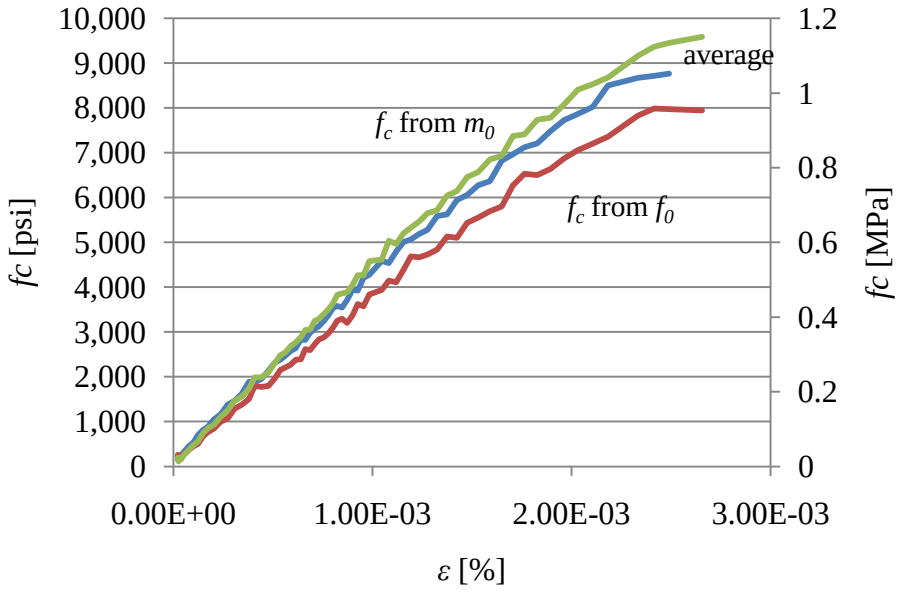

FIGURE 5-30: f_c computed from f_0 and from m_0 and average values.

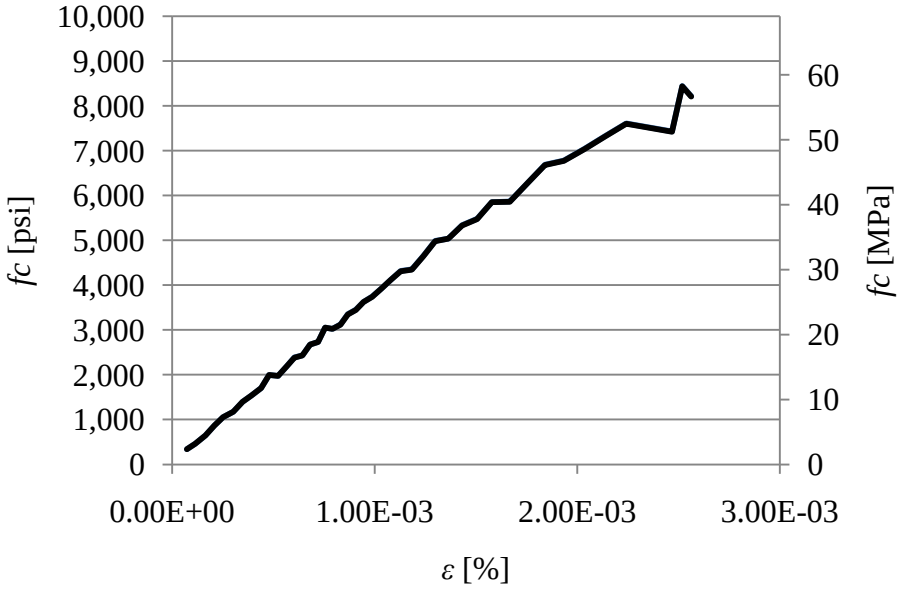

FIGURE 5-31: GCC-3-BC1 stress-strain relationship from flexural tests.

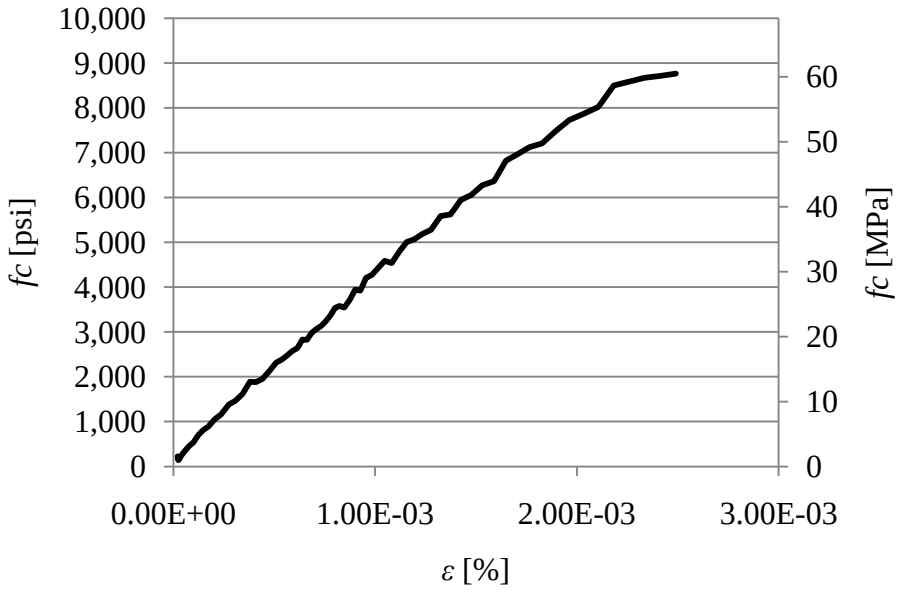

FIGURE 5-32: GCC-4-BC2 stress-strain relationship from flexural tests.

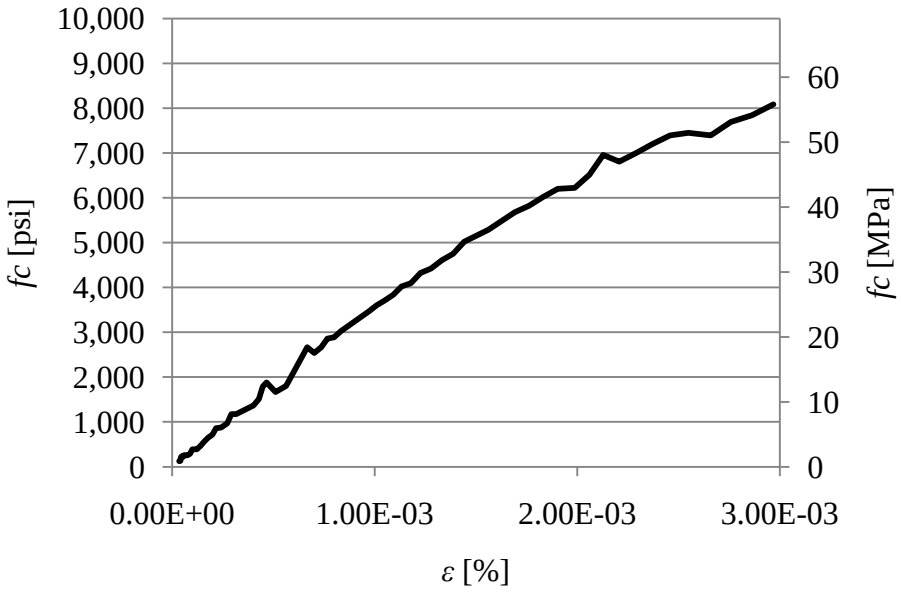

FIGURE 5-33: GCC-5-BC3 stress-strain relationship from flexural tests.

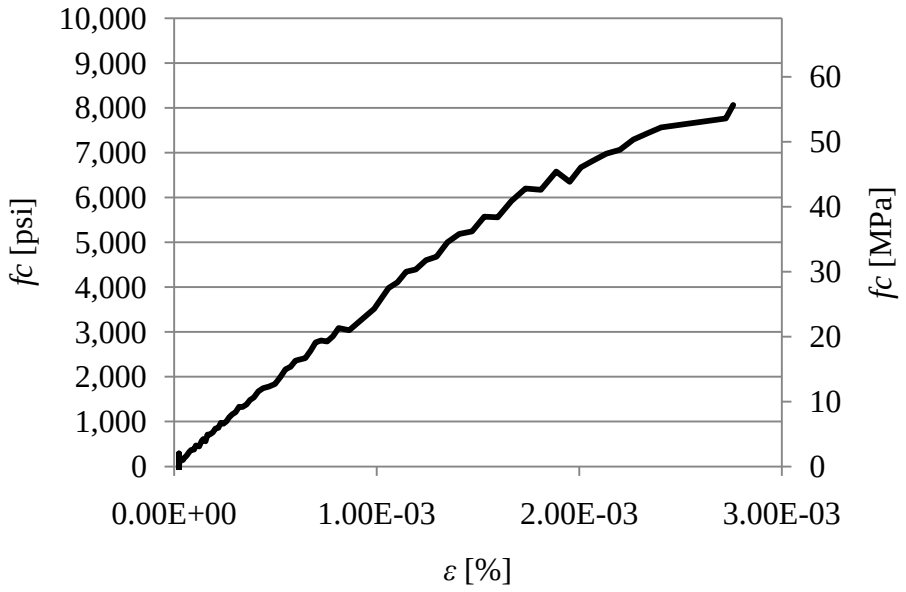

FIGURE 5-34: GCC-6-BC4 stress-strain relationship from flexural tests.

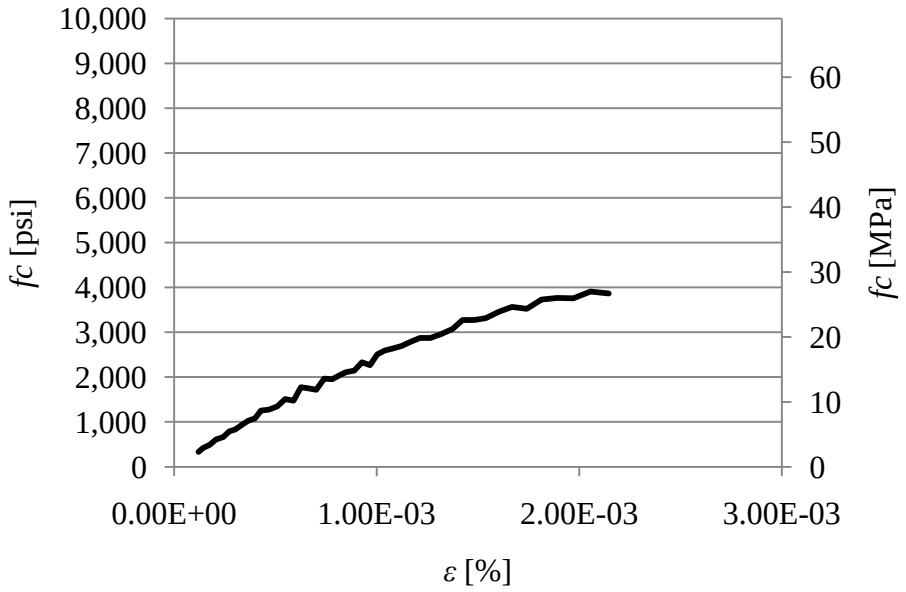

FIGURE 5-35: GCC-7-BC5 stress-strain relationship from flexural tests.

5.3.2 Discussion of beam column results

The five beam-columns provided a spectrum of stress-strain response that appears to be related to concrete compressive strength. As is apparent in FIGURE 5-36, the slope of the stress strain curve increases as the concrete compressive strength increases. TABLE 5-2 also shows this relationship and provides a comparison with the slope of each curve between zero strain and 0.001% strain and the estimated modulus of elasticity for each concrete compressive strength using Equations (2-9) and (2-10). These formulas verify the linear portion of the results curves by accurately predicting the slope within 5%.

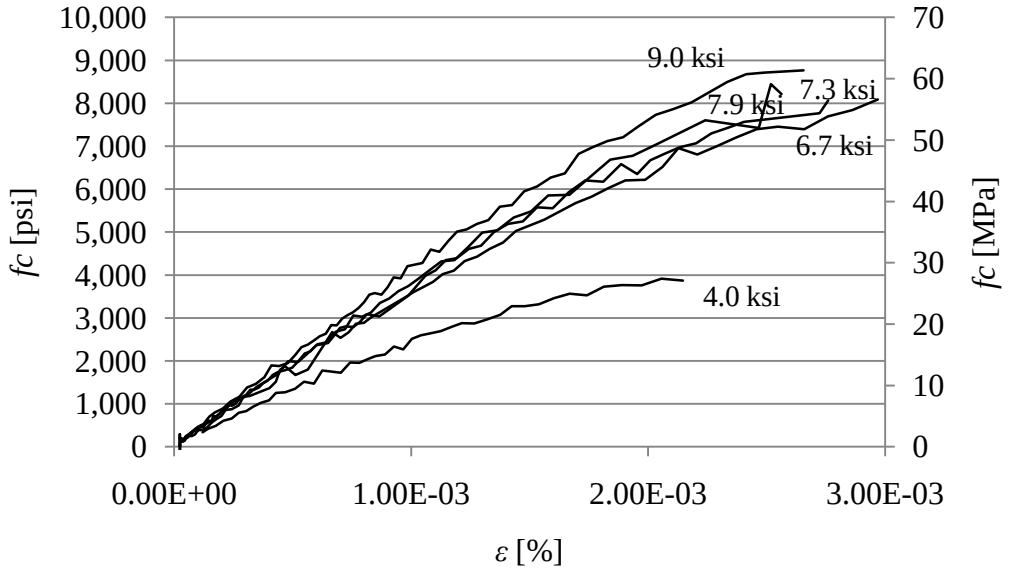

FIGURE 5-36: Relative slopes of stress strain curves.

TABLE 5-2: Slope of stress-strain curves versus estimated modulus of elasticity, psi (GPa).

Specimen	f'_c, psi (MPa)	Estimated E psi (Gpa)	Slope of Stress-Strain curve	% Difference
GCC-3-BC1	7,900 (54)	3.66×10^6 (25.26)	3.82×10^6 (26.33)	4%
GCC-4-BC2	9,000 (62)	3.91×10^6 (26.96)	4.13×10^6 (28.48)	5%
GCC-5-BC3	6,700 (46)	3.37×10^6 (23.27)	3.54×10^6 (24.44)	5%
GCC-6-BC-4	7,300 (50)	3.52×10^6 (24.28)	3.76×10^6 (25.94)	6%
GCC-7-BC-5	4,000 (28)	2.61×10^6 (17.98)	2.48×10^6 (17.13)	-5%

5.3.3 Analysis of beam-column test data

Equations (5-2) and (5-4) allow the computation of k_1k_3 and k_2, respectively. The data presented in the FIGURES above was used to compute these values and is presented in TABLE 5-3. k_3 was found as the ratio of f'_c to the maximum concrete stress f_c determined during the test.

TABLE 5-3: Calculated values of k_1k_3, k_2 and k_3 for beam columns.

Beam-Column	f'_c, psi (MPa)	k_1k_3	k_2	k_3	α_1	β_1
GCC-3-BC1	7,900 (45)	0.513	0.228	1.03	1.13	0.46
GCC-4-BC2	9,000 (62)	0.519	0.231	0.98	1.12	0.46
GCC-5-BC3	6,700 (46)	0.644	0.240	1.21	1.34	0.48
GCC-6-BC4	7,300 (50)	0.593	0.275	1.10	1.08	0.55
GCC-7-BC5	4,000 (28)	0.539	0.266	0.97	1.01	0.53

In order to use these values for practical design purposes, the quantities α_1 and β_1 are used to define a rectangular area that has the same volume as the parabolic shape depicted in FIGURE 5-37. Based on the relationships in FIGURE 5-37, α_1 and β_1 were computed using Equations (5-13) and (5-14) and are presented in TABLE 5-3.

$$\alpha_1 = \frac{k_1 k_3}{2k_2} \quad (5\text{-}13)$$

$$\beta_1 = 2k_2 \quad (5\text{-}14)$$

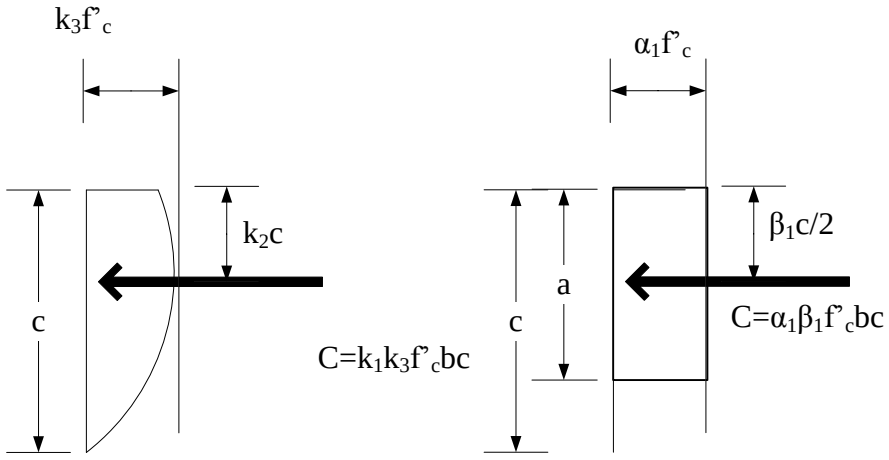

FIGURE 5-37: Relationship between k_1,k_2, k_3 and α_1 and β_1.

The relationship of α_1 and β_1 to the cylinder compressive strength of the concrete in the beam-columns is shown in FIGURE 5-38 and FIGURE 5-39. For α_1 there is a trend towards increasing α_1 with increasing cylinder strength. This implies that the maximum stress attained by concrete in the column was greater than the maximum stress attained by concrete in cylinder tests. As the concrete became stronger, the ratio of cylinder strength to element strength increases. In PCC structural elements, this phenomenon is often related to the altered proportion of mortar and aggregate found in concrete before and after vibratory consolidation. The consolidation process causes lighter, fluid constituents of the fresh concrete to rise towards the upper surface of the element, while aggregate and less mobile constituents remain on the bottom. Such segregation could have occurred in the beam-column elements tested here. Unlike PCC, these beam-columns were cured under elevated temperatures. Fans inside the curing

chamber vigorously circulate the heated air, however it remains possible that a temperature stratification could have developed. In this case, the cylinders, which were placed on the bottom of the oven during curing, may have achieved lower temperatures than the beam-columns, which extended higher into the oven.

All α_1 were in the range of 1.0, with an upper bound of 1.33 and a lower bound of 1.02. For design purposes it is proposed that α_1 be taken as 1.0, which provides conservative estimates of the concrete strength in the concrete element. Although FIGURE 5-38 indicates that α_1 varies with concrete strength, the variation is not pronounced. There is not sufficient data to justify proposing a design value of α_1 based on the cylinder compressive strength until further research can illuminate the causes of this difference.

β_1 also shows a tendency to be reduced slightly as cylinder compressive strength increases. For normal strength PCC, ACI 318 provides a range of β_1 =0.85 for concrete between 2,500 and 4,000 psi (17-28 MPa) to β_1 =0.65 for concrete above 8,000 psi [55 MPa]. The beam-columns tested here ranged in strength from 4,000 to 9,000 psi [28-62 MPa], however the range of β_1 values was not nearly as broad. For the GCC beam-columns, β_1 values ranged from 0.54 for the 4,000 psi [28 MPa] concrete to 0.46 for the higher strength concrete. Although this seems to imply that the depth of the stress block should become smaller with increasing concrete compressive strength, there is not sufficient resolution in the data to justify creating a variable β_1. The average value of β_1=0.5 can be used for design purposes.

When plotted, the data point representing GCC-5-BC3 appears to be an outlier. This column achieved much higher compressive stress in the flexural specimen than was

expected considering the cylinder tests. These results show α_1 and β_1 that are higher than the rest of the specimens.

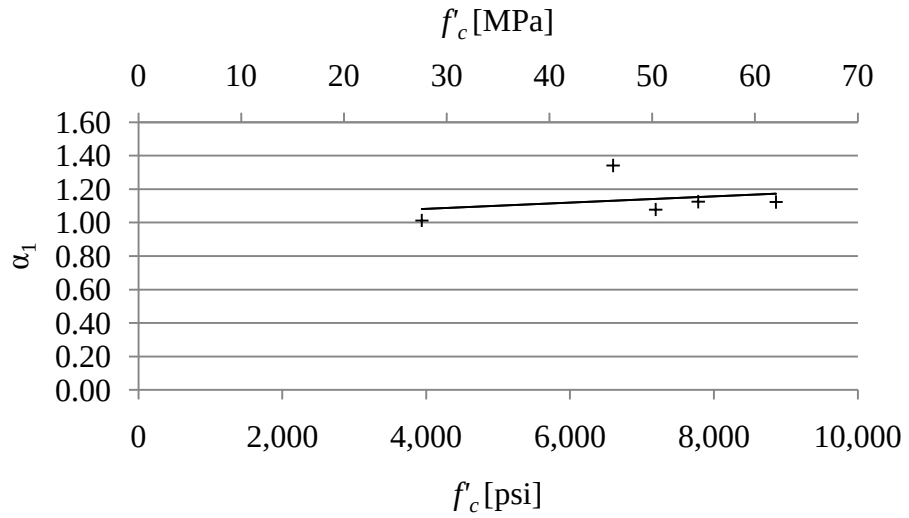

FIGURE 5-38: α_1 related to cylinder compressive strength for beam-columns.

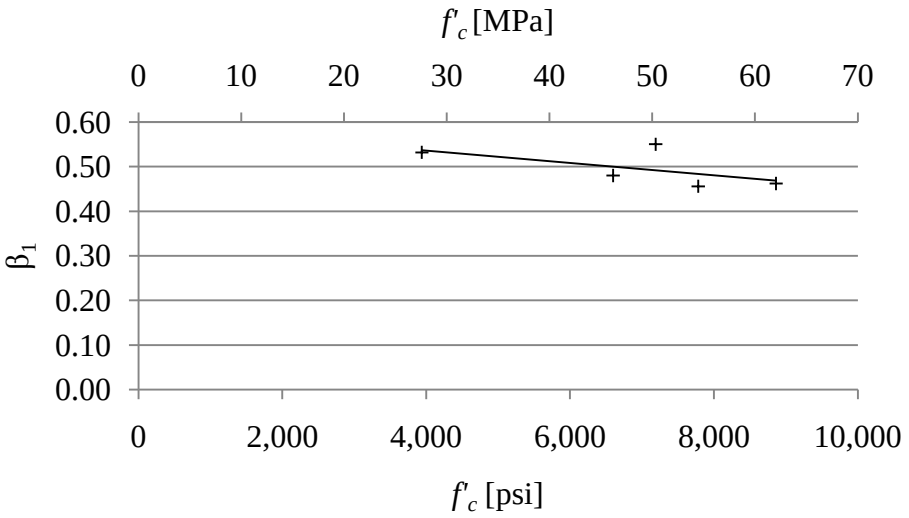

FIGURE 5-39: β_1 related to cylinder compressive strength for beam-columns.

The values for α_1 and β_1 indicate that an equivalent rectangular stress block for GCC materials is significantly smaller than similar blocks representing Portland cement concrete behavior. The factor k_1 describes the ratio of the area defined by the parabolic

stress distribution shown in FIGURE 5-37 to the area of a rectangle fitted around its border. For a triangular distribution, the appropriate factor would be 0.5, meaning that the triangle occupies half the area of the rectangle. Similarly, for parabolic distributions the appropriate factor is 0.67. The k_1 for the GCC materials was 0.54, indicating that the distribution was very nearly triangular.

The factor k_2 describes the depth of the resultant force, C (defined in FIGURE 5-37), from the extreme compressive fiber. The average computed value for k_2 found here was 0.25, which indicates a more strongly linear portion to the lower-strain portions followed by a plateau near the upper strain regions of the stress-strain relationship. This is apparent from the plots shown in FIGURE 5-31 through FIGURE 5-35.

These conclusions presuppose that the entire range of stress-strain behavior for the GCC beam-columns was captures during the test. PCC materials would be expected to exhibit a descending branch of the stress-strain relationship. The GCC beam columns did not produce this descending branch, but there is not sufficient data to conclude whether the test was not capable of measuring it, or whether GCC materials do not undergo strain softening.

5.3.4 Generalized stress-strain relationship for gcc

The stress strain profiles given in FIGURE 5-31 through FIGURE 5-35 are only directly applicable to concrete having similar composition and compressive strength as the concretes that were tested in these experiments. However, there is a trend of increasing slope with increasing compressive strength. Therefore, it may be possible to relate the shape of the stress-strain profile with a generalized, continuous function whose slope is defined by the compressive strength of the material.

The basic contour of the stress-strain profiles that of a very shallow parabola. The model function given in Equation (5-15) was used as an input to a curve-fitting routine in MathCAD to determine the parameters *a* and *b* for each of the profiles in FIGURE 5-31 through FIGURE 5-35. The basic form of the equation is a power function. The slope of the function can be increased or reduced with the parameter *a*, and the degree of curvature is fixed by adjusting parameter *b*. The curve fitting routine returned the values in TABLE 5-4. These values were further parameterized with the relationships shown in FIGURE 5-40 and FIGURE 5-41.

$$f_c = a\varepsilon_c^b \tag{5-15}$$

TABLE 5-4: Parameters a and b for GCC stress-strain relationship

f_c' ksi	*a*	*b*
8.7	2.45	0.26
7.9	2.74	0.26
7.3	3.83	0.38
6.7	4.89	0.36
4.0	4.10	1.07

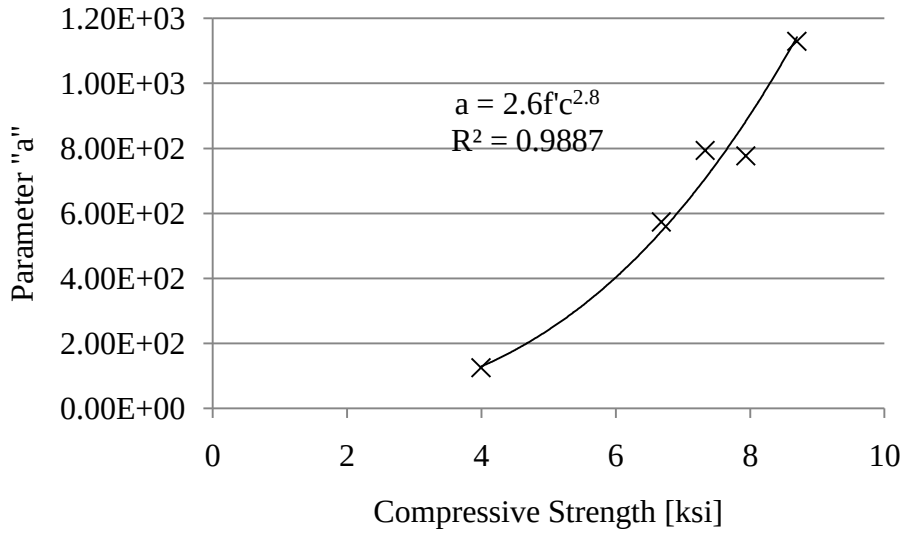

FIGURE 5-40: Formula to determine parameter *a* based on compressive strength.

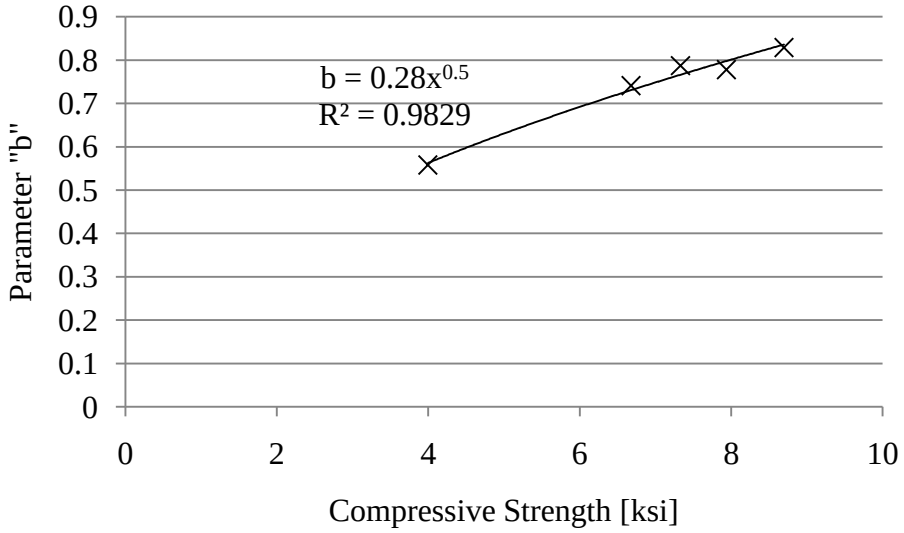

FIGURE 5-41: Formula to determine parameter "b" based on compressive strength

The proposed relationship between stress and strain of GCC is given as Equation (5-15) with the parameters *a* and *b* defined in Equations (5-16) and (5-17). Its ability to approximate the performance of the concretes tested in this study is presented graphically

in FIGURE 5-42 through FIGURE 5-46. The correlation coefficients for Equation (5-15) with each of the experimentally derived relationships are given in TABLE 5-5.

$$a = 2.6{f_c'}^{2.8} \quad (5\text{-}16)$$

$$b = 0.28\sqrt{f_c'} \quad (5\text{-}17)$$

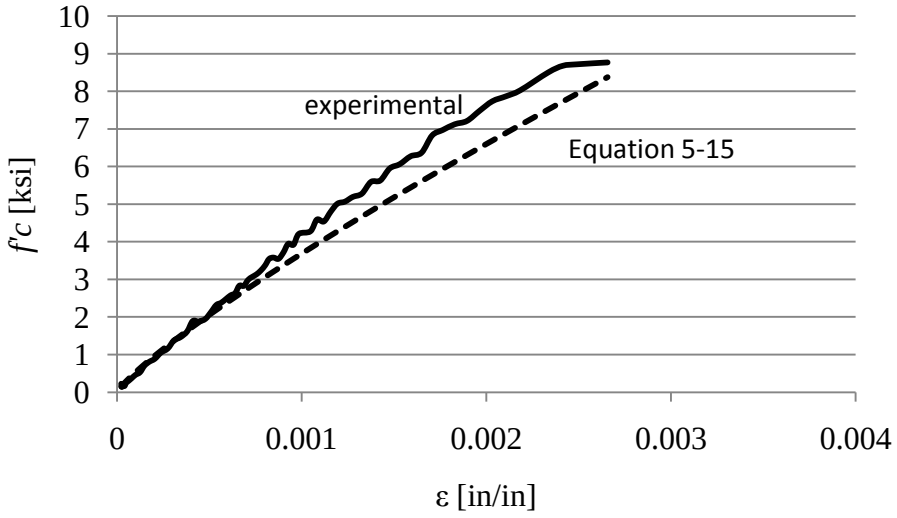

FIGURE 5-42. Experimental results and Equation 5-15 for 9.0 ksi concrete.

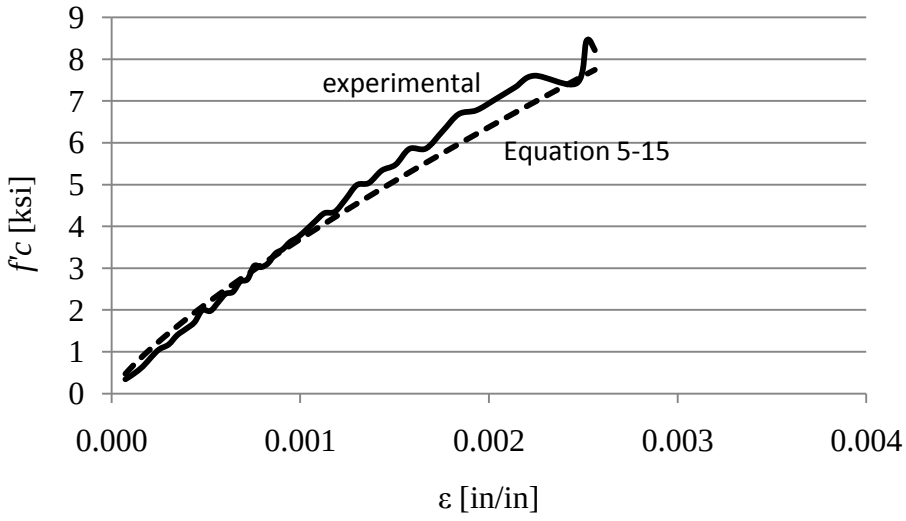

FIGURE 5-43: Experimental results and Equation 5-15 for 7.9 ksi concrete.

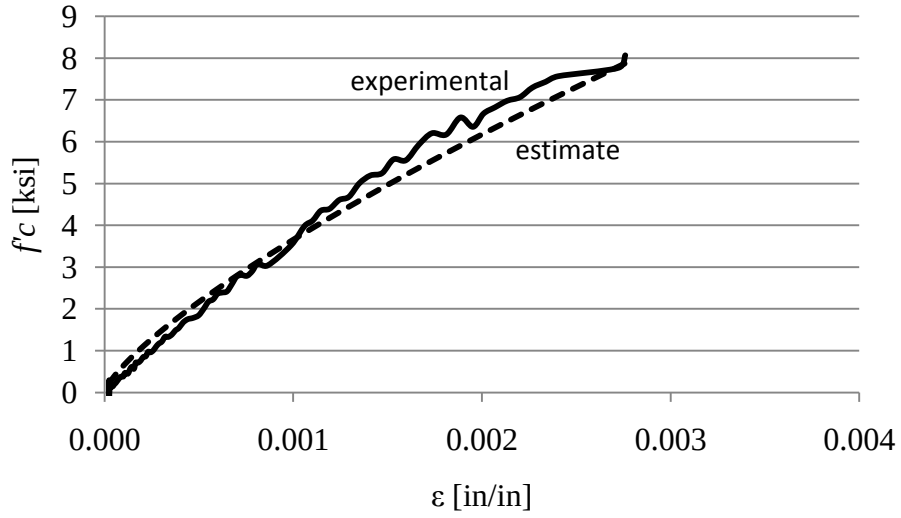

FIGURE 5-44. Experimental results and Equation 5-15 for 7.3 ksi concrete.

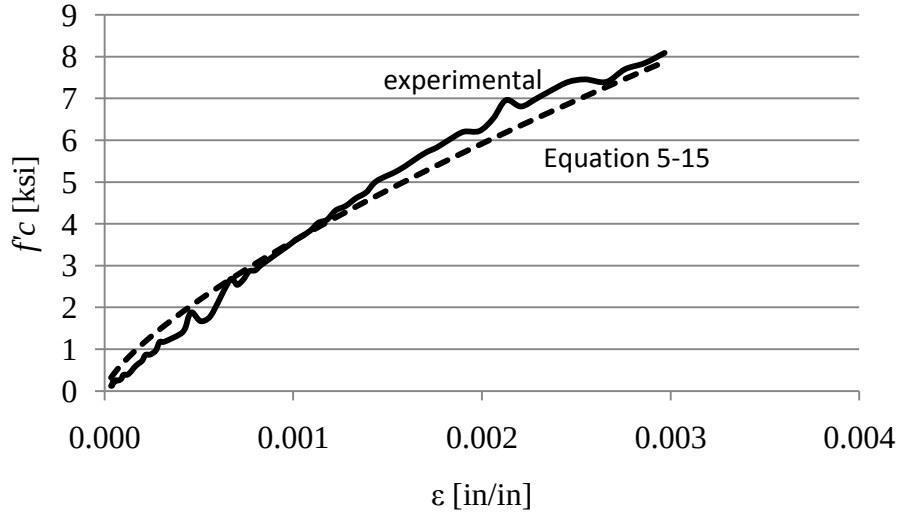

FIGURE 5-45: Experimental results and Equation 5-15 for 6.7 ksi concrete.

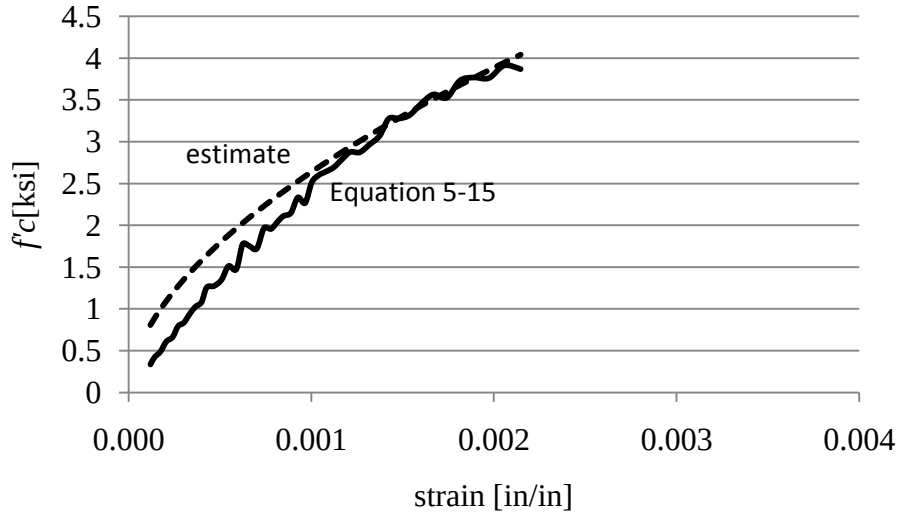

FIGURE 5-46: Experimental results and Equation 5-15 for 4.0 ksi concrete.

TABLE 5-5: Correlation coefficient for concrete stress estimation curves.

Concrete Compressive Strength	Pearsons's Correlation Coefficient
9.0	0.998
7.9	0.998
7.3	0.998
6.7	0.998
4.0	0.997

5.4 Conclusions

The results presented in this section have many qualities that correlate with expected results such as the estimated modulus of elasticity. However, some results indicate that the test procedure may not have successfully measured stress-strain behavior through ultimate strain. This is evidenced by the wide range in terminal strain (rather than ultimate strain, since it is not certain that ultimate strain was reached) values collected across the five tests. These ranged from 0.00215 in specimen GCC-7-BC5 to 0.00297 in

specimen GCC-6-BC4. The terminal strain recorded in the tests was not linked to concrete compressive strength.

Difficulty measuring the ultimate strain could have arisen from several issues related to the specimen construction or the test protocol. The specimens did not fail in the instrumented zone of the beam. This means that when crushing was initiated, the strains local to the instrumented area actually would have reduced due to the declining loads on the specimen and the peak strain would not likely be recorded. Since data is not available in the literature regarding post peak or ultimate strain behavior of GCC materials, more specialized tests are required to ascertain whether the full range of elastic and post elastic response was measured by these tests.

CHAPTER 6: VERIFICATION OF BEAM PERFORMANCE AND DESIGN COMPUTATIONS

In previous chapters of this dissertation, several material properties and design values have been presented for geopolymer cement concrete. A variety of test specimens have been utilized to experimentally determine these material characteristics. In this chapter, the flexural performance of the beams reported in CHAPTER 4 will be used as a check of the applicability of the material characteristics to the design of GCC beams. Two main cross-checking strategies are used for this purpose. In the first pass, the traditional ACI flexural design calculations for mild-steel reinforced concrete beams and prestressed concrete beams are used to compare expected beam capacity with observed beam capacity. The checkpoints in this first method are cracking moment and ultimate load.

In the second pass, a more complex moment-curvature model is used with the material characteristics determined in previous chapters. The moment-curvature method allows the analysis of stresses and strains in the beams at points prior the beam reaching ultimate moment, so a richer set of checkpoints is available for comparison. In this second method, the checkpoints will include midspan deflection at several points prior to beam failure as well as the predicted ultimate moment.

6.1 Moment-curvature models

Most design computations for reinforced concrete flexural components are made at the limit state. This means, they use the assumption that either the concrete is at its

compression failure strain or the steel is at its tension yield strain. This strategy eliminates the more complicated process of predicting the nonlinear response of the materials at points prior to failure. In order to model the full range of beam behavior up to failure, a more complex computation strategy is required. Moment-curvature analysis is one such method for modeling reinforced concrete beam behavior throughout a loading range.

The model assumes that as a moment is applied to a segment of a beam, as in FIGURE 6-1a, strains develop which lead to the deformation of the cross section (FIGURE 6-1b). The strain distribution across the section is linear, as shown in FIGURE 6-1c, even after the concrete is cracked. The linear distribution of strain is experimentally verifiable. The assumed strain can then be related to stresses in the constituent materials via their known elastic and inelastic properties. To create such a model numerically, the cross-section of the concrete beam is divided into many horizontal strips as shown in FIGURE 6-2. Each strip is assumed to have uniform strain over its depth, which is taken as the average of the range of strains found in the continuous cross-section. The constitutive properties of the material in the strip are used to compute stress from the strain, and the area of the strip can be used to determine the force generated at the centroid of each strip, also shown in FIGURE 6-2.

In order to determine the magnitude of the strains in the cross-section, a value is assumed for strain in the extreme compression fiber. Once maximum strain is established, the curvature, φ (FIGURE 6-1b,c), is computed based on maintaining force equilibrium. The moment acting on the section may be computed by summing the moments generated by the force acting in each strip about any convenient point, such as

the top of the beam. Thus, the iterative steps used to prepare the moment curvature response curve are

1. Assume the maximum compressive strain in the cross-section
2. Determine φ to maintain internal force equilibrium
3. Compute the internal moment that corresponds to φ determined in step 2

By considering the range of moments from zero through ultimate that would be imposed on the beam, a plot relating moment and curvature is generated, as shown in FIGURE 6-3. The points A, B, C and D represent important discontinuities in the behavior of the beam. Point "A" corresponds with the initial tension cracking of the concrete. Point "B" marks the initiation of tension steel yielding and point "C" denotes the beginning of crushing in the extreme compression fibers of the concrete. "D" indicates beam failure by rupture of the compression concrete which is generally caused by the compression rebars buckling.

In addition to modeling the distribution of strains and stresses in a beam undergoing loading, the moment curvature analysis technique is also used to model deflections. The moment-curvature relationship shown in FIGURE 6-3 can be mapped directly onto the moment diagram of a beam to produce a plot of the distribution of curvature along the length of the beam, as in FIGURE 6-4. The beams tested in these experiments were simply supported and symmetrically loaded. This indicates that the deflection of the beam at midspan relative to the support is given by

$$\Delta_{cl} = \int \varphi \, \bar{x} dx \qquad (6\text{-}1)$$

which can be solved numerically by summing the moment of area beneath the curve in FIGURE 6-4. For instance, to determine the deflection at point *x* in FIGURE 6-4, the moment of area, $A_1 \bar{x}$, between the support and *x* would be summed by numerical integration.

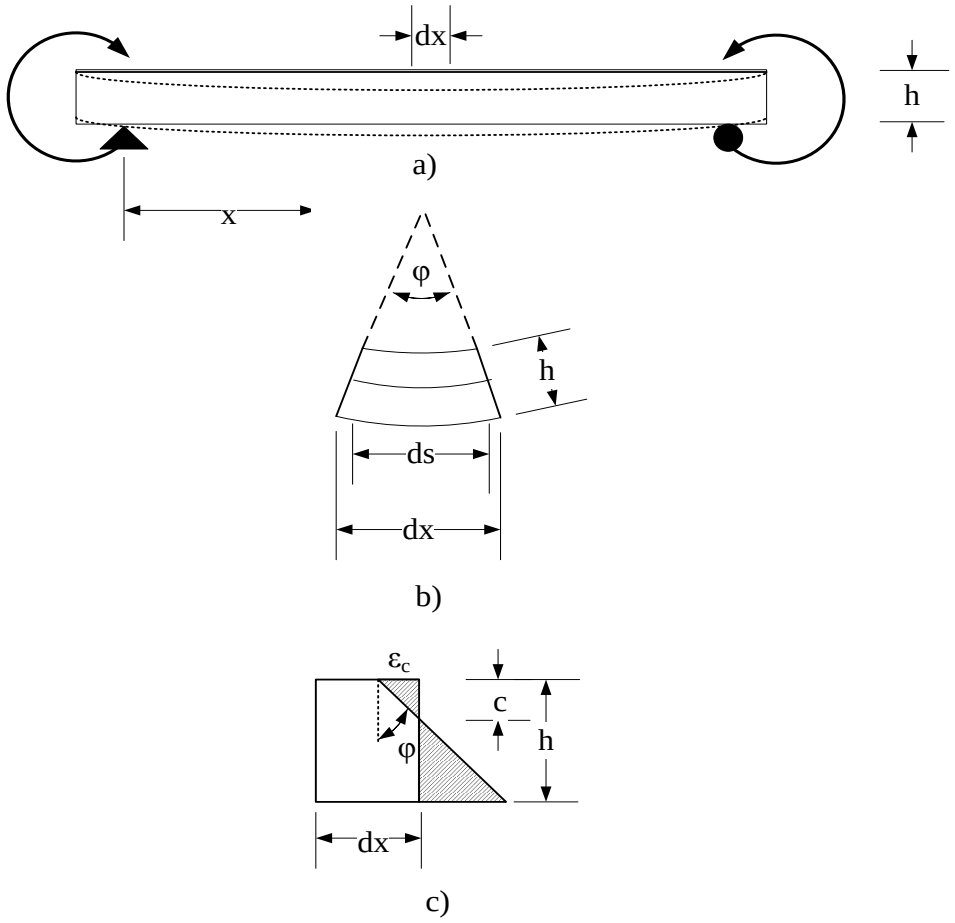

FIGURE 6-1a,b,c. Moment-curvature analysis.

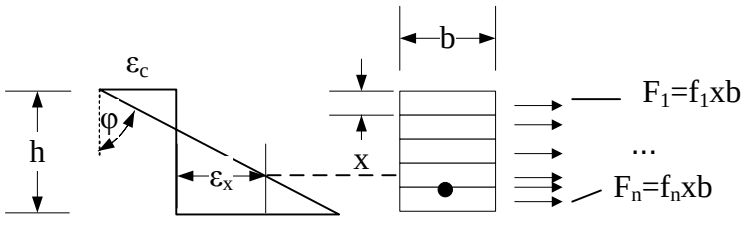

FIGURE 6-2: Distribution of forces in the moment curvature model.

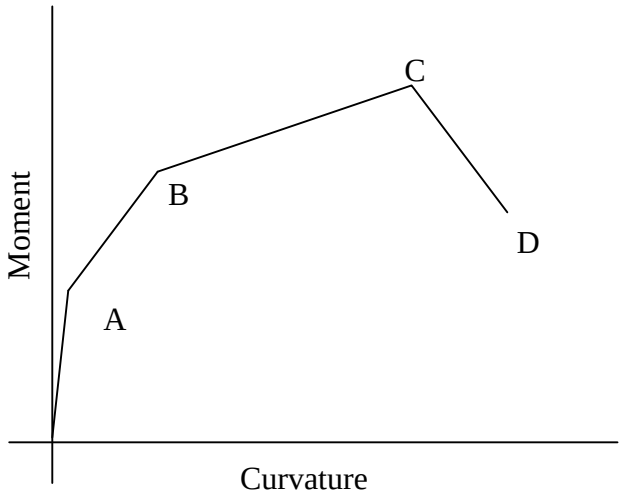

FIGURE 6-3: Moment curvature plot.

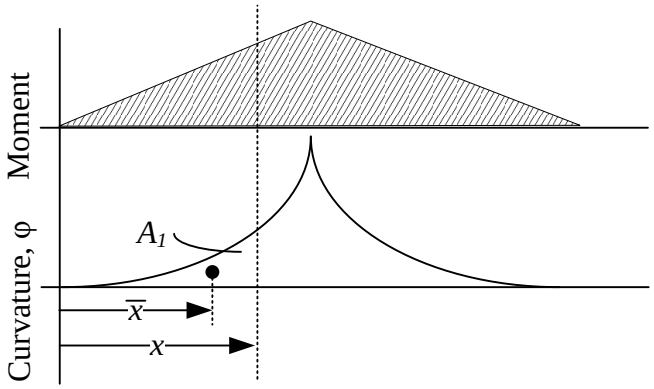

FIGURE 6-4: Moment-curvature relationship plotted along beam length.

Moment curvature models were used in this study to verify the applicability of the concrete stress-strain characteristics measured via the flexural beam-column tests with the component tests of reinforced concrete beams. In the model prepared for this study, the beams were divided into 0.25" (6.4mm) horizontal strips.

6.1.1 Traditional analysis methods

Two points in the load history, "A"- initial cracking of the concrete section, and "C"- initiation of concrete crushing at the compression face of the beam, are important to the design process and are calculated using formulas provided by ACI 318 (American Concrete Institute, 2008). For the purposes of determining the cracking moment, ACI gives

$$M_{cr} = \frac{f_r I_g}{y_t} \tag{6-2}$$

where:

$$I_g = \frac{bh^3}{12} \text{ (for rectangular beams)} \tag{6-3}$$

$$f_r = 7.5\sqrt{f_c'} \text{ [psi]} \tag{6-4}$$

or

$$f_r = 0.62\sqrt{f_c'} \text{ [MPa]} \tag{6-5}$$

For ultimate moment capacity, ACI gives

$$M_n = A_s f_y \left(d - \frac{a}{2}\right) \tag{6-6}$$

where:

A_s: area of steel
f_y: steel yield stress
d: depth of steel in the beam relative to the extreme compression fiber
a: depth of the compressive stress block

Inputs to the ultimate moment calculations are presented in TABLE 6-1. The computed ultimate moment values for the four beams reported here are given in TABLE 6-2. It can be seen that for all the mild steel reinforced beams the design values are very conservative in comparison to the recorded performance. In order to make the

calculations in TABLE 6-2, the actual steel yield stress values determined by tensile tests were used rather than the assumption that grade 60 steel would yield at 60 ksi . Plots of these values are provided in APPENDIX A. Also, stresses in the compression steel were considered. Since the beams were highly underreinforced, the neutral axis was above the top bars and they acted as tensile reinforcement near beam failure.

6.1.1.1 Example calculation method for ultimate moment

Step 1: Determine the depth of the compressive stress block, a

Balancing compressive and tensile forces in the concrete cross section gives

$$\sum f = 0 = -\alpha_1 f_c^{'} ab + A_s^{'} E_s \left(\frac{\varepsilon_c}{\frac{a}{\beta_1}} d - \varepsilon_c \right) + f_y A_s \qquad (6\text{-}7)$$

which can be used to solve for *a* by simplifying and using the quadratic formula. In the case of GCC-1-B1, geometric and material strength quantities In this example, traditional ACI 318 values were used $\alpha_1 = 0.85$ and $\beta_1 = 0.65$. For GCC-1-B1, geometric and material strength quantities are:

d=10.5
$d^{'}$=3
d=10.5" (267mm)
A_s=0.31 in^2 (398mm^2)
$A_s^{'}$=0.31 in^2 (398mm^2)
f_y=54,000 psi (558 MPa)
$f_c^{'}$=11,000 psi (372 MPa)

Solving Equation (6-7), a=1.06" (26.9mm) and $\boldsymbol{\varepsilon_s^{'}}$= 0.00252%. Since this indicates that the top steel has yielded, the depth of the stress block must be recalculated using

$$\sum f = 0 = -\alpha_1 f_c^{'} ab + A_s^{'} f_y + f_y A_s \qquad (6\text{-}8)$$

Solving for a, the depth of the stress block is found to be 1.09" (27.7mm) and ε_s'= 0.00233%.

Step 2: Determine the moment, M_n

Considering that the top steel acts in tension rather than compression, the ultimate moment is computed with

$$M_n = A_s f_y \left(d - \frac{a}{2}\right) + A_s' E_s \varepsilon_s' \left(d' - \frac{a}{2}\right) \quad (6\text{-}9)$$

Therefore, using the section and material qualities for the beam,

$$M_n = A_s f_y \left(d - \frac{a}{2}\right) + A_s' E_s \varepsilon_s' \left(d' - \frac{a}{2}\right)$$

$$M_n = 0.31 \times 55{,}000 \left(10.5 - \frac{1.09}{2}\right) + 0.31 \times 55{,}000 \left(3 - \frac{1.09}{2}\right)$$

$$M_n = 423{,}000\ in - lb$$

$$M_n = 423\ in - kip$$

$$M_n = 47.8\ m - kN$$

The same computation strategy was used for all the mild steel reinforced beams. Input values and calculation points are listed in TABLE 6-1. Results are reported in TABLE 6-2. The cracking moment was computed by estimating the modulus of rupture using ACI methods. Results are presented in TABLE 6-3.

TABLE 6-1: Beam ultimate moment calculation inputs.

Beam		$\alpha_1 = 0.85$ and $\beta_1 = 0.65$		$\alpha_1 = 1.0$ and $\beta_1 = 0.50$	
	f_c' psi (MPa)	a, in (mm)	ε_s'	a, in (mm)	ε_s'
GCC-1-B1	11,000 (75.8)	1.10 (27.9)	0.00233	1.29	0.00049
GCC-2-B2	11,900 (82.0)	1.00 (25.4)	0.00286	0.82	0.00251
PCC-1-B3	12,500 (86.2)	1.00 (25.4)	0.00298	-	-
GCC-R-B4	9,200 (63.4)	1.16 (29.5)	0.00205	0.94	0.00178

TABLE 6-2: Computed and observed values for, M_n.

Beam	M_n (observed)	$\alpha_1 = 0.85$ and $\beta_1 = 0.65$		$\alpha_1 = 1.0$ and $\beta_1 = 0.50$	
		M_n kip-in, (kn-m)	$\frac{M_n\,(observed)}{M_n(calculated)}$	M_n kip-in, (kn-m)	$\frac{M_n\,(observed)}{M_n(calculated)}$
GCC-1-B1	600 (68)	423 (47.8)	1.42	416 (47.0)	1.44
GCC-2-B2	760 (85.9)	567 (64.1)	1.34	566 (63.9)	1.34
PCC-1-B3	670 (75.7)	568 (64.2)	1.18	-	-
GCC-R-B4	682 (77.0)	540 (61.0)	1.26	540 (61.0)	1.25

TABLE 6-3: Computed and observed values for f_r, M_{cr}.

Beam	f_r psi, (MPa)	I_g in^4, (cm^4)	$M_{cr}(calculated)$ k-in, (kN-m)	$M_{cr}\,(observed)$ k-in, (kN-m)
GCC-1-B1	787 (5.4)	1,152 (47,950)	151 (17.1)	160 (18.1)
GCC-2-B2	818 (5.6)	"	157 (17.7)	187 (21.1)
PCC-1-B3	838 (5.8)	"	161 (18.2)	80 (9.0)
GCC-R-B4	719 (5.0)	"	138 (15.6)	144 (16.3)

ACI design formulas conservatively predicted the performance of the GCC beams in all cases. TABLE 6-4 provides the ratios of predicted to observed flexural performance for the four mild-steel reinforced beams. The ultimate moment predictions for the GCC beams were conservative by an average factor of 1.29. This is similar to the same ratio

for the PCC beam of 1.18. For cracking moments, the predictions were very accurate in the case of the GCC beams. Only for the PCC beam were the design formulations unconservative. The first crack appeared in the PCC beam at half the expected load. This could have been caused by damage to the beam during transportation. Since the value is so different from expected, it should be treated as an outlier.

TABLE 6-4: Ratio of observed to predicted cracking moment and ultimate moment.

Beam	$\frac{M_{cr}(calculated)}{M_{cr}\ (observed)}$	$\frac{M_n(calculated)}{M_n\ (observed)}$
GCC-1-B1	1.06	1.42
GCC-2-B2	1.19	1.34
PCC-1-B3	0.50	1.18
GCC-R-B4	1.04	1.26

Similar flexural tests conducted by Sumajouw et al. (2005) resulted in very comparable results. Beams having the same reinforcement ratio, ρ=0.64 defined by

$$\rho = \frac{Area\ of\ concrete}{Area\ of\ tension\ steel} \tag{6-10}$$

displayed the ratios of predicted to observed flexural capacity given in TABLE 6-5. As with the results collected in this study, Sumajouw found that over-estimates are made for beams with very low reinforcement ratios. As the ρ increases, the design formulations result in smaller overestimates.

TABLE 6-5: Ratio of observed and calculated flexural strength as reported by Sumajouw(2006).

f_c' psi (MPa)	ρ	$\frac{M_n\ (observed)}{M_n(calculated)}$
5,531 (37)	0.64	1.24
6,876 (46)	0.64	1.28
11,361 (76)	0.64	1.42

6.2 Flexural performance assessed by moment-curvature models

The moment-curvature model was used to predict the failure load as well as the deflection of the reinforced concrete beams. Inputs to the models were the concrete compressive strength for each beam, the stress-strain curve given by Equation (5-16) and the beam geometry presented in FIGURE 4-3. The model, executed in the spreadsheet application Excel, used the techniques described in Section 6.1.1 to make midspan deflection estimates as well as maximum moment computations. These were compared with the results given in CHAPTER 4.

6.2.1 Ultimate moment

The ultimate moment is defined as the maximum resisting moment achieved by the reinforced concrete beams during the flexural tests. The experimental results of these tests were presented in CHAPTER 4, and are summarized in TABLE 6-6. It can be seen that the moment curvature model provided slightly conservative results for the strength of the beams.

TABLE 6-6: Ultimate moment predictions made with the moment-curvature model.

Beam	$M_n(calculated)$ kip-in (kn-m)	$M_n\ (observed)$ kip-in (kn-m)	$\frac{M_n\ (observed)}{M_n(calculated)}$
GCC-1-B1	494 (55.8)	600 (68)	1.21
GCC-2-B2	615 (69.5)	760 (85.9)	1.24
PCC-1-B3	657 (74.2)	670 (75.7)	1.02
GCC-R-B4	589 (66.5)	682 (77.0)	1.16

6.2.2 Correlation of moment-curvature model results with beam performance

The moment-curvature model was used to predict midspan deflection of the reinforced concrete beams. The predicted and actual deflection is plotted in FIGURE 6-5 through FIGURE 6-8. Based on the changes in slope along the load history displayed in these charts, the model does accurately predict cracking and the onset of reinforcement yielding. However, it loses accuracy in the upper regions of the beam's moment capacity. TABLE 6-6 gives the accuracy of the models in terms of the ratio of actual to predicted deflection.

FIGURES 6-5 through 6-8 also provide model results using a stress-strain relationship sometimes applied to PCC. Due to uncertainty in the results of the flexural beam-column tests, the stress-strain relationship proposed by Popovics and refined for high strength concrete by Mertol was used to model the GCC stress-strain response (Mertol, 2006; Popovics, 1973). This equation is give as

$$f_c = f_c' \frac{\varepsilon_c}{\varepsilon_{co}} \frac{n}{n-1+\left(\frac{\varepsilon_c}{\varepsilon_{co}}\right)^{nk}} \tag{6-11}$$

where

$$n = 0.31f_c^{'} + 0.78 \quad (6\text{-}12)$$
$$k = 0.10f_c^{'} + 1.20 \quad (6\text{-}13)$$
$$\varepsilon_{co} = 0.0035 \quad (6\text{-}14)$$

Since reliable values for ε_{co} were not determined during the flexural beam column tests, this value was taken as 0.0035 for all tests, rather than the variable value proposed by Mertol (2006).

TABLE 6-7: Ratio of predicted and actual deflections for mild steel reinforced beams at different moment levels ($\Delta_{predicted}/\Delta_{observed}$).

Beam	Maximum Moment, kip-in (kN-M)				
	100 (11.3)	200 (22.6)	300 (33.9)	400 (45.2)	500 (56.5)
GCC-1-B1 (GCC)	0.88	1.11	1.11	1.91	1.14
GCC-1-B1 (Popovics)	0.76	0.79	1.03	1.56	1.08
GCC-2-B2 (GCC)	1.15	3.12	1.62	1.37	1.74
GCC-2-B2 (Popovics)	1.04	2.58	1.52	1.25	1.55
PCC-1-B3 (Popovics)	0.41	0.44	0.82	0.84	1.13
GCC-R-B4 (GCC)	0.51	0.75	1.02	1.00	1.45
GCC-R-B4 (Popovics)	0.62	1.04	1.09	1.09	1.51

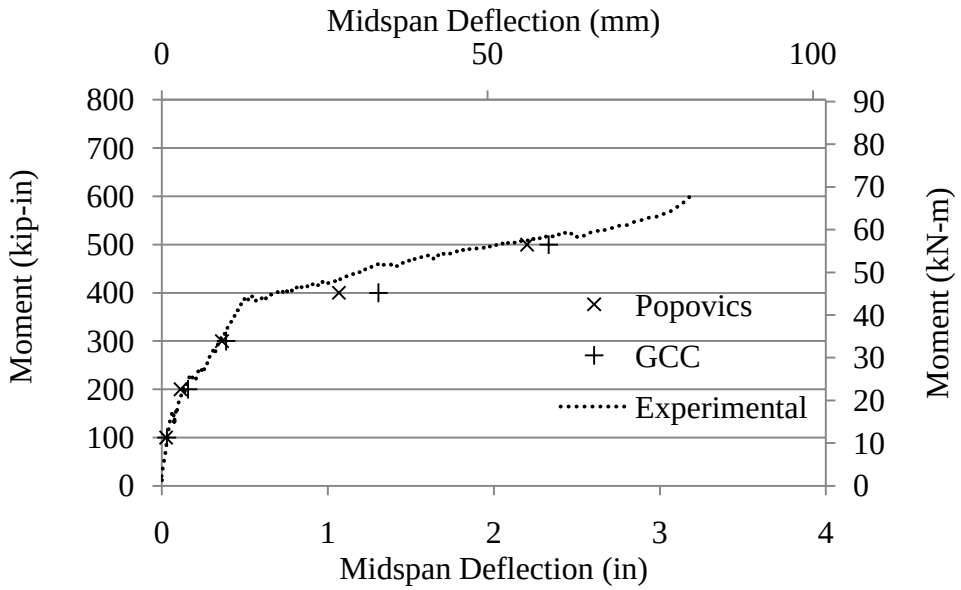

FIGURE 6-5: Modeled and actual deflection for GCC-1-B1.

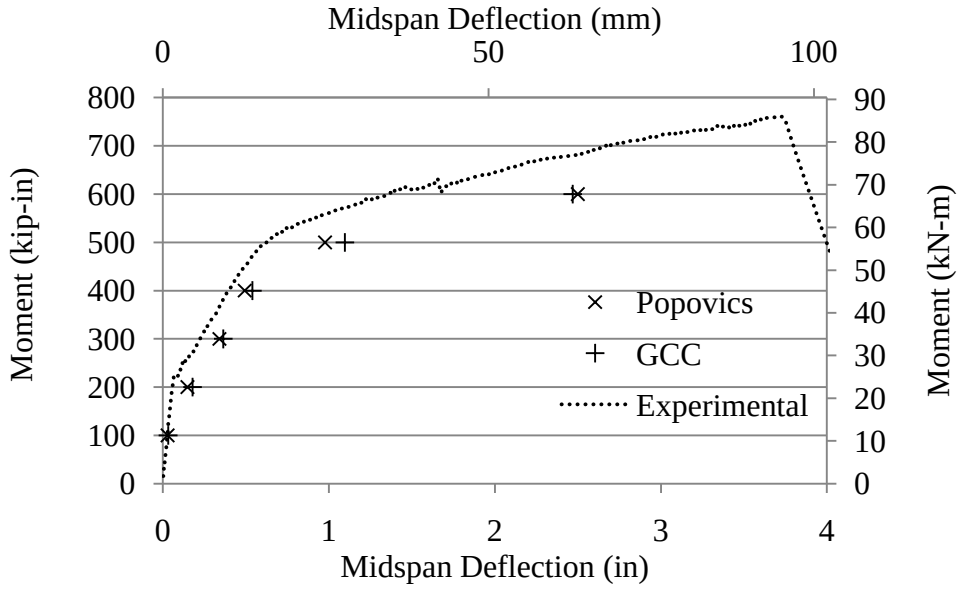

FIGURE 6-6: Modeled and. actual deflection for GCC-2-B2.

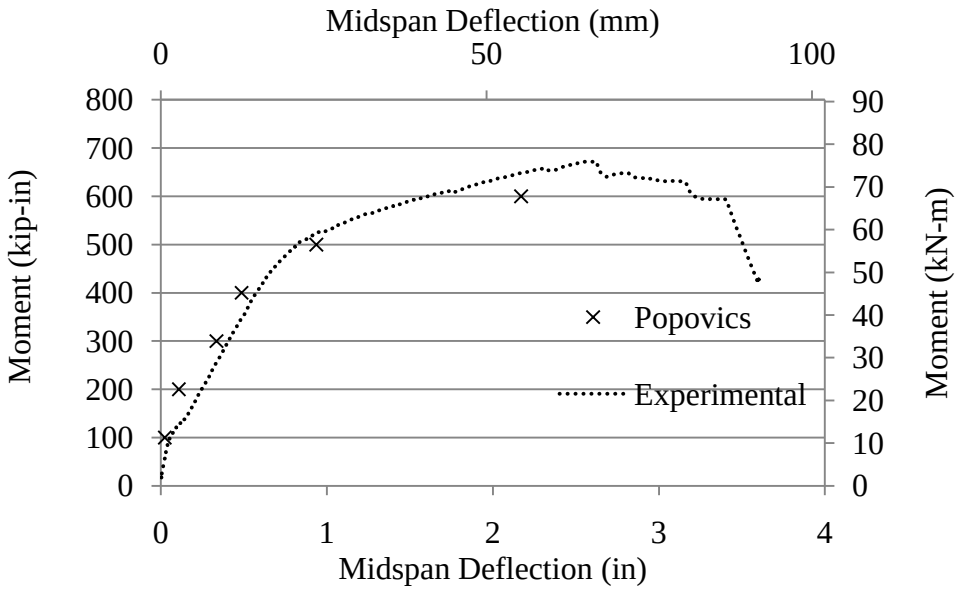

FIGURE 6-7: Modeled and actual deflection for PCC-1-B3.

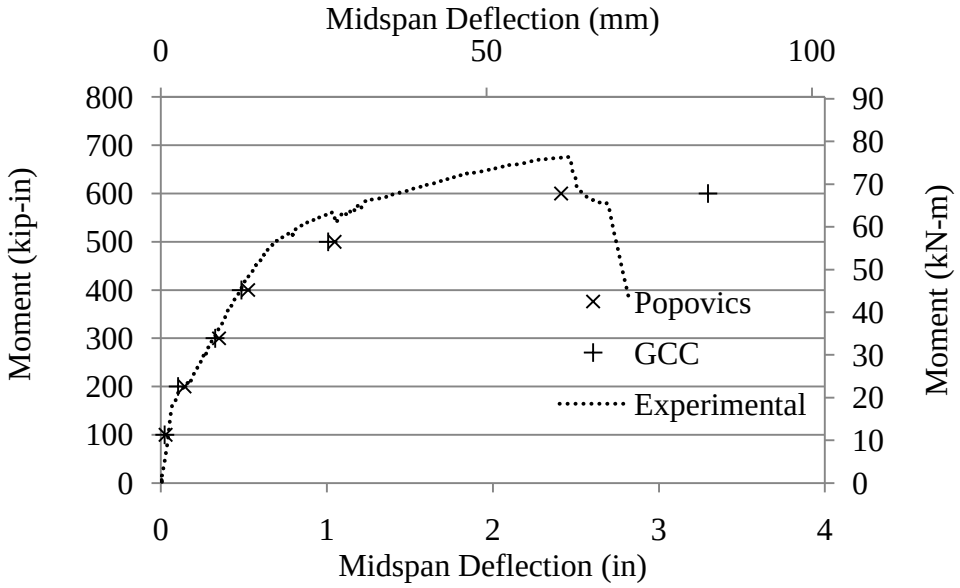

FIGURE 6-8: Modeled and actual deflection for GCC-R-B4.

6.2.3 Discussion of moment-curvature modeling results

Because the concrete beams used in this study were very under-reinforced, the depths of the compression zones in the beam were small. This resulted in the ultimate moment calculations having a high sensitivity to quantities that are not well defined for the GCC, such as ultimate strain and post-peak stress-strain relationships. The results of the deflection-correlation study had less sensitivity to the ultimate and post-peak stress characteristics of the GCC and therefore, provided more reliable results for moment loads less than the ultimate moment. The results in TABLE 6-7 as well as in FIGURE 6-5 through 6-8 show that the moment-curvature models typically predicted larger deflections than were observed during the tests. At service load levels (300 kip-in) the ratio of predicted to observed deflections ranged from 1.02 to 1.62. Although the difference between using Popovic's stress-strain relationship and the one presented in CHAPTER 5 is fairly small, Popovic's relationship produced more accurate models. This is most likely due to its inclusion of post-peak strains.

6.3 Prestressed concrete beams

For the prestressed concrete beams, two points in the load-deflection history were used to verify the applicability of design formulations and material properties to GCC beam components. These were cracking moment M_{cr} and nominal ultimate moment M_n. The ultimate moment was predicted using both existing ACI design values for α_1 and β_1 as well as the special GCC values presented in CHAPTER 5. Shrinkage and creep parameters for GCC were used to estimate the effective prestress at the time of the test. The magnitude of the measured cracking moment was further used to estimate the

accuracy of the calculation. For purposes of making the design calculations presented in this chapter, the geometric quantities given in TABLE 6-8 were used.

TABLE 6-8: Geometric quantities used for prestressed beam analysis.

Quantity	Notation	Value	Units
Beam width	b_w	10	In
Beam length	L	18	Ft
Beam height	h	18	In
Depth to the centroid of the prestressing steel	d_p	14	In
Depth to the mild steel reinforcing	d_s	16.25	in
Moment of inertia	I	4860	in^4
Cross sectional area	a_c	180	in^2
Distance from beam centroid to beam top	y_{top}	9	in
Distance from beam centroid to beam bottom	y_{bot}	9	in
Section modulus for beam bottom	S_{bot}	540	in^3
Section modulus for beam top	S_{top}	540	in^3
Radius of gyration	r^2	27	in^2
Length	l	216	in
Prestressing steel eccentricity	e	5	in

6.3.1 Ultimate moment

The prestressed beams contained both prestressing steel at two depths in the beam as well as mild steel reinforcing at the top and the bottom as shown in FIGURE 4-21. All four of these steel groups were considered as contributing to the ultimate moment capacity of the beam. The depth to the neutral axis was computed by balancing the

forces from each of these reinforcing groups as well as the compressive zone of the concrete. Analysis accounted for increasing strain in the prestressing steel and related the magnitude of the stress to stress-strain test results provided by the manufacturer.

TABLE 6-9 gives the results of the ultimate moment computation using the ACI 318 design guidelines for α_1 and β_1 where

α_1=0.85

β_1=0.65

Also in TABLE 6-9 are the results of the same computation using the updated design quantities developed in CHAPTER 5:. These were given as

α_1=1.0

β_1=0.5

TABLE 6-9: Computed ultimate moment values, kip-in.

Beam	$M_n\ (observed)$	ACI 318 α_1 and β_1	$\frac{M_n\ (observed)}{M_n(calculated)}$	Updated α_1 and β_1	$\frac{M_n\ (observed)}{M_n(calculated)}$
GCC-2-P1	3,125	3,255	0.96	3,126	1.00
PCC-1-P2	3,112	3,350	0.93	-	-
GCC-R-P3	3,124	2,805	1.11	2,988	1.05

The ratio of experimental to calculated results shows a very good ability to predict the ultimate moment for GCC prestressed flexural beams. Using the α_1 and β_1 values proposed in CHAPTER 5, calculations are slightly more accurate than when using values proposed for general Portland cement concrete design. It is important to note that using the ACI values provides a risk of over-estimating the flexural strength, as seen in the case of GCC-1. However, the ACI values also over estimated the strength of the PCC beam.

6.3.2 Creep and shrinkage

Long term creep and shrinkage tests were performed on all three concretes used in this study. In order to verify the results of these tests, presented in CHAPTER 3, they were applied to a prestressed concrete design problem that was verified experimentally. The creep and shrinkage values were used to estimate prestress losses in three prestressed concrete beams. The cracking moment observed during flexural testing was compared with the cracking moment computed using the effective prestress.

For the calculation, losses from elastic shortening, creep and shrinkage were considered. Steel relaxation was not considered because its magnitude for the stress levels in the steel and the duration of the load would be negligible. Also of note, the initial prestress was measured with a pressure transducer attached to the prestressing jack. For GCC-R-P1, individual load cells were placed under each strand-chuck in order to verify that the tension remaining after the chucks seated was at the intended level. By using the individual load cells, it was determined that each strand lost approximately 30% of its pre-seating load once the jack was removed. Therefore, the initial prestress for beams GCC-2-P1 and PCC-1-P1 has been prorated by 30% prior to the loss calculations presented here. Inputs to the loss calculations are given in TABLE 6-10.

TABLE 6-10: Inputs to prestress loss calculations.

Beam	Initial Prestress, f_{pi}, psi	Age of Beam, days	f_c', psi	E_c, psi	C_t	ε_{sh}
GCC-2-P1	147,700	229	11,900	$41{,}143\sqrt{f_c'}$	0.310	0.000278
PCC-1-P2	147,700	209	12,500	$57{,}000\sqrt{f_c'}$	0.870	0.00060
GCC-R-P3	211,000	30	9,200	$41{,}143\sqrt{f_c'}$	0.184	0.00026

Losses were calculated with the following equations

$$f_{cs} = -\frac{P_i}{A_c}\left(1 + \frac{e^2}{r^2}\right) + \frac{M_D}{I_c}e \tag{6-15}$$

where f_{cs} is the stress at the centroid of the steel and all other quantities are given in the preceding TABLEs.

$$\Delta f_{pES} = n f_{cs} \tag{6-16}$$

where:

$n = \frac{E_s}{E_c}$

Δf_{pES}: change in prestress due to elastic shortening

$$\Delta f_{pCR} = C_t \frac{E_s}{E_c} f_{cs} \tag{6-17}$$

where:

Δf_{pCR}: change in prestress due to creep

$$\Delta f_{pSH} = \varepsilon_{SH} E_s \tag{6-18}$$

where:

Δf_{pSH}: change in prestress due to shrinkage

TABLE 6-11 gives a summary of the calculations related to prestress losses. Computations make use of the equations presented above. M_{cr}, given by

$$M_{cr} = S_{bot}\left(7.5\sqrt{f_c'} + \frac{P_i}{A_c}\left(1 + \frac{c_b e}{r^2}\right)\right) \tag{6-19}$$

and are presented in the last column of TABLE 6-11 using the values for effective prestress presented in the same TABLE. It is compared with the observed cracking moment in TABLE 6-12. This test involves the interaction of the multiple variables: concrete strength, creep coefficient and shrinkage coefficient. However the results

indicate a fairly good correlation of calculated values and experimentally determined values. The largest calculated losses were a result of shrinkage, followed by elastic shortening. The strains due to creep were very nearly negligible in comparison.

TABLE 6-11: Prestress loss calculations, psi (MPa).

	f_{pi}	Δf_{pES}	Δf_{pCR}	Δf_{pSH}	Total losses	f_{pe}	M_{cr} k-in, (kN-m)
GCC-1-P1	147,700 (1,018)	-5,525 (-38)	-1,712 (-12)	-8,006 (-55)	-15,243 (-105)	132,457 (913)	1,077 (121)
PCC-1-P2	147,700 (1,018)	-3,896 (-27)	-3,391 (-23)	-17,280 (-119)	-24567 (-169)	123,134 (849)	1,049 (118)
GCC-R-P3	211,000 (1,455)	-9,269 (-64)	-1,704 (-12)	-7,488 (-52)	-18462 (-127)	192,539 (1328)	1,315 (149)

TABLE 6-12: Observed cracking moment versus calculated cracking moment, k-in (kN-m).

Beam	M_{cr} *Observed*	M_{cr} *Calculated*	M_{cr} *Observed*/M_{cr} *Calculated*
GCC-1-P1	989 (111.7)	1,077 (121.7)	0.92
GCC-R-P3	1,261 (142.5)	1,315 (148.6)	0.96

6.4 Conclusions

Material properties determined from tests of GCC specimens, have been used in conjunction with reinforced concrete design formulas and methods to predict the performance of a series of reinforced and prestressed GCC beams. Overall, there was very good correlation between the predicted and observed results as measured by the deflection predictions, cracking moment predictions and ultimate moment predictions.

In order to verify the applicability of α_1 and β_1 values, ACI 318 design provisions were used to predict the ultimate moment for the mild steel reinforced beams. The

average ratio of predicted to observed performance was 1.34. This indicates that the design provisions are slightly conservative. However, since the beams were underreinforced, the design calculations are not very sensitive to changes in the value β_1.

The traditional ACI design formulations were also used to analyze the ultimate capacity of the prestressed beams. Since the depth of the compressive stress block *a* for the prestressed beams is deeper, this exercise provided a better assessment of the α_1 and β_1 values proposed in 0. The average ratio of predicted to observed moment capacity was 1.025. This indicates that the existing design formulations for reinforced concrete may be applied to GCC beams when values of α_1 and β_1 modified for geopolymer applications are used.

CHAPTER 7: LIFE CYCLE ANALYSIS OF GEOPOLYMER CEMENT CONCRETE

Geopolymer cement concrete (GCC) can be used to make many of the structural members that are commonly formed from Portland cement concrete (PCC). The Portland cement binder in PCC requires large inputs of energy and natural resources during its manufacture whereas the binder in GCC is sourced from the waste stream and less energy is required to develop its cementitious properties. The GCC and PCC materials are very similar in many aspects aside from the make-up of their binders. A life cycle assessment can be used to compare the lifecycle impacts of each material in order to verify the improved environmental performance of GCC.

7.1 Life cycle assessment for geopolymer cement concrete production

The results of GCC development presented in CHAPTER 3 were used to generate the inputs to a lifecycle model for the production of geopolymer cements. These inputs include the materials and energy that were used to manufacture the mix designs that were presented. The diagrams in FIGURE 7-1 and FIGURE 7-2 depict the inputs to the manufacture of each material. The quantities of the inputs and outputs shown in the FIGUREs are given in the description of each process later in this dissertation.

In order to compare the results of a life cycle analysis for different materials, it is necessary to define a functional unit. This is an especially critical step when comparing radically different systems, such as timber columns versus steel columns. But, since

concrete bound with geopolymer cement can be used in an overwhelmingly similar capacity as precast Portland cement concrete, the functional unit used for this analysis is simply 1.3 yd^3 (1 m^3) of 7,300 psi (50 MPa) concrete. The two materials can be cast into identical shapes that can be expected to offer similar structural performance. Therefore, the LCA comparison that is presented here is solely related to the development of the concrete strength and does not include the energy required for other concreting tasks. The main differences in the two processes relate to the preparation of the cement. In the case of Portland cement, manufacturing energy is applied prior to mixing the concrete. For geopolymer cement, the energy used to develop strength is applied to prepare the activating solution and to heat the concrete after it is mixed and placed. However, the mixing processes, formwork preparation, reinforcing requirements, concrete placement and consolidation practices are very similar. Therefore, the boundaries of the comparison for the two materials are simplified by considering the following stages for each:

Geopolymer Cement Concrete

- Preparation of cementitious material
- High temperature curing

Portland Cement Concrete

- Manufacture of Portland cement

The mixing process and delivery of structural components from the precasting plant to the jobsite is considered to be similar for both materials.

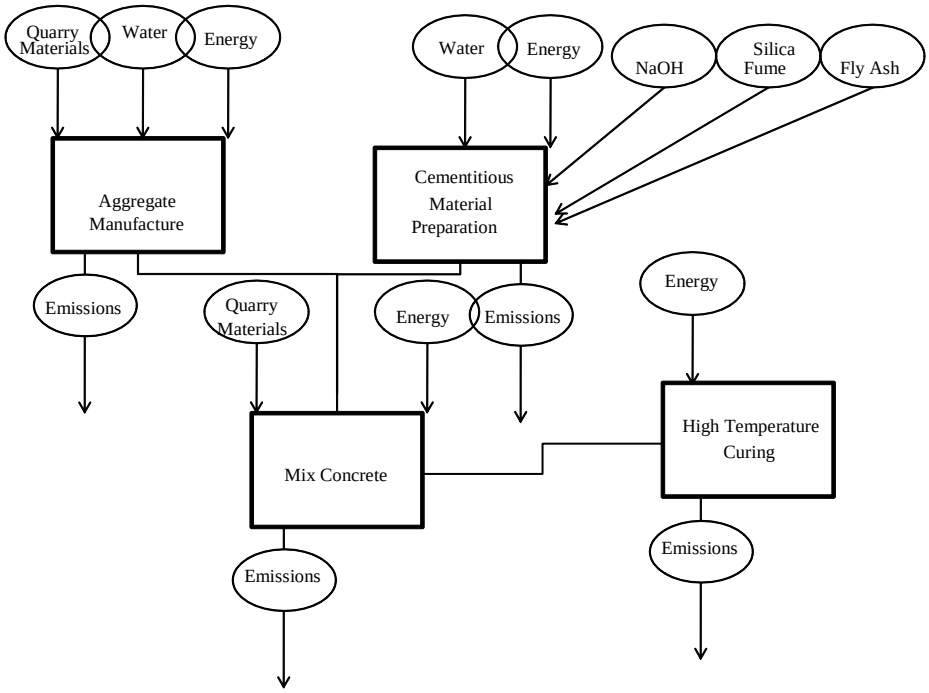

FIGURE 7-1: Manufacture processes for geopolymer cement concrete.

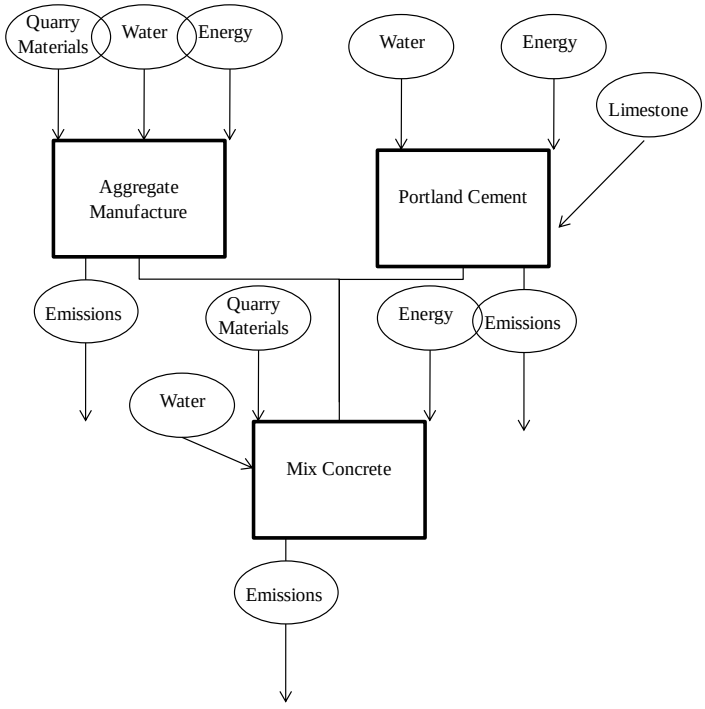

FIGURE 7-2: Manufacture processes for Portland cement concrete.

7.1.1 Energy requirements

The energy necessary to collect fly ash and silica fume used to produce geopolymer was neglected from this study. Because these are both industrial byproducts that must be collected for compliance with air quality regulations, it is customary to neglect their upstream energy requirements. An important energy input to the use of these materials is that for transportation. However, since transportation energy is not considered in the comparison of geopolymer cement concrete with Portland cement concrete production, it is left out of the analysis altogether. Also not considered are the energy requirements for making the concrete admixtures used because their quantities are small enough as to not be significant in the overall analysis.

The ingredients used to manufacture 1.3 yd^3 (1 m^3) of the GCC considered in this analysis are given in TABLE 7-1.

TABLE 7-1: Materials to create 1unit of GCC.

Raw Material	lb/yd^3 (kg/m^3)
Fly Ash	834 (495)
Water	274 (163)
NaOH	83 (49.5)
Silica Fume	62 (37.1)
Fine Aggregate	1336 (793)
Coarse Aggregate	1336 (793)

The processes involved in preparing the cementitious materials for GCC are the following:

1) Manufacture of Alkalinity

NaOH is most commonly produced by electrolysis of brine solution. The reaction produces chlorine gas at the anode and a weak alkali at the cathode. The alkaline solution is typically concentrated to 50% strength for shipment. The SPLINE LCA dataset quantifies the energy required to produce sodium hydroxide as 8,917 BTU/lb (20.74 MJ/kg) (Center for Environmental Assessment of Product and Material Systems, 2008).

2) Production of the activator solution

The method of producing alkaline activator solution for the concretes made in this set of experiments was to mix water, silica fume and the sodium hydroxide together and then to heat the solution overnight. To estimate the energy required for this process only the energy required to maintain an elevated temperature of 167° F (75° C) in a well insulated tank was included. The energy required to heat the solution to 167° F (75° C) was not included because the dissolution of the sodium hydroxide in the water produces temperatures that far exceed 167° F (75°C). The reaction with the silica fume is also quite violent and elevates the temperature further. It was estimated that a well insulated tank will lose heat energy at the rate of 0.194 MJ m^{-2} h^{-1} when the contents are maintained at 167° F (75° C) and the ambient conditions outside the tank are 70° F (21° C). In the lab, small quantities of activator are produced in an oven. However, in an industrial setting it would be produced in a much different manner. In this work, the quantity of activator solution required to produce 1.3 yd^2 (1 m^3) of concrete is about 26 gallons (100 L). A cylindrical 26 gallon (100 L) tank with a height

twice its diameter would have a surface area of 13.5 ft^2 (1.25 m^2). Thus, the energy required to maintain the sodium silicate solution at 167° F (75° C) for 24 hours would be 5,497 BTU (5.8 MJ).

The second process within the boundaries of this LCA is the high temperature curing of the GCC.

3) High Temperature Curing

In the absence of measured quantities, the specific heat of geopolymer concrete was assumed to be similar to that of Portland cement concrete, 0.88 J G^{-1} K^{-1}. Other researchers have determined the specific heat of geopolymer-sand mortars to range between 0.7 and 1.0 J G^{-1} K^{-1} (Geopolymer Institute, 2009). As the bulk of constituents in both materials is aggregate (~80%), this assumption is felt to be reasonably valid. However, properly measuring the specific heat of geopolymer concrete would refine the accuracy of this energy analysis. The heat required to raise the geopolymer concrete from 70 ° F to 167° F (21° C to 75° C) is calculated as 97,436 BTU (102.8 MJ). The concrete must then be held at an elevated temperature for 24-48 hours. As with the activating solution production, heat losses from a well insulated oven wall were estimated at 1,979 BTU ft^{-2} hr^{-1} (0.194 MJ m^{-2} h^{-1}). An oven slightly larger in volume than the concrete would show losses of 2,464 BTU hr^{-1} (2.6 MJ h^{-1}). Longer curing durations will require greater inputs of energy to maintain elevated temperatures for longer periods of time. In total, the energy required to develop the cementitious component of 1.3 yd^2 (1 m^3) of this concrete is estimated at 1,178,137 BTU (1.243 GJ).

7.1.2 Energy required to produce portland cement concrete

The Portland Cement Association (PCA) has published a lifecycle inventory of the energy and material inputs to concrete (Nisbet and Portland Cement, 2007). In this document the Portland cement products ready-mix concrete, precast concrete and concrete masonry units are analyzed. Due to the heating requirements of the geopolymer cement concrete presented in this paper that require it to be produced in a factory setting, it is most directly comparable to a 7,300 psi (50 MPa) precast concrete that is studied in the PCA document. The mix design for this concrete is shown in TABLE 7-2, below.

TABLE 7-2: Mix design for 7,300 psi (50 MPa) concrete.

Raw Material	lb/yd^3 (kg/m^3)
Cement	849 (504)
Water	300 (178)
Coarse Aggregate	1770 (1,050)
Fine Aggregate	(935) 555

In order to compare the energy requirement for manufacturing the two concretes, it is assumed that the primary differences in the production process are in the preparation of the cement and the necessity for elevated curing temperatures in the case of the geopolymer cement concrete. Thus, the other processes such as mixing, transporting, facility lighting and maintenance, etcetera, are similar. The embodied energy of Portland cement averaged over the many production methods is 2,063 BTU/lb (4.798 MJ kg^{-1}) (Marceau et al., 2006). In order to produce the 1,111 lb (504 kg) of cement required for 1.3 yd^3 (1 m^3) of concrete, 2,085,200 BTU (2,200 MJ) of energy would be required.

7.1.3 Comparison of production energy of geopolymer and portland cement concrete

The difference in energy required to produce 50 MPa Portland cement concrete and 7,000 psi (48 MPa) geopolymer cement concrete is 909900 BTU (0.96 GJ) or 44%. TABLE 7-4 lists emissions associated with Portland cement manufacture and NaOH manufacture. The quantities are adjusted for the proportions of each material necessary to mix 1.3 yd^3 (1 m^3) of material having similar compressive strength. The geopolymer cement concrete is characterized by lower emissions. This is due in part to the CO_2 intensive calcination process used to manufacture Portland Cement. The rotary kilns required for manufacture are heated with fossil fuels and waste hydrocarbons that produce large amounts of greenhouse gas. However, the process of manufacturing NaOH requires electricity for a hydrolosis reaction that emits Cl and H. Both of these products are captured for sale on the commodity market. The emissions listed for the production of the NaOH include those released during electricity generation, proportioned by the percentage coming from fossil sources, hydroelectric sources and nuclear sources.

TABLE 7-3: Energy and water inputs for geopolymer and Portland cements.

Inputs	Geopolymer Cement	Portland Cement
Energy Inputs to Materials Manufacture, BTU (GJ)	955,400 (1.008)	2,085,000 (2.2)
Energy Inputs to Curing, BTU (GJ)	221,800 (0.234)	0
Total Energy Inputs, BTU (GJ)	1,178,000 (1.243)	2,085,000 (2.2)
Water Inputs, lb (kg)	282 (128)	951 (431.5)

TABLE 7-4: Emissions for geopolymer and Portland cements.

Emissions	Geopolymer Cement	Portland Cement
CO, lb (kg)	0.037 (0.017)	1.19 (0.538)
CO_2, lb (kg)	59.7 (27.1)	1,008 (457)
NO_x, lb (kg)	0.384 (0.174)	2.49 (1.13)
Particulates, lb (kg)	0.165 (0.075)	3.09 (1.4)

7.2 Environmental impact

The environmental impact of GCC is related to the energy use and emissions as listed in TABLE 7-3. A brief description of the emissions is provided below.

- Carbon Monoxide - CO is hazardous to humans in concentrations over 5,000 parts per million. In the atmosphere, however, it is likely transformed into CO_2 by reacting with hydroxyl radicals. As CO_2 it contributes to global warming.
- Carbon Dioxide - perhaps the most ubiquitous emission, CO_2 has a natural place in earth's atmosphere. In the quantities that it is currently produced and emitted by industrial processes, it is a major contributor to both acid rain and global warming. CO_2 acts as a greenhouse gas by trapping long wave radiation (heat) from the surface of the earth. Most CO_2 in the atmosphere has come from the burning of fossil fuels. It is removed from the air by plants, which convert it into biomass.
- Nitrogen Oxides - when combustion gasses are cooled in the atmosphere NO reacts with free oxygen or ozone to form NO_2 and NO_3. These molecules form particulates that dissolve in atmospheric water to form nitric acid (HNO_3). The resulting acid is one component of acid rain.

- Particulates come from smoke and dust. They can cause respiratory difficulty and contribute to smog.

The environmental aspects of the GCC lifecycle are not known as accurately as those for PCC. This is because there are very few examples of the material being exposed in the environment for long periods. Laboratory leaching tests have indicated that arsenic leaching might be an issue for fly-ash based geopolymers (Olanrewaju et al., 2009). This would particularly be a problem at the end of a GCC structural element's service life. If GCC components were crushed and landfilled in the same fashion typical for PCC components, the loose arsenic would present a hazard to soils and groundwater. Also, maintenance of GCC components would be hazardous if personnel attempted to refinish the surface by grinding.

7.3 Reducing the life cycle impact of geopolymer concrete

The main lifecycle impacts to the production, use and disposal/recycling of geopolymer cement concrete are related to emissions generation, energy consumption and leaching. The following are strategies that could be instituted to improve the environmental performance of geopolymer cement concrete.

1) Locate Waste Sources of Alkalinity – if alkalinity sources could be located in the waste stream, geopolymer cement production could become a recycling strategy for their disposal. Currently wastes that are too alkaline to enter the municipal wastewater system are neutralized with acid to reduce their pH. Mixing them in with geopolymer would be a safe means of recycling them as well as reducing the

demand for virgin materials in the GCC. Manufacturing the alkalinity source accounts for 80% of the energy input to developing the cementitious properties of the fly ashes. A waste source of alkalinity could greatly reduce the energy inputs.

2) Use Waste or Solar Heat for Curing – the LCA provided in this report shows that 20% of the energy inputs to developing GCC strength are due to elevating temperature curing. However, the temperature range required (<212° F (100 °C) is attainable by collecting solar heat or locating the production facility near a source of waste heat. Since most sources of fly ash are also sources of waste heat, an optimal way to capitalize on industrial synergies is to situate the precasting plant near such a source. This will also eliminate the additional energy (not considered in this dissertation) required to transport fly ash or other aluminosilicates from their production point to the precasting facility.

CHAPTER 8: CONCLUSIONS AND RECOMMENDATIONS FOR FURTHER STUDIES

Geopolymer cement concretes offer an alternative to Portland cement concrete that can provide many of the same structural functions but in a more sustainable fashion by reducing the energy inputs and emissions outputs of the manufacturing process. A series of studies were performed to assess the mechanical performance of geopolymer material test specimens and structural components. These tests have verified the applicability of some design methods for flexural Portland cement concrete components to GCC.

Small specimen studies of GCC materials have correlated splitting tensile strength and compressive elastic modulus with concrete compressive strength. These studies have indicated that the splitting tensile strength of GCC is approximately 15% higher than for similar strength PCC. However, the elastic modulus is slightly lower than for PCC. This implies that while cracking moments for reinforced and prestressed concrete beams would be higher for GCC materials, expected deflections would likely also be higher.

Five flexural beam-columns were prepared in order to study the compressive stress-strain behavior of GCC material under the influence of a strain gradient similar to the gradient that would be developed in a beam undergoing flexure. These tests indicated that GCC concretes are characterized by a long, linear stress-strain relationship followed by a period of diminishing slope. This behavior is similar to the stress-strain response of PCC prior to the onset of strain softening. The experiments reported in this dissertation did not capture a descending branch of the stress-strain relationship. However, they were

also not sufficiently conclusive to rule out the existence of post-peak stress response. As applied to beam analysis, the results were used to prepare modified values of α_1 and β_1 to be used with traditional ACI 318 analysis and design methodologies. The magnitude of these two factors reflected the reduced slope of the stress-strain relationship as compared to similar strength PCC.

A series of reinforced and prestressed concrete beams were fabricated with GCC materials along with similar control beams made from PCC. The beams were tested to failure under controlled loading. The performance of these GCC beams versus PCC beams was qualitatively very similar with steel yielding prior to rupture of concrete in the compressive zone of the beam. The design factors, α_1 and β_1, were applied to analyses of the GCC beams and found to provide accurate predictions for the beam behavior determined experimentally.

Finally, a life cycle assessment was completed to verify the sustainable aspects of the concrete. Using inputs to the concretes prepared for this study, the energy requirements and emissions generation related to manufacturing the GCC were quantified. The results were compared to a similar life cycle assessment for Portland cement concrete. It was determined that manufacturing GCC produces fewer emissions and requires less energy than manufacturing a similar quantity of similar strength PCC for precasting use.

These results indicate that GCC is a feasible material for structural concrete applications. This study has focused on concretes made from only a few batches of source materials and has evaluated the performance of concretes under limited conditions. In order to improve the quality of some of the results, as well as to increase confidence in some of the conclusions, the following are suggested for further study:

- The gradation of aggregates should be optimized more rigorously for the concretes under evaluation. It may be possible to improve the workability and some mechanical characteristics of the concrete by studying the interaction of mortar and aggregate in both the plastic material as well as cured material.
- The tests presented here did not give a conclusive correlation between compressive strength and ultimate strain due to the limited post-peak data recorded in the flexural beam-column tests. The columns tended to fail away from the instrumented zone and may have suffered unintended slenderness effects. For future study, a smaller cross-section should be coupled with shorter overall specimen length to reduce the slenderness effects as well as the required compressive loads. The termination of reinforcement should also be designed to eliminate abrupt stiffness discontinuities and stress concentrations.
- The lifecycle assessment for geopolymer use should extend beyond the manufacture phase. Further work is required on the risks associated with GCC materials exposure to the environment, where they can leach potentially hazardous heavy metals. It is possible that the mix proportions can be further optimized to eliminate this phenomenon.
- Although there was not sufficient data recorded in this study to provide a correlation, it appears that the age of the concrete may have a significant impact on the stress-strain relationship or the ultimate strain. Higher ultimate strains may be found in GCC materials at later ages. This was evidenced by

the very large deflections recorded in the test of the 229 day-old beam GCC-2-B2 prior to reaching its ultimate moment. Mineralogical changes over time might cause such a change in the macro-performance of the material and should be investigated.

REFERENCES

ACI. (2003). "ACI manual of concrete practice - 2003." American Concrete Institute, Detroit, Mich.

ACI Committee 318., and American Concrete Institute. (2002). *Building code requirements for structural concrete : (ACI 318-02) and commentary (ACI 318R-02)*, American Concrete Institute, Farmington Hills, Mich.

ACI Committee 318., and American Concrete Institute. (2008). *Building code requirements for structural concrete : (ACI 318-08) and commentary (ACI 318R-08)*, American Concrete Institute, Farmington Hills, Mich.

Alonso, S., and Palomo, A. (2001). "Alkaline activation of metakaolin and calcium hydroxide mixtures: influence of temperature, activator concentration and solids ratio." *Materials Letters*, 47(1-2), 55-62.

American Coal Ash Association. (2007). "2006 Coal Combustion Products Production and Use Survey." American Coal Ash Association, Aurora.

American Concrete Institute. (2008). *Building code requirements for structural concrete : (ACI 318-08) and commentary (ACI 318R-08)*, American Concrete Institute, Farmington Hills, Mich.

American Concrete Pavement Association. (2009). "Recycling Concrete Pavements."

Andini, S., Cioffi, R., Colangelo, F., Grieco, T., Montagnaro, F., and Santoro, L. (2008). "Coal fly ash as raw material for the manufacture of geopolymer-based products." *Waste Management*, 28(2), 416-423.

ASTM. (1991). "C234-91 Standard Test Method for Comparing Concretes on the Basis of the Bond Developed with Reinforcing Steel ", ASTM International, West Conshohocken, PA.

ASTM. (1994). "C1260 Standard Test Method for Potential Alkali Reactivity of Aggregates (Mortar-Bar Method)." ASTM International, West Conshohocken, PA.

ASTM. (1999). "A944-99 Standard Test Method for Comparing Bond Strength of Steel Reinforcing Bars to Concrete Using Beam-End Specimens." ASTM International, West Conshohocken, PA.

ASTM. (2002a). "C469-02e1 Standard Test Method for Static Modulus of Elasticity and Poissons Ratio of Concrete in Compression ", ASTM International, West Conshohocken, PA.

ASTM. (2002b). "C512-02 Standard Test Method for Creep of Concrete in Compression." ASTM International, West Conshohocken, PA.

ASTM. (2004a). "C42-04 Standard Test Method for Obtaining and Testing Drilled Cores and Sawed Beams of Concrete ", ASTM International, West Conshohocken, PA.

ASTM. (2004b). "C496/C496M-04e1 Standard Test Method for Splitting Tensile Strength of Cylindrical Concrete Specimens ", ASTM International, West Conshohocken, PA.

ASTM. (2005). "C39/C39M-05e1 Standard Test Method for Compressive Strength of Cylindrical Concrete Specimens ", ASTM International, West Conshohocken, PA.

ASTM. (2007). "C192 Standard Practice for Making and Curing Concrete Test Specimens in the Laboratory." ASTM International, West Conshohocken, PA.

ASTM. (2008a). "C805-08 Standard Test Method for Rebound Number of Hardened Concrete." ASTM International, West Conshohocken, PA.

ASTM. (2008b). "C 157 Standard Test Method for Length Change of Hardened Hydraulic-Cement Mortar and Concrete." ASTM International, West Conshohocken, PA.

Bakharev, T. (2005a). "Durability of geopolymer materials in sodium and magnesium sulfate solutions." *Cement and Concrete Research*, 35(6), 1233-1246.

Bakharev, T. (2005b). "Resistance of geopolymer materials to acid attack." *Cement and Concrete Research*, 35(4), 658-670.

Branson, D. E. (1976). *Deformation of concrete structures*, McGraw-Hill, New York.

Buchwald, A., and Schulz, M. (2005). "Alkali-activated binders by use of industrial by-products." *Cement and Concrete Research*, 35(5), 968-973.

Center for Environmental Assessment of Product and Material Systems. (2008). "Sustainable Product Information Network for the Environment." Chalmers.

Chindaprasirt, P., Chareerat, T., and Sirivivatnanon, V. (2007). "Workability and strength of coarse high calcium fly ash geopolymer." *Cement and Concrete Composites*, 29(3), 224-229.

Criado, M., Fernandez-Jimenez, A., de la Torre, A. G., Aranda, M. A. G., and Palomo, A. (2007). "An XRD study of the effect of the SiO2/Na2O ratio on the alkali activation of fly ash." *Cement and Concrete Research*, 37(5), 671-679.

Davidovits, J. (1991). "Geopolymers." *Journal of Thermal Analysis and Calorimetry*, 37(8), 1633-1656.

Diaz, E. I., Allouche, E. N., and Eklund, S. (2009). "Factors affecting the suitability of fly ash as source material for geopolymers." *Fuel*, 89(5), 992-996.

Duxson, P., Fernández-Jiménez, A., Provis, J., Lukey, G., Palomo, A., and van Deventer, J. (2007a). "Geopolymer technology: the current state of the art." *Journal of Materials Science*, 42(9), 2917-2933.

Duxson, P., and Provis, J. (2008). "Designing Precursors for Geopolymer Cements." *Journal of the American Ceramic Society*, 91(12), 3864-3869.

Duxson, P., Provis, J. L., Lukey, G. C., and van Deventer, J. S. J. (2007b). "The role of inorganic polymer technology in the development of `green concrete'." *Cement and Concrete Research*, 37(12), 1590-1597.

Elias-Ozkan, S. T. (2001). "Recycling rubble into aggregates: a model for local governments." *Habitat International*, 25(4), 493-502.

Federal Highway Administration. (2008). "User Guidelines for Byproducts and Secondary Use Materials in Pavement Construction."

Fernandez-Jimenez, A., and Palomo, A. (2003). "Characterisation of fly ashes. Potential reactivity as alkaline cements*." *Fuel*, 82(18), 2259-2265.

Garcia-Lodeiro, I., Palomo, A., and Fernandez-Jimenez, A. (2007). "Alkali-aggregate reaction in activated fly ash systems." *Cement and Concrete Research*, 37(2), 175-183.

Gartner, E. (2004). "Industrially interesting approaches to "low-CO2" cements." *Cement and Concrete Research*, 34(9), 1489-1498.

Geopolymer Institute. (2009). "Technical Data Sheet." Institut Géopolymère, Saint-Quentin, France, quick facts on geopolymer mortars.

Glukhovsky, V. D. (1959). *Soil silicates*, Gosstroyizdat, Kiev.

Guo, X., Shi, H., Chen, L., and Dick, W. A. (2009). "Alkali-activated complex binders from class C fly ash and Ca-containing admixtures." *Journal of Hazardous Materials*, In Press, Corrected Proof.

Hardjito, D., and Rangan, B. (2005). "Development and properties of low-calcium fly ash-based geopolymer concrete." Curtin University of Technology, Perth, Australia.

Henry, J., Towler, M. R., Stanton, K. T., Querol, X., and Moreno, N. (2004). "Characterisation of the glass fraction of a selection of European coal fly ashes." 540-546.

Hognestad, E., Hanson, N. W., and McHenry, D. (1955). "Concrete Stress Distribution in Ultimate Strength Design." *Journal of the American Concrete Institute.*, 52(12), 455-480.

Jo, B. w., Park, S. k., and Park, J. b. (2007). "Properties of concrete made with alkali-activated fly ash lightweight aggregate (AFLA)." *Cement and Concrete Composites*, 29(2), 128-135.

Kou, S. C., Lee, G., Poon, C. S., and Lai, W. L. (2009). "Properties of lightweight aggregate concrete prepared with PVC granules derived from scraped PVC pipes." *Waste Management*, In Press, Corrected Proof.

Lampris, C., Lupo, R., and Cheeseman, C. R. (2009). "Geopolymerisation of silt generated from construction and demolition waste washing plants." *Waste Management*, In Press, Corrected Proof.

Lee, W. K. W., and van Deventer, J. S. J. (2002). "The effect of ionic contaminants on the early-age properties of alkali-activated fly ash-based cements." *Cement and Concrete Research*, 32(4), 577-584.

Lee, W. K. W., and van Deventer, J. S. J. (2004). "The interface between natural siliceous aggregates and geopolymers." *Cement and Concrete Research*, 34(2), 195-206.

MacGregor, J. G., and Wight, J. K. (2005). *Reinforced concrete : mechanics and design*, Prentice Hall, Upper Saddle River, N.J.

Malhotra, V. M., American Concrete Institute., Canada Centre for Mineral and Energy Technology., and Norges tekniske høgskole. (1989). *Fly ash, silica fume, slag, and natural pozzolans in concrete : proceedings, third international conference, Trondheim, Norway, 1989*, American Concrete Institute, Detroit.

Marceau, M., Nisbet, M. A., Van Geem, M. G., and Portland Cement, A. (2006). "Life cycle inventory of portland cement manufacture." Portland Cement Association, Skokie, Ill.

Mecklenburg County Land Use and Environmental Services Agency. (2006). "Mecklenburg County Solid Waste Management Plan, 2006-2016." Mecklenburg County.

Mehta, P. K. (1989). "Pozzolanic and Cementitious by-Products in Concrete--Another Look." Fly ash, silica fume, slag, and natural pozzolans in concrete, American Concrete Institute, Trondheim, Norway, 1-44.

Mertol, H. (2006). "Behavior of high-strength concrete members subjected to combined flexure and axial compression loadings," North Carolina State University, Raleigh, NC.

Michigan Department of Transportation. (2003). "MDOT Standard Specifications for Construction." 692-703.

Mikuni, A., Komatsu, R., and Ikeda, K. (2007). "Dissolution properties of some fly ash fillers applying to geopolymeric materials in alkali solution." *Journal of Materials Science*, 42(9), 2953-2957.

Mindess, S., Young, J. F., and Darwin, D. (2003). *Concrete*, Prentice Hall, Upper Saddle River, NJ.

Nisbet, M. A., and Portland Cement, A. (2007). "Life cycle inventory of Portland cement concrete." Portland Cement Association, Skokie, Ill.

Obla, K., Kim, H., and Lobo, C. (2007). "Crushed Returned Concrete as Aggregates for New Concrete." National Ready Mix Concrete Association.

Olanrewaju, S., Tempest, B., Ogunro, V., Gergely, J., and Daniels, J. (2009). "Effect of Hydroxyl Ion on Immobilization of Oxyanions Forming Trace Elements from Fly Ash-based Geopolymer Concrete." 2009 World of Coal Ash, Lexington, KY.

Palomo, A., Fernandez-Jimenez, A., Lopez-Hombrados, C., and Lleda, J. (2007). "Railway Sleepers made from alkali activated fly ash concrete." *Revista Inenieria de construccion*, 22(2), 5.

Palomo, A., Grutzeck, M. W., and Blanco, M. T. (1999). "Alkali-activated fly ashes: A cement for the future." *Cement and Concrete Research*, 29(8), 1323-1329.

Panagiotopoulou, C., Kontori, E., Perraki, T., and Kakali, G. (2007). "Dissolution of aluminosilicate minerals and by-products in alkaline media." *Journal of Materials Science*, 42(9), 2967-2973.

Panias, D., Giannopoulou, I. P., and Perraki, T. (2007). "Effect of synthesis parameters on the mechanical properties of fly ash-based geopolymers." *Colloids and Surfaces A: Physicochemical and Engineering Aspects*, 301(1-3), 246-254.

Popovics, S. (1973). "A Numerical Approach to the Complete Stress-Strain Curve of Concrete." *Cement and Concrete Research*, 2, 583-599.

Roy, D. M. (1999). "Alkali-activated cements Opportunities and challenges." *Cement and Concrete Research*, 29(2), 249-254.

Sagoe-Crentsil, K., and Weng, L. (2007). "Dissolution processes, hydrolysis and condensation reactions during geopolymer synthesis: Part II. High Si/Al ratio systems." *Journal of Materials Science*, 42(9), 3007-3014.

Sarker, P. (2009). "Analysis of geopolymer concrete columns." *Materials and Structures*, 42(6), 715-724.

Slavik, R., Bednarik, V., Vondruska, M., and Nemec, A. (2008). "Preparation of geopolymer from fluidized bed combustion bottom ash." *Journal of Materials Processing Technology*, 200(1-3), 265-270.

Sofi, M., van Deventer, J., Mendis, P., and Lukey, G. (2007a). "Bond performance of reinforcing bars in inorganic polymer concrete (IPC)." *Journal of Materials Science*, 42(9), 3107-3116.

Sofi, M., van Deventer, J. S. J., Mendis, P. A., and Lukey, G. C. (2007b). "Engineering properties of inorganic polymer concretes (IPCs)." *Cement and Concrete Research*, 37(2), 251-257.

Songpiriyakij, S., Kubprasit, T., Jaturapitakkul, C., and Chindaprasirt, P. (2009). "Compressive strength and degree of reaction of biomass- and fly ash-based geopolymer." *Construction and Building Materials*, 24(3), 236-240.

Standards Association of Australia. (2001). *AS3600 Concrete Structures Code*, Standards Association of Australia, Sydney.

Sumajouw, D., Hardjito, D., Wallah, S., and Rangan, B. (2007). "Fly ash-based geopolymer concrete: study of slender reinforced columns." *Journal of Materials Science*, 42(9), 3124-3130.

Sumajouw, D., and Rangan, B. (2006). "Low-Calcium fly ash-based geopolymer concrete: reinforced beams and columns." Curtin University of Technology, Perth, Australia.

Sun, P. (2005). "Fly ash based inorganic polymeric building material." 216 p.

Swanepoel, J. C., and Strydom, C. A. (2002). "Utilisation of fly ash in a geopolymeric material." *Applied Geochemistry*, 17(8), 1143-1148.

Tam, V. W. Y., Gao, X. F., and Tam, C. M. (2005). "Microstructural analysis of recycled aggregate concrete produced from two-stage mixing approach." *Cement and Concrete Research*, 35(6), 1195-1203.

Tam, V. W. Y., Tam, C. M., and Le, K. N. (2007). "Removal of cement mortar remains from recycled aggregate using pre-soaking approaches." *Resources, Conservation and Recycling*, 50(1), 82-101.

Temuujin, J., van Riessen, A., and Williams, R. (2009). "Influence of calcium compounds on the mechanical properties of fly ash geopolymer pastes." *Journal of Hazardous Materials*, In Press, Corrected Proof.

Texas Department of Transportation. (2004). "Texas Department of Transportation Materials Requirements."

Topçu, I. B., and Sengel, S. (2004). "Properties of concretes produced with waste concrete aggregate." *Cement and Concrete Research*, 34(8), 1307-1312.

Tu, T.-Y., Chen, Y.-Y., and Hwang, C.-L. (2006). "Properties of HPC with recycled aggregates." *Cement and Concrete Research*, 36(5), 943-950.

van Deventer, J. S. J., Provis, J. L., Duxson, P., and Lukey, G. C. (2007). "Reaction mechanisms in the geopolymeric conversion of inorganic waste to useful products." *Journal of Hazardous Materials*, 139(3), 506-513.

van Jaarsveld, J. G. S., and van Deventer, J. S. J. (1999). "Effect of the Alkali Metal Activator on the Properties of Fly Ash-Based Geopolymers." *Industrial & Engineering Chemistry Research*, 38(10), 3932-3941.

van Jaarsveld, J. G. S., van Deventer, J. S. J., and Lukey, G. C. (2002). "The effect of composition and temperature on the properties of fly ash- and kaolinite-based geopolymers." *Chemical Engineering Journal*, 89(1-3), 63-73.

van Jaarsveld, J. G. S., van Deventer, J. S. J., and Lukey, G. C. (2003). "The characterisation of source materials in fly ash-based geopolymers." *Materials Letters*, 57(7), 1272-1280.

Wallah, S., Hardjito, D., Sumajouw, D., and Rangan, B. (2004). "Creep behaviour of fly ash-based geopolymer concrete." 7th CANMET/ACI international conference on recent advances in concrete technology, CANMET/ACI Las Vegas, NV.

Weng, L., and Sagoe-Crentsil, K. (2007). "Dissolution processes, hydrolysis and condensation reactions during geopolymer synthesis: Part I—Low Si/Al ratio systems." *Journal of Materials Science*, 42(9), 2997-3006.

Whitney, C. S. (1937). "Design of Reinforced Concrete Members Under Flexure or Combined Flexure and Direct Compression." *Concrete international : design & construction*, 33(3), 483-498.

Xu, H., and Van Deventer, J. S. J. (2002). "Microstructural characterisation of geopolymers synthesised from kaolinite/stilbite mixtures using XRD, MAS-NMR, SEM/EDX, TEM/EDX, and HREM." *Cement and Concrete Research*, 32(11), 1705-1716.

Yip, C. K., Lukey, G. C., and van Deventer, J. S. J. (2005). "The coexistence of geopolymeric gel and calcium silicate hydrate at the early stage of alkaline activation." *Cement and Concrete Research*, 35(9), 1688-1697.

APPENDIX A: STEEL STRESS-STRAIN CURVES

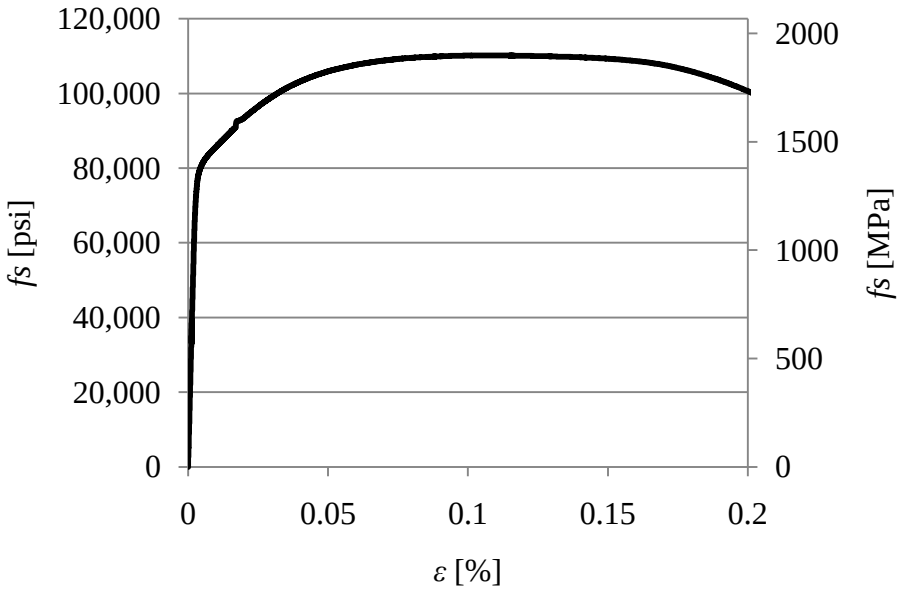

FIGURE A-1: Grade 60 steel f_s vs.ε.

TABLE A-1: Grade 60 steel characteristics, psi (MPa).

f_y	80,000 (552)
E	$28.6X10^6$ ($19.7X10^4$)

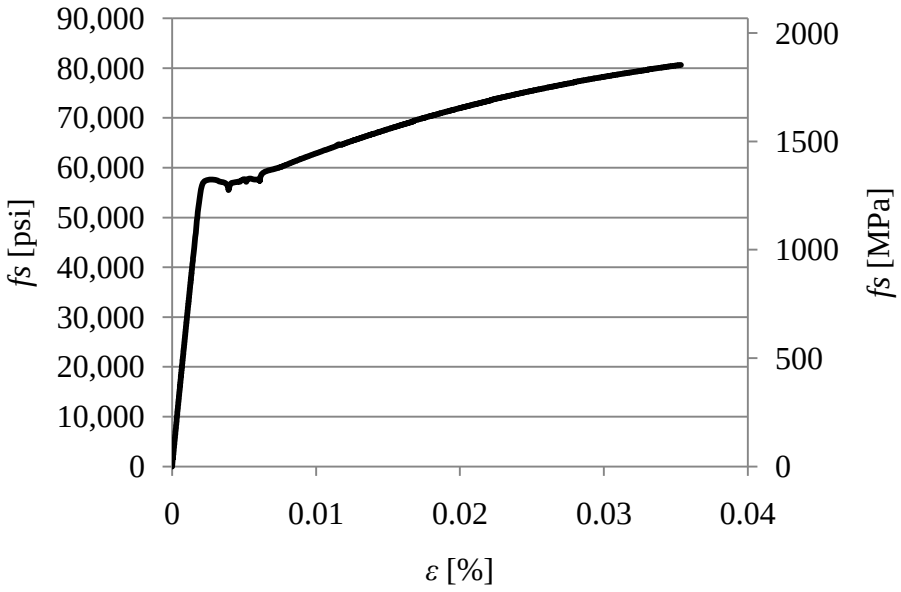

FIGURE A-2: Grade 40 steel f_s vs.ε.

TABLE A-2: Grade 40 steel characteristics, psi (MPa).

f_y	54,000 (379)
E	$28.8X10^6$ ($19.9X10^4$)

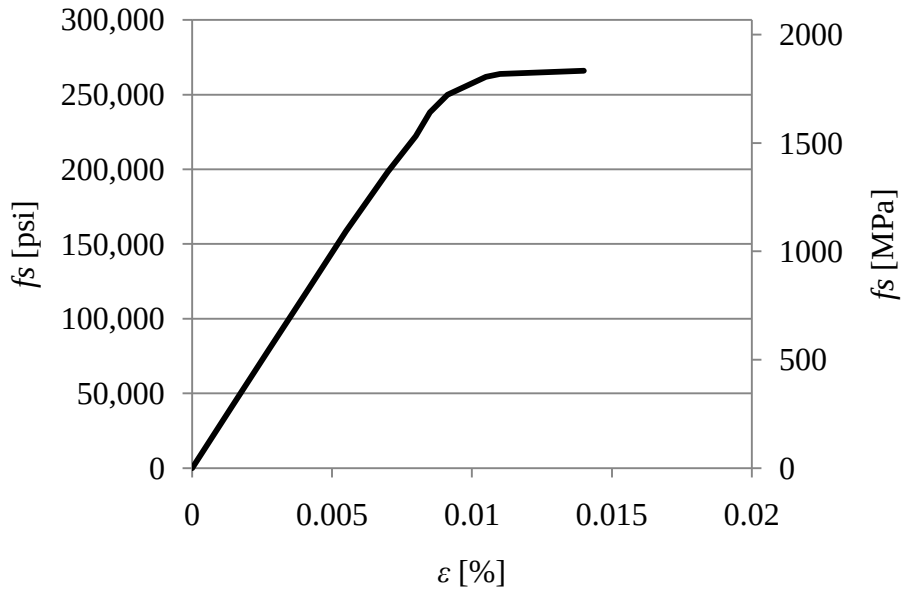

FIGURE A-3: Grade 270 prestressing steel f_s vs.ε.

TABLE A-3: Grade 270 prestressing steel characteristics, psi (MPa).

f_y	257,000 (1,172)
E	$28.3X10^6$ ($19.5X10^4$)

APPENDIX B: MOMENT-CURVATURE MODEL DESCRIPTION

The moment-curvature model used to analyze the moment-deflection behavior of the beams includes two components. The first component is an iterative routine that relates moment to curvature for the beam cross-section broken into 50 horizontal strips in the manner depicted in FIGURE B-1. 48 elements are horizontal strips and two elements represent the compression and tension reinforcing steel. The second component of the model relates curvature to deflection. The following sections of this APPENDIX present the computation technique used for each of these model components.

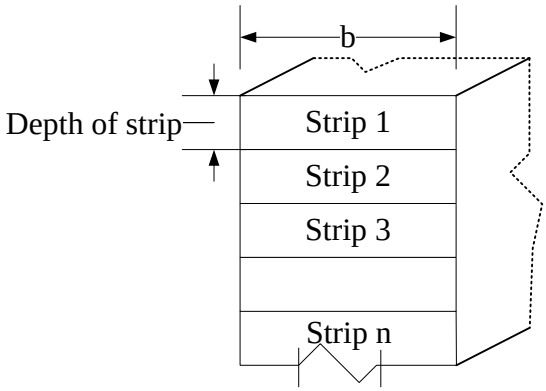

FIGURE B-1: Division of beam into horizontal strips.

a. Preparation of the moment-curvature model

The reinforced concrete beams described in this dissertation featured the cross-sectional details shown in FIGURE B-2. In order to model them the cross section was divided into 48 horizontal strips having a depth of 0.25". Steel in the beam is placed in two layers, which are assigned adjacent to the strip at the same depth in the beam. As is

shown in the first three columns of TABLE B-1, each layer is described by its cross-sectional area and material properties.

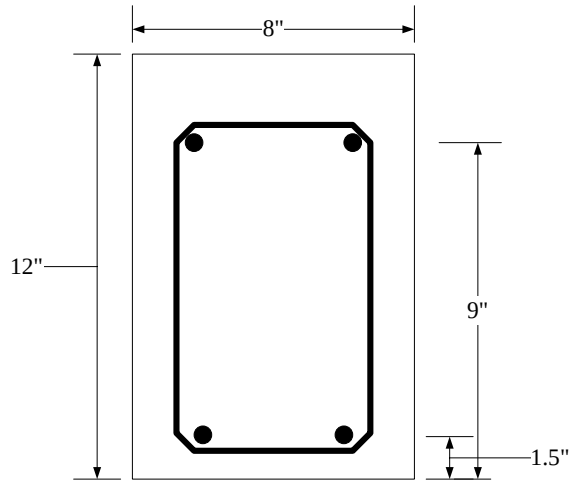

FIGURE B-2: Cross-sectional dimensions and position of steel reinforcing.

An initial value of φ and ε_{top} (as defined in FIGURE B-3) is selected and used to determine the strain at the mid-depth of each segment ε_c by

$$\varepsilon_c = \varepsilon_{top} + \tan(\varphi) \times (col\ b - 0.125) \quad \text{(B-1)}$$

In the example presented in the TABLE B-1, the strain in the extreme compressive fiber ε_c was assumed to be 0.0021. Based on the strain in each strip, the stress in the concrete regions is calculated using the formula,

$$f_c = f_c' \frac{\varepsilon_c}{\varepsilon_{co}} \frac{n}{n-1+\left(\frac{\varepsilon_c}{\varepsilon_{co}}\right)^{nk}} \quad \text{(B-2)}$$

where

$$n = 0.31 f_c' + 0.78 \quad \text{(B-3)}$$

$$k = 0.10 f_c' + 1.20 \quad \text{(B-4)}$$

$$\varepsilon_{co} = 0.0035 \quad \text{(B-5)}$$

Because the compression steel never yielded, the formula

$$f_s = \varepsilon_s \times 29{,}000 \text{ ksi} \qquad \text{(B-6)}$$

is used for steel with compressive strains. For steel in tension the actual stress-strain curve, as measured by direct tension testing, was used to determine stress. The steel stress-strain curves are given in APPENDIX A.

After the concrete cracks in tension it cannot contribute to the development of tension stresses in the cross-section and is no longer considered in the model. Most of the cracked strips are not listed in TABLE B-1 in order to improve readability. The concrete in the beam is assumed to have a limiting compressive strain of 0.0035%. Therefore, a range of maximum compressive strains from 0-0.0035 were modeled to establish the complete range of moment-curvature response.

Once stress is computed, the cross-sectional area of each strip may be used to determine the horizontal force contribution from the strip. The stress associated with each horizontal concrete strip as well as the steel reinforcing is plotted in FIGURE B-3. Also apparent in FIGURE B-3 is the absence of stress in concrete strips beneath the neutral axis since the model has determined that they have cracked.

Using static equilibrium, the angle φ is adjusted so that the sum of the horizontal forces equals 0. Once equilibrium is achieved by balancing φ, the internal moment is computed by taking the moment of the forces from each strip about the compression face of the beam. This process is repeated for each of the ε_c values shown in TABLE B-2 and the results are used to generate the moment-curvature plot given in FIGURE B-4.

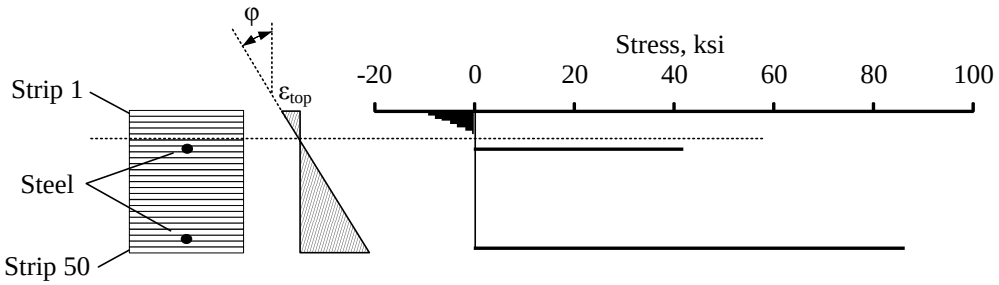

FIGURE B-3: From left a) concrete strips and steel areas; b) strain distribution, c) stress in each strip and in steel bars.

TABLE B-1: Computation of section curvature and associated moment for $\varepsilon_{top} = 0.0021$.

		a	b	c	d	e	f
Strip	Material	Area, in^2	Depth of strip, in	ε_c ($x10^{-5}$ %)	Stress in Strip, ksi	Force from strip, kip	Moment, kip-in
				$\varepsilon_{top} + \tan(\varphi) \times (col\ b - 0.125)$	Results of column c applied in Equations	$col\ a \times col\ d$	$col\ e \times (col\ b - 0.125)$
1	Concrete	2.0	0.25	-19.45	-9.38	-18.75	-2.34
2	Concrete	2.0	0.5	-16.35	-7.89	-15.78	-5.92
3	Concrete	2.0	0.75	-13.25	-6.39	-12.79	-7.99
4	Concrete	2.0	1	-10.15	-4.90	-9.80	-8.57
5	Concrete	2.0	1.25	-7.05	-3.40	-6.81	-7.66
6	Concrete	2.0	1.5	-3.96	-1.91	-3.82	-5.25
7	Concrete	2.0	1.75	-0.86	-0.41	-0.83	-1.34
8	Concrete	2.0	2	2.24	0	0	0
12	Steel	0.4	3	14.64	41.96	16.79	50.36
13	Concrete	2.0	3	14.64	0	0	0
42	Concrete	2.0	10.25	104.51	0	0	0
43	Steel	0.6	10.5	107.61	86.29	51.77	543.63
44	Concrete	2.0	10.5	107.61	0	0	0
50	Concrete	2.0	12	126.21	0	0	0
						$\sum F = 0$	$\sum M = 555$

TABLE B-2: Extreme compression fiber strain, moment and curvature.

ε_c	Moment	φ
0	0	0
-0.0001	104	1.5E-05
-0.0006	280	0.00022
-0.0009	415	0.00035
-0.0012	476	0.00053
-0.0015	506	0.00075
-0.0018	530	0.00099
-0.0021	555	0.00124
-0.0024	578	0.00149
-0.0027	602	0.00173
-0.003	628	0.00203
-0.0033	642	0.00233
-0.0036	653	0.0026
-0.0039	657	0.0028
-0.0042	655	0.00293
-0.0045	650	0.003
-0.005	637	0.00305
-0.006	608	0.00314
-0.009	539	0.00365

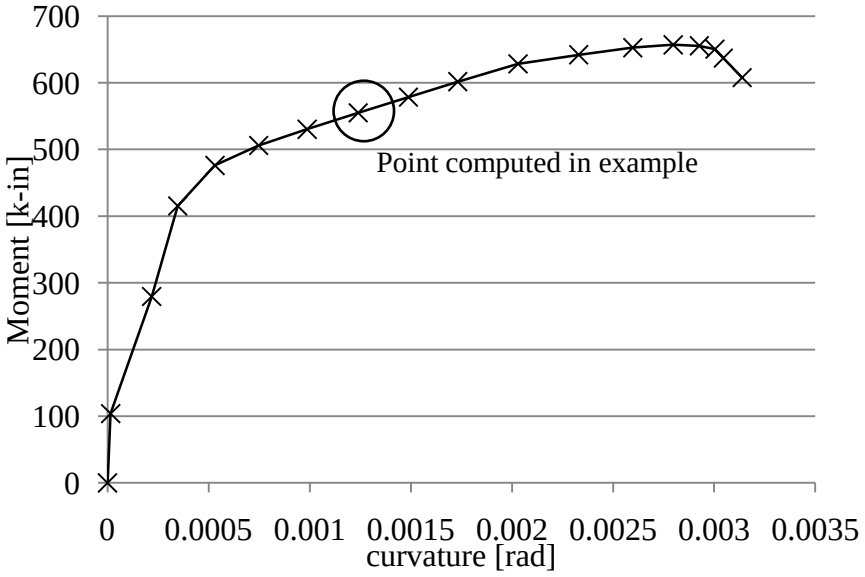

FIGURE B-4: Moment curvature relationship through failure.

b. Computation of beam deflection from moment-curvature relationships.

The beams tested in this study were supported and loaded with the geometry shown in FIGURE B-5a. The beam moment diagram is given in FIGURE B-5b. Using the moment-curvature relationship computed in the previous section, the distribution of curvatures may be assigned to the beam as shown in FIGURE B-5c by relating the magnitude of the moment to the moment curvature relationship. Since this was achieved numerically in the model, the beam was divided into 1" vertical strips oriented perpendicular to the longitudinal axis as shown in FIGURE B-6. The average curvature of each strip is found by relating the moment at that segment with the moment-curvature diagram.

For the simple support conditions used in the experiment, deflection at the midspan is equal to the moment of area about the support of the curvature diagram between the support and midspan. In order to determine the deflection at the midspan, the sum of the moment of area about the west support for each vertical strip in the curvature diagram was computed. For the moment-curvature relationship described in section a), the distribution of curvature for each strip is given in TABLE B-3. The sum of the rightmost column of TABLE B-3 is equal to the deflection of the midspan of the beam. The load *P* corresponding to a midspan moment of 555 kip-in is

$$555 \text{ kip-in}/60 \text{ in} = 9.25 \text{ kip} \qquad \text{(B-7)}$$

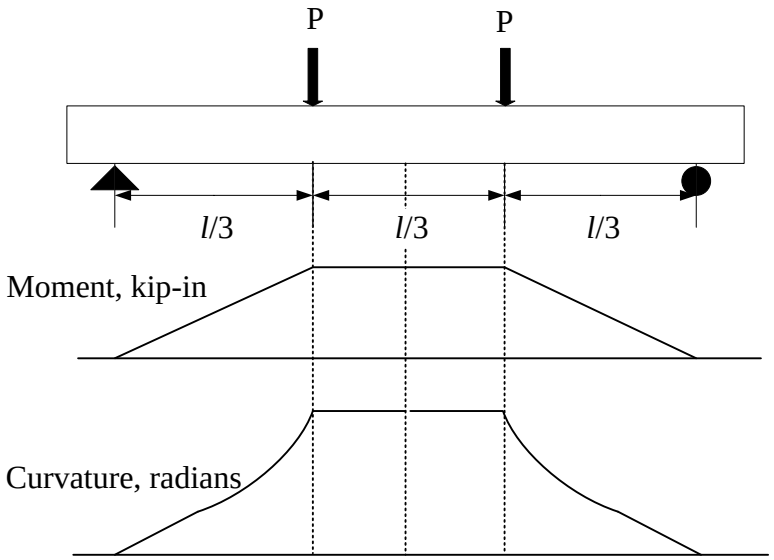

FIGURE B-5: : (from top) a) loading geometry, b) moment diagram, c) distribution of curvature.

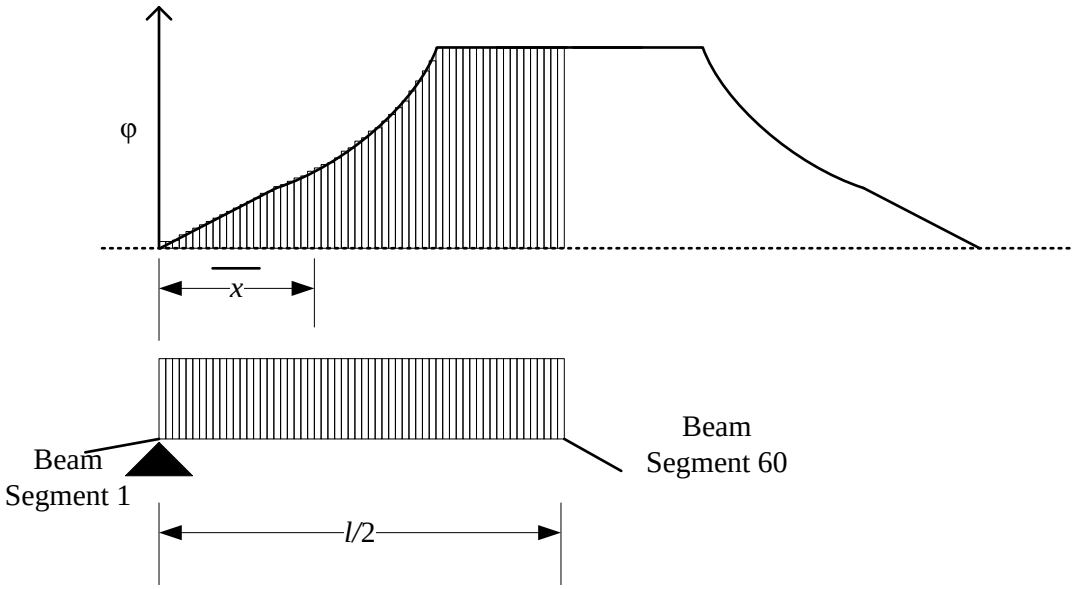

FIGURE B-6: Division of beam and curvature diagram into vertical segments.

TABLE B-3: Curvature for each beam segment.

Beam Segment	$\bar{x}$ (in)	Moment (k-in)	φ (radians $x10^{-5}$)	Moment of area for segment ($x10^{-2}$ in)
1	0.5	7	0.010	0.000
2	1.5	21	0.031	0.000
3	2.5	35	0.052	0.001
4	3.5	49	0.073	0.003
5	4.5	63	0.094	0.004
6	5.5	77	0.114	0.006
7	6.5	91	0.135	0.009
8	7.5	105	0.165	0.012
9	8.5	119	0.326	0.028
10	9.5	133	0.487	0.046
11	10.5	147	0.647	0.068
12	11.5	160	0.808	0.093
13	12.5	174	0.968	0.121
14	13.5	188	1.128	0.152
15	14.5	202	1.288	0.187
16	15.5	216	1.448	0.224
17	16.5	230	1.608	0.265
18	17.5	244	1.768	0.309
19	18.5	258	1.928	0.357
20	19.5	271	2.088	0.407
21	20.5	285	2.236	0.458
22	21.5	299	2.366	0.509
23	22.5	313	2.497	0.562
24	23.5	327	2.628	0.618
25	24.5	340	2.759	0.676
26	25.5	354	2.889	0.737
27	26.5	368	3.020	0.800
28	27.5	382	3.150	0.866
29	28.5	396	3.281	0.935
30	29.5	409	3.411	1.006
31	30.5	423	3.706	1.130
32	31.5	437	4.124	1.299

Beam Segment	$\bar{x}$ (in)	Moment (k-in)	φ (radians x10^{-5})	Moment of area for segment (x10^{-2} in)
33	32.5	451	4.541	1.476
34	33.5	464	4.958	1.661
35	34.5	478	5.461	1.884
36	35.5	492	6.459	2.293
37	36.5	505	7.455	2.721
38	37.5	519	8.792	3.297
39	38.5	533	10.147	3.907
40	39.5	547	11.544	4.560
41	40.5	553	12.249	4.961
42	41.5	554	12.265	5.090
43	42.5	554	12.280	5.219
44	43.5	554	12.293	5.348
45	44.5	554	12.307	5.476
46	45.5	554	12.319	5.605
47	46.5	554	12.330	5.734
48	47.5	554	12.341	5.862
49	48.5	554	12.351	5.990
50	49.5	555	12.360	6.118
51	50.5	555	12.368	6.246
52	51.5	555	12.375	6.373
53	52.5	555	12.382	6.500
54	53.5	555	12.387	6.627
55	54.5	555	12.392	6.754
56	55.5	555	12.396	6.880
57	56.5	555	12.400	7.006
58	57.5	555	12.402	7.131
59	58.5	555	12.404	7.256
60	59.5	555	12.405	7.381
				$\sum = 1.57$